Groundwater Flow and Age Tracer Modeling in the Montérégie Est Bedrock Aquifer using MODFLOW, MODPATH, and MT3D-USGS.

Xuanqi Wang

Supervisor: Dr. Oliver Warr

A thesis submitted to the University of Ottawa in partial fulfilment of the requirements for the Master of Science degree in Earth Science

Department of Earth and Environmental Sciences

Faculty of Science

University of Ottawa

© Xuanqi Wang, Ottawa, Canada, 2026

Declaration of Authorship

I hereby declare that this thesis is entirely my own original work except where otherwise indicated. I am aware of the University's regulations regarding plagiarism. Any use of the works of any other authors is properly referenced at their point of use.

Acknowledgements

I would like to thank Dr. Oliver Warr from University of Ottawa for all of his wonderful supervision, guidance, and support throughout this project. as well as all members of the Warr Group at the University of Ottawa, including Daisy Butera, Harry George Barnes, Jean De La Paix Izerumugaba, Keelan Kells, Liam Zonruiter, Mackenzie Isla Gracequist, Matilda Poole, Natasha Luckovitch, Nick Stepto, Tanuj Mahajan and Zoe Landry, for their assistance and feedback, and support throughout my two years of studies. I also thank Dr. René Lefebvre and the FLOHydro Group at UQAM for their collaboration. I would also like to thank Dr. Florent Barbecot and Dr. Daniele Pinti from UQAM for supporting this project with essential datasets of major ions and age tracers from 2010, also their guidance throughout this project. Special thanks are extended to Ahmed El Azhari for his assistance during the field campaign in 2025. I gratefully acknowledge the Jan Veizer Stable Isotope Laboratory, the Tritium Laboratory, the Radiocarbon Laboratory, and the Geochemistry Laboratory at the University of Ottawa for analyzing the groundwater samples. This research was supported by the Natural Sciences and Engineering Research Council of Canada (NSERC) and the FLOHydro Group, with radiocarbon and tritium analyses supported by the A. E. Lalonde National Accelerator Mass Spectrometry Facility. I would also like to thank Dr. Emmanuel Dubois for serving on my examination committee and for his time, thoughtful comments, and constructive feedback on this thesis. I am also grateful to Dr. Richard Amos for serving on my examination committee and for his careful review, valuable questions, and helpful suggestions that improved this work.

Artificial intelligence (AI) tools were used in a transparent manner to support writing and editing of this thesis. Specifically, Grammarly was used to assist with grammar, spelling, sentence structure, clarity, and overall readability of the written text. All research design, data collection, numerical modelling, analysis, interpretation of results, figures, and conclusions were developed, reviewed, and verified by the author.

Abstract

Groundwater residence times and flow pathways are difficult to constrain in regional fractured bedrock aquifers because groundwater movement is controlled by heterogeneous fracture networks, variable recharge conditions, and mixing between local and regional flow systems. This study developed a numerical coupled groundwater flow, particle-tracking, and age-tracer transport model for the 9,218 km² Montérégie Est fractured bedrock aquifer system in southern Québec, Canada. The model was constructed using MODFLOW-NWT to simulate steady-state regional groundwater flow, and hydraulic head, MODPATH-7 to evaluate advective flow pathways, and MT3D-USGS to simulate the infiltration, transport and decay of tritium (^{3}H) and radiocarbon (^{14}C) from major recharge zones in the region.

The model was developed and calibrated using hydrogeological and geochemical datasets from the 2010 PACES field campaign and was subsequently independently evaluated using groundwater samples collected during a 2025 field campaign. The 2025 sampling targeted wells located near model-derived regional flowpaths and included analyses of ^{3}H, ^{14}C, dissolved inorganic carbon, $\delta^{2}H$, $\delta^{18}O$, and major ions. Surface-water samples were also collected from the region's major watersheds to assess potential river influence.

Simulated hydraulic heads reproduced the regional groundwater gradient well, with strong agreement between measured and modelled heads. The model also captured the main spatial patterns in groundwater age-tracer distributions. ^{3}H simulations reproduced the overall measured–predicted relationship across the 2010 and 2025 datasets, although local deviations indicate unresolved variability in recharge, mixing, and flowpath geometry. ^{14}C simulations showed strong agreement with measured values from 2025, supporting the model's ability to reproduce first-order regional residence-time patterns, while also highlighting the presence of water-rock interactions. Stable isotope results suggest broadly similar meteoric recharge sources between the 2010 and 2025 sampling periods, while temporal changes in ^{3}H and ^{14}C were site-specific, suggesting no overall temporal shift in recharge conditions. Decreases in ^{3}H at several resampled wells are consistent with radioactive decay and reduced modern recharge signals, whereas anomalous increases in ^{14}C at selected wells likely reflect localized surface-water influence or enhanced recent recharge.

The results from the ground-truthed and validated model presented here support the main recharge-to-discharge structure previously proposed for Montérégie Est while highlighting remaining uncertainties associated with local recharge, brackish groundwater zones, and vertical borehole mixing.

Table of contents:

List of Figures**……**viii

List of Tables**……**ix

List of Equations**……...**xi

Conversion Factors**…….....**xiv

Abbreviations**……....**xv

Units**…….....**xv

Chapter 1. Introduction**…….....**1

1.1 Groundwater and Fractured Bedrock Aquifers……..1

1.1.1 Importance of Groundwater Resources…….....1

1.1.2 Groundwater in Fractured Bedrock Aquifers…….2

1.1.3 Importance of Groundwater Residence Times and Recharge Dynamics……4

1.2 Water - Rock interaction and carbonate dissolution……..13

1.2.1 Dissolution and Dead Carbon Addition……13

1.2.2 Cation Exchange and Groundwater Evolution…….14

1.3 Regional Hydrogeological Setting of Montérégie Est Region……16

1.3.1 Geographic and Watershed Overview…….16

1.3.2 Groundwater–Surface-Water Interactions……...20

1.3.3 Beaudry et al. (2018) and the PACES project…….21

1.3.4 Previous Studies of the Montérégie Est Region……..22

1.3.5 Previous Regional Studies Using Age Tracers Combined with ModelMuse…..22

1.4 Regional hydrogeological characterization……24

1.4.1 Hydrogeochemical Classifications Based on Beaudry et al. (2018) 24

1.4.2 Hydrogeological Contexts……...25

1.4.3 Flow regime predictions……..28

1.5 Existing Knowledge Gaps……29

1.6 Study Objectives……...31

Chapter 2. Numerical Modelling Framework**……**32

2.1 Overview of Numerical Modelling Framework……32

2.1.1 General Modelling Framework……....32

2.1.2 Summary of Numerical Modelling Parameters and Components……....33

2.2 Modelling Platform……...38

2.2.1 MODFLOW-NWT Flow Model Setup……....38

2.2.2 Basic Model Configuration……39
2.2.3 Model Layer Configuration……39
2.2.4 Hydraulic Parameters……..44
2.2.4.1 Recharge and Discharge Boundary conditions .....……...49
2.3 MODPATH 7 Particle Tracking Setup……...50
2.4 MT3D-USGS setup……...52
2.4.1 Advection and Dispersion Parameters……52
2.4.2 Péclet Number Analysis and Numerical Stability Assessment……...56
2.5 Data Screening and Selection Criteria……...58
2.5.1 Historic hydrochronologic data used to calibrate model……58
2.5.2 Model Evaluation and Calibration Using Historical Data……..…..63
2.5.3 Delineation of Major Advection Groundwater Flowpaths……..67
2.5.4 ^{3}H Transport Model……68
2.5.5 ^{14}C Transport Model……....71
Chapter 3. Targeted field data to evaluate model……..75
3.1 Field Sampling and Well Sites Selection……....75
3.1.1 New geochemical data used to validate calibrated model……..75
3.1.2 Well Access Permissions and Landowner Consent……79
3.2 Field Sampling Procedures and Analytical methods……....80
3.2.1 Field Sampling Procedures……80
3.2.2 Post-Field Laboratory Analytical Procedures……82
***Chapter 4. Results and model comparisons*……....**84
4.1 Stable Isotopes……..84
4.2. Aqueous geochemistry……89
4.2.1 Major Ion Trends……89
4.2.2 Piper Diagram Interpretation (Stosch, 2022) 91
4.2.3 DIC and Alkalinity Patterns and other field parameters……....93
4.3 Tritium……..97
4.3.1 Tritium Model Accuracy Assessment……....97
4.3.2 Temporal Comparison Between 2010 and 2025 Groundwater Samples……...102
4.4. Radiocarbon……...103
4.4.1 Radiocarbon Model Accuracy Assessment……...103
4.4.2 Temporal Comparison Between 2010 and 2025 Groundwater Samples……...105

Chapter 5. Discussion……106
5.1 Model Results Discussion……106
5.1.1 ModelMuse Results……106
5.1.2 MODPATH-7 Results Discussion……108
5.1.3 MT3D-USGS result discussion……109
5.2 Identifying and characterising water-rock interactions……110
5.2.1 Dead Carbon Addition Along Groundwater Flowpaths……110
5.3 Evaluating potential temporal trends in the data……117
5.4 River Influence……121
5.5 Overall underestimation of the CS group……123
5.6 Model Limitations and Simplifications……124
5.6.1 Fractured Bedrock Layer Geometry……124
5.6.2 Hydraulic Conductivity Assumptions……125
5.6.3 Recharge Simplifications……126
5.6.4 Drain Package and Groundwater-Discharge Representation……127
5.6.5 Hydraulic-Head Constraint and Model Non-Uniqueness……128
5.7 Transport Model Simplifications and Limitations……129
5.7.1 Uniform Dispersivity……129
5.7.2 Vertical Mixing and Groundwater Sampling Depth Limitations……129
5.7.3 Lack of Dual-Domain Mass Transfer……130
5.7.4 Simplified Representation of Tracer Recharge Zones……131
5.7.5 Simplified Radiocarbon Geochemistry……132
5.7.6 Constant Tracer Inputs and Steady-State Conditions……132
Chapter 6. Conclusions……134
6.1 Summary of Major Findings……134
6.2 Limitations and Future Work……136
6.3 Implications for Groundwater Resource Management……139
6.4 Potential Contributions of Regional Age Tracer Groundwater Model……140
References……142
Supplementary Material……152

List of Figures:

Figure 1. Global Meteoric Water Line (GMWL) Showing the Relationship Between δ^2H and $\delta^{18}O$ in Precipitation.
Figure 2. Basses-Laurentides Groundwater Line (BLGWL) Relative to the Basses-Laurentides and Ottawa Meteoric Water Lines.
Figure 3. The Five Hydrogeological Contexts of the Montérégie Est Study Area.
Figure 4. Spatial Distribution of Hydrochemical Water Groups and Brackish Groundwater Distribution in the Montérégie Est Region.
Figure 5. Conceptual figure of the two layered model.
Figure 6. Bedrock-surface topography of the Montérégie Est study area.
Figure 7. Regional piezometric surface of the fractured-bedrock aquifer in the Montérégie Est study area.
Figure 8. Preferential recharge zones to the regional fractured-bedrock aquifer in Montérégie Est.
Figure 9. Spatial distribution of the 2010 PACES age-tracer sampling locations in the Montérégie Est study area (adapted from Beaudry et al., 2018).
Figure 10. Spatial distribution of 2010 PACES groundwater age-tracer sampling locations in the Montérégie Est study area.
Figure 11. Simulated hydraulic head distribution in the Montérégie Est regional groundwater flow model.
Figure 12. Comparison of measured and simulated hydraulic heads for the 2010 PACES model-evaluation wells.
Figure 13. Simulated regional groundwater flow regimes and flow system dynamics.
Figure 14. Measured versus Predicted 2010 Tritium Concentrations by Hydrochemical Water Groups.
Figure 15. Comparison of raw measured and model-predicted ^{14}C values for the 2010 calibration dataset.
Figure 16. Model-guided selection of groundwater sampling locations for the 2025 field campaign.
Figure 17. δ^2H versus $\delta^{18}O$ values of groundwater samples (blue circles) and river water samples (orange squares) collected during the 2025 field campaign in the Montérégie Est study area, Québec.
Figure 18. Temporal comparison of groundwater δ^2H values at the resampled wells between the 2010 and 2025 field campaign.
Figure 19. Hydrochemical facies of groundwater and surface water samples from the 2025 Montérégie Est field campaign using a Piper diagram.
Figure 20. Comparison of measured and model-predicted ^3H concentrations for the 2025 model-evaluation dataset. Measured ^3H concentrations are plotted against MT3D-USGS-predicted concentrations for nine groundwater wells sampled during the 2025 field campaign.
Figure 21. Combined comparison of measured and model-predicted ^3H concentrations for the 2010 and 2025 groundwater datasets.
Figure 22. Comparison of measured and model-predicted raw ^{14}C activities for the 2025 groundwater dataset.
Figure 23. Combined comparison of measured and model-predicted raw 14C activities for the 2010 and 2025 groundwater datasets.
Figure 24. Sensitivity of Simulated ^{14}C Model Performance to Distance from Major Recharge Zones.

List of Tables:

Table 1. Summary of the major groundwater flow and solute transport model parameters and components used in the MODFLOW-NWT, MODPATH 7, and MT3D-USGS numerical modelling framework.
Table 2. 2010 Groundwater wells used to evaluate simulated model predictions against measured groundwater conditions in the Montérégie Est region.
Table 3. Water budget output reported by MODFLOW-NWT.
Table 4. Summary of groundwater tracer and hydrochemical analyses of the 2010 field campaign (Beaudry et al.,2018) and additional data collected by the 2025 field campaign as part of this study, the coordinate system is in Quebec Lambert.
Table 5. Stable isotope compositions (δ^2H and $\delta^{18}O$) of groundwater and surface water samples collected during the 2025 field campaign in the Montérégie Est study area, Québec, measured at the Ján Veizer Stable Isotope Laboratory, University of Ottawa.
Table 6. Comparison of Stable Isotope Compositions ($\delta^{18}O$ and δ^2H) Between the 2010 INRS Field Campaign and the 2025 Groundwater Sampling Campaign for Revisited Wells.
Table 7. Major ion concentrations and calculated carbonate species in groundwater samples collected during the 2025 field campaign in the Montérégie Est study area, Québec.
Table 8. Paired comparison of major-ion concentrations in groundwater samples collected during the 2010 and 2025 field campaigns in Montérégie Est, Québec.
Table 9. Comparison of hydrochemical parameters for groundwater samples collected in 2010 field campaign across the Montérégie Est study area (Beaudry et al., 2018).
Table 10. Hydrochemical parameters for groundwater samples collected in 2025 field campaign in the Montérégie Est study area.
Table 11. Comparison of carbonate system parameters for groundwater wells sampled for age tracers in 2010 and 2025 in the Montérégie Est study area
Table 12. Temporal comparison of tritium (^3H) concentrations between the 2010 and 2025 groundwater sampling campaigns for resampled groundwater wells within the Montérégie Est fractured bedrock aquifer system.
Table 13. Temporal comparison of groundwater age-tracer results between the 2010 and 2025 field campaigns for resampled borehole wells within the Montérégie Est fractured bedrock aquifer system.
Table 14. Suggested starting input values for the MODFLOW-NWT input file (after Niwonfer et al., 2011, U.S. Geological Survey).
Table 15. Final MODFLOW-NWT solver settings used for the Montérégie Est regional groundwater-flow model.
Table 16. Comparison of measured and simulated 2010 hydraulic heads under two MODFLOW-NWT solver configurations.
Table 17. Predicted head vs the measured head by the final model.
Table 18. Sensitivity of simulated 2010 hydraulic heads to the assumed lower model boundary elevation (−250, −500, and −1000 m above mean sea level).
Table 19. Comparison of measured and model-predicted raw ^{14}C activities under alternative coupled hydraulic scaling factors. Residuals were calculated as predicted minus measured activity.
Table 20. Comparison of simulated hydraulic heads under final-model, reduced-KzK_zKz, and no-scaling-factor sensitivity scenarios.
Table 21. Comparison of measured and model-predicted raw ^{14}C values, recharge-zone distance, and interpreted lithologies for sampled groundwater wells within the Montérégie Est fractured bedrock aquifer system from the 2010 field campaign.
Table 22. Comparison of measured and MT3D-USGS-predicted raw ^{14}C activities for selected

2010 groundwater samples from the CS and M2 hydrochemical water groups.
Table 23. Spatial, hydrochemical, and radiocarbon characteristics of the selected 2010 groundwater samples, together with MT3D-USGS predicted 14C activities under three recharge-boundary scenarios. Scenario 1 assigns 100 pMC to all PACES-defined main recharge zones. Scenario 2 assigns 35 pMC to all PACES-defined main recharge zones. Scenario 3 assigns 100 pMC to unconfined zones, while 14C concentrations in semi-confined and confined zones are allowed to evolve through the transport simulation.
Table 24. 2010 measured and predicted tritium data by hydrochemical water group.
Table 25. 2010 Measured and predicted radiocarbon data by hydrochemical water groups.
Table 26. Measured and model-predicted tritium concentrations for the 2025 model-evaluation dataset. Measured and MT3D-USGS-predicted (^{3}H) concentrations are reported in tritium units (TU), with sample-specific analytical uncertainties reported for the measured values. For plotting and statistical analysis, measured or predicted concentrations below 0.5 TU, including measurements below the detection limit, were assigned a value of 0 TU. The dataset contains nine groundwater wells.
Table 27. Measured and model-predicted raw ^{14}C activities for groundwater samples collected during the 2025 field campaign. Measured and MT3D-USGS-predicted ^{14}C activities are reported in percent modern carbon (pMC). Analytical uncertainties reported as $F^{14}C$ were converted to pMC by multiplying by 100.

List of Equations:

Equation 1:

$$N_t = N_0 e^{-\lambda t}$$

Equation 2:

$$t = 8267 \times ln\left(\frac{N_0}{N_t}\right)$$

Equation 3:

$$t = -8267 ln\left(\frac{14Ct}{14Ci \cdot q}\right)$$

Equation 4:

$$q = \frac{\delta\ ^{13}C_{DIC} - \delta\ ^{13}C_{calcite}}{\delta\ ^{13}C_{recharge} - \delta\ ^{13}C_{calcite}}$$

Equation 5:

$$\delta^2H = 8 \times \delta^{18}O + 10$$

Equation 6:

$$\delta^2H = 6.70 \times \delta^{18}O - 0.02$$

Equation 7:

$$CO_2 + H_2O \leftrightarrow H_2CO_3$$

Equation 8:

$$CaCO_3 + H_2CO_3 \leftrightarrow Ca^{2+} + 2HCO_3^-$$

Equation 9:

$$K_x(z) = K_{x,0} \cdot e^{-\lambda z}$$

Equation 10:

$$e^{-\lambda z} = e^{-0.04 \times 50} = e^{-2} = 0.135335283236613$$

Equation 11:

$$K_z = K_x/20$$

Equation 12:

$$C = \frac{KLW}{M}$$

Equation 13:

$$C = \frac{K}{M}$$

Equation 14:

$$C = \frac{K_z \ of \ the \ hydrogeological \ zone}{100 \ m}$$

Equation 15:

$$\frac{\partial}{\partial xi}(D_{i,j}\frac{\partial C}{\partial xj}) - vi\frac{\partial C}{\partial xi} + q_s C_s$$

Equation 16:

$$\alpha_L = 0.32L^{0.83}$$

Equation 17:

$$Pe = \frac{V_e L}{D_L} = \frac{V_D L}{n_e D_L}$$

Equation 18:

$$D_L = \alpha_L v_e + D_m + D_h,$$

Equation 19:

$$P_e \simeq \frac{v_e L}{\alpha L v_e} = \frac{L}{\alpha L}$$

Equation 20:

$$P_e \simeq \frac{L}{\alpha L} = \frac{5000\,m}{376.09\,m} = 13.29$$

Equation 21:

$K_x = K_y$

Equation 22:

$K_x = K_y = 0.135335283236613 * K_{average}$

Equation 23:

$$P_{ec} = \frac{v \Delta x}{D}$$

Equation 24:

$$P_{ec} \simeq \frac{ve \Delta x}{\alpha L ve} = \frac{\Delta x}{\alpha L}$$

Conversion Factors

1 year = 365.25 days in ModelMuse

1 m = 100 cm

1 cm = 100 mm

Abbreviations

DIC: Dissolved Inorganic Carbon

Deuterium excess: d-excess

Radiocarbon-dead carbon: dead carbon

Local Meteoric Water Line: LMWL

Global Meteoric Water Line: GMWL

The Basses - Laurentides Meteoric Water Line: BLMWL

Equivalent Porous Medium: EPM

Calcium: Ca^{2+}

Magnesium: Mg^{2+}

Sodium: Na^{+}

Potassium: K^{+}

Chloride: Cl^{-}

Sulfate: SO_4^{2-}

Fluoride: F^{-}

Bicarbonate: HCO_3^{-}

Carbonate: CO_3^{2-}

Radiocarbon: ^{14}C

Tritium: ^{3}H

Longitudinal dispersivity: αL

Units

Percent modern carbon (pMC)

Tritium Unit (TU)

Chapter 1. Introduction

1.1 Groundwater and Fractured Bedrock Aquifers

1.1.1 Importance of Groundwater Resources

Groundwater is one of the most important freshwater resources on Earth and plays a critical role in supporting human populations, ecosystems, agriculture, and industrial activities (Gleeson et al., 2016). Although only approximately 2.5% of water on Earth is freshwater, more than 68% of this freshwater is stored in glaciers and ice caps, while about 30% is groundwater within aquifers beneath the land surface, making groundwater one of the largest accessible freshwater resources available for human use (United States Geological Survey, 2019; Gleeson et al., 2016; Freeze & Cherry, 1979).

Globally, groundwater provides nearly 50% of the world's drinking water, 33% of industrial water use, and 40% of irrigation water use, supplying approximately 2 billion people worldwide with potable water (UNESCO World Water Assessment Programme, 2022; Karandish et al., 2025). Therefore, groundwater constitutes an essential freshwater resource for human populations worldwide. Groundwater also provides a relatively reliable source of water during periods of drought and surface-water scarcity because subsurface storage can buffer short-term climatic variabilities in water bodies (Taylor et al., 2013). In many regions, groundwater serves as a primary source of potable water and often requires less treatment than surface-water sources due to natural filtration processes occurring within aquifers (Freeze & Cherry, 1979; Fetter, 2018). In addition to supporting domestic water supply, groundwater plays a critical role in agricultural irrigation, industrial activities, and the maintenance of groundwater-dependent ecosystems, including wetlands, rivers, springs, and riparian habitats (Giordano, 2009; Fleckenstein et al., 2010; Gleeson et al., 2016).

In Canada, groundwater is an important component of national water resources and supplies drinking water to approximately 30% of the population, with an even greater dependence observed in rural communities where municipal surface-water infrastructure may be limited (Rivera, 2014). Groundwater resources are particularly important throughout southern Québec, where fractured bedrock aquifers constitute a major source of drinking water for approximately 20% of households and the area dependence is higher for rural areas of more than 90% of the inhabited territory (Larocque et al., 2018). The sustainable management and protection of these groundwater resources are therefore essential for ensuring long-term water security, maintaining groundwater quality, and supporting continued domestic, agricultural, and industrial water use within the region.

Despite their importance, groundwater resources are increasingly threatened by population growth, agricultural intensification, urbanization, industrial development, land-use change, and climate variability. Groundwater represents approximately 99% of the Earth's liquid freshwater resources, and it is often characterized by residence times ranging from months to thousands of years, making it one of the slowest renewing freshwater resources available for human use (Karandish et al., 2025).

As groundwater withdrawals increasingly exceed natural recharge rates, groundwater overexploitation has emerged as a major global sustainability concern. Continued groundwater depletion has been linked to declining groundwater levels, reduced streamflow, land subsidence, groundwater quality deterioration, salinization, biodiversity loss in groundwater-dependent ecosystems, and the drying of groundwater wells (Karandish et al., 2025). In addition, groundwater overexploitation may contribute to increased energy consumption and greenhouse gas emissions through deeper groundwater pumping requirements (Karandish et al., 2025). Continued groundwater depletion has also been shown to reduce streamflow, degrade groundwater-dependent ecosystems such as wetlands, and contribute to ecosystem decline and biodiversity loss (Rohde et al., 2024; Zipper et al., 2024; Konikow & Kendy, 2005). If unsustainable extraction continues, groundwater depletion may also compromise long-term water security and reduce agricultural productivity (Rohde et al., 2024; Zipper et al., 2024; Konikow & Kendy, 2005).

1.1.2 Groundwater in Fractured Bedrock Aquifers

Fractured bedrock aquifers are groundwater systems that occur within consolidated rock formations that commonly underlie unconsolidated surficial deposits such as soil, glacial till, sand, gravel, and clay (Beaudry et al., 2018). Fractured bedrock aquifers are an important source of groundwater worldwide, especially in regions with absent, thin, or discontinuous unconsolidated aquifers e.g. sub-Saharan Africa, Southern India, Fennoscandia, and Central Canada (Singhal & Gupta, 2010; Ohenhen et al., 2023; Chandra et al., 2019; Kitterød et al., 2022; Gleeson et al., 2009; Beaudry et al., 2018).

Unlike porous media aquifers, groundwater flow within fractured bedrock is governed primarily by fractures, faults, bedding planes, and other structural disconnectivities that provide secondary permeability pathways for groundwater movement, these flow pathways are called preferential flow pathways (Freeze & Cherry, 1979; Singhal & Gupta, 2010). These structural features commonly produce heterogeneous and anisotropic hydraulic conditions that may result

in substantial variations in groundwater flow velocities, hydraulic conductivity, recharge pathways, and residence times (Ofterdinger et al., 2019). However, detailed characterization of fracture geometry, connectivity, and hydraulic properties is rarely available at regional scales. This heterogeneity presents a major challenge for numerical groundwater flow modelling because fracture networks cannot usually be characterized in sufficient detail at regional scales. Therefore, fractured bedrock aquifers are commonly represented using an Equivalent Porous Medium (EPM) approach, where the collective hydraulic effects of numerous fractures are represented using equivalent hydraulic properties such as hydraulic conductivity and effective porosity (Cook, 2003). Within this framework, hydraulic heterogeneity is commonly represented through spatially variable hydraulic conductivity zones, including the assignment of elevated hydraulic conductivity values to highly fractured regions or fault zones, while effective porosity is assigned using regional-scale estimates (Cook, 2003; Nastev et al., 2005). Although this approach does not explicitly represent individual fractures or preferential flow pathways, it has been widely applied in regional groundwater flow studies of fractured bedrock aquifers where fracture-network characterization is insufficient to support discrete fracture modelling (Cook, 2003; Nastev et al., 2005).

As groundwater moves through fractured bedrock systems, water-rock interactions progressively modify groundwater chemistry (discussed in more details in Section 1.2). Processes such as mineral dissolution, ion exchange, redox reactions, and precipitation reactions may alter groundwater composition along flowpaths and contribute to the hydrochemical evolution of groundwater with increasing residence time (Freeze & Cherry, 1979; Singhal & Gupta, 2010). The extent of these interactions is influenced by groundwater residence time, mineralogy, groundwater flow velocity, and the degree of contact between groundwater and the surrounding rock matrix (Gleeson et al., 2016).

Characterizing groundwater flow systems and groundwater residence times within fractured bedrock aquifers remains a significant hydrogeological challenge. Fracture networks are inherently heterogeneous, often poorly characterized, and may exhibit strong preferential flow behaviour that is difficult to represent within numerical groundwater flow models. Therefore, groundwater age distributions within fractured bedrock aquifers are often influenced by groundwater mixing, matrix diffusion, dispersion, and water-rock interactions, complicating the interpretation of environmental tracers and groundwater residence times (Berkowitz, 2002; Cook & Herczeg, 2000).

1.1.3 Importance of Groundwater Residence Times and Recharge Dynamics

Groundwater residence time describes the length of time groundwater has remained in the subsurface since recharge (Cook & Herczeg, 2000). Residence times may range from months to years in shallow local groundwater flow systems to thousands or tens of thousands of years or more in deeper regional flow systems (Cook & Herczeg, 2000; Gleeson et al., 2016; Sherwood Lollar et al., 2024). Groundwater age is an important indicator of groundwater residence time and is commonly correlated with groundwater chemistry, water-rock interactions, contaminant transport, nutrient cycling, and ecosystem functioning, making it a fundamental parameter in hydrogeological investigations (Gleeson et al., 2016).

Groundwater recharge represents the process by which precipitation and surface water infiltrate through the unsaturated zone and replenish groundwater systems (Freeze & Cherry, 1979). Recharge rates and recharge locations have a major control on groundwater residence times since they determine both the volume of water entering an aquifer and the rate at which groundwater is renewed (Taylor et al., 2013). Areas experiencing high recharge rates generally contain younger groundwater and shorter residence times due to more rapid groundwater circulation, whereas low recharge rates often result in longer residence times and greater groundwater age (Taylor et al., 2013; Cook & Herczeg, 2000). Recharge conditions also influence groundwater availability and sustainability, as groundwater withdrawals that exceed long-term recharge rates may result in groundwater depletion, declining water levels, reduced baseflow contributions to streams, and degradation of groundwater-dependent ecosystems (Taylor et al., 2013; Karandish et al., 2025). Furthermore, recharge location influences groundwater flowpath length and residence time distributions, with groundwater typically becoming progressively older as it moves away from recharge zones and along regional flow systems (Cook & Herczeg, 2000; Beaudry et al., 2018).

Direct measurement of groundwater residence time is generally not possible because groundwater residence times cannot be observed directly within the subsurface (Cook & Herczeg, 2000). Moreover, measured raw groundwater age distributions may be affected by groundwater recharge conditions, groundwater mixing, dispersion, matrix diffusion, and preferential flow processes, particularly within fractured bedrock aquifer systems (Berkowitz, 2002; Cook & Herczeg, 2000). As a result, environmental tracers have become one of the most widely used tools for investigating groundwater residence times, recharge processes, and groundwater flow systems (Cook & Herczeg, 2000).

Among the available environmental tracers, radiocarbon (^{14}C) and tritium (^{3}H) are two of the most widely applied tracers for evaluating groundwater residence times (Clark & Fritz, 1997; Cook & Herczeg, 2000). These two tracers provide complementary information across different groundwater age ranges, allowing both modern and older groundwater components to be investigated (Clark & Fritz, 1997; Kazemi et al., 2006). Additional tracers, including stable isotopes of water ($\delta^{18}O$ and $\delta^{2}H$) and major ion hydrochemistry, provide important supporting information regarding recharge sources, groundwater evolution, groundwater mixing, and water-rock interactions (Clark & Fritz, 1997; Beaudry et al., 2018). The combined use of environmental tracers provides a robust framework for investigating groundwater residence times and groundwater flow systems within fractured bedrock aquifers (Cook & Herczeg, 2000).

Radiocarbon (^{14}C):

Radiocarbon (^{14}C) is one of the most widely applied environmental tracers for estimating groundwater residence times over timescales ranging from several hundred to tens of thousands of years (Cartwright et al., 2020). ^{14}C is a naturally occurring radioactive isotope of carbon that is continuously produced in the upper atmosphere through interactions between cosmic rays and atmospheric nitrogen (^{14}N), forming ^{14}C with a half-life of approximately 5,730 ±40 years (Libby, 1960; Cartwright et al., 2020; Clark & Fritz, 1997). Following production, ^{14}C rapidly oxidizes to radiocarbon dioxide ($^{14}CO_2$) and mixes with the atmospheric carbon reservoir (Libby, 1960).

Atmospheric $^{14}CO_2$ then enters the biosphere and soil zone through gas exchange and biological activities, becoming incorporated into soil-respired carbon dioxide (Libby, 1960). During groundwater recharge, infiltrating water dissolves soil CO_2 and transfers radiocarbon into dissolved inorganic carbon (DIC) species, including dissolved CO_2, bicarbonate (HCO_3^-), and carbonate (CO_3^{2-}) (Libby, 1960; Cartwright et al., 2020). This process represents the primary pathway through which radiocarbon enters groundwater systems (Libby, 1960; Cartwright et al., 2020).

Because the radioactive decay of ^{14}C occurs at a known rate, measured ^{14}C activity within groundwater DIC can be used to estimate groundwater residence times (Cartwright et al., 2020). Radiocarbon activities are commonly reported as percent modern carbon (pMC), a standardized unit expressing the measured ^{14}C activity of a sample relative to an internationally accepted modern radiocarbon reference standard (Stuiver & Polach, 1977). The modern

reference is defined as 95% of the ^{14}C activity of the National Bureau of Standards (NBS) oxalic acid standard normalized to a $\delta^{13}C$ value of −19‰ relative to the Pee Dee Belemnite (PDB) standard and referenced to the year 1950 CE, which is conventionally defined as "present" in radiocarbon dating (Olsson, 1970; Stuiver & Polach, 1977). Under this convention, a sample exhibiting the same radiocarbon activity as the modern reference standard has a value of 100 pMC, whereas samples containing lower radiocarbon activities exhibit values less than 100 pMC due to radioactive decay and/or geochemical dilution processes. The decrease in groundwater ^{14}C activity through time can be described using the first-order radioactive decay equation, this equation describes the exponential decrease in ^{14}C activity due to solely ^{14}C decay and forms the basis of groundwater radiocarbon dating calculations (Equation 1, Clark & Fritz, 1997). Radiocarbon activities can be used to calculate conventional radiocarbon age per Equation 1:

$$N_t = N_0 e^{-\lambda t} \quad (1)$$

where N_t is the ^{14}C activity remaining at time (t), N_0 is the initial ^{14}C activity at thetime of groundwater recharge, λ is the radioactive decay constant for ^{14}C (0.00012097 yr^{-1} for ^{14}C), and t is the time since groundwater recharge (years).

Conventional radiocarbon ages are typically reported in years before present (BP), where “present” is defined as 1950 CE (Cartwright et al., 2020). Assuming a known initial ^{14}C activity at recharge, groundwater residence time in years may be estimated using the radioactive decay relationship shown in Equation 1 (Clark & Fritz, 1997; Pearson & Hanshaw, 1970) by rewriting Equation 1 as follows (Equation 2):

$$t = 8267 \times ln\left(\frac{N_0}{N_t}\right) \quad (2)$$

Although ^{14}C is a powerful tracer for investigating groundwater residence times, measured ^{14}C activities may be modified by geochemical processes occurring along groundwater flow pathways such as carbonate dissolution and other processes including methanogenesis, sulfate reduction, cation exchange, and CO_2 degassing caused by open system dissolution (Cartwright et al., 2020). Each of these processes can affect the $^{14}C/^{12}C$ ratio, which should be accounted for and corrected to ensure accurate groundwater age estimates (Cartwright et al., 2020). These processes are important when evaluating semi-arid and arid regions where long flow paths and greater geochemical evolution increase the likelihood of ^{14}C signal alterations (Cartwright et al., 2020). In particular, dissolution of carbonate minerals such as calcite and dolomite may introduce geologically old carbon with little or no measurable ^{14}C activity into the DIC pool along flow pathways (Cartwright et al., 2020; Clark & Fritz, 1997;

Han & Plummer, 2013). This process may dilute groundwater ^{14}C activity, resulting in an apparent reduction in measured ^{14}C concentrations and potentially leading to overestimation of groundwater residence times if geochemical corrections are not applied (Cartwright et al., 2020; Clark & Fritz, 1997). Therefore, interpretation of groundwater age from raw measured ^{14}C data commonly requires consideration of groundwater geochemistry, DIC concentrations, and carbon isotope systematics to account for geochemical modification of the radiocarbon signal (Cartwright et al., 2020; Clark & Fritz, 1997, by adapting Equation 2 as follows (Equation 3):

$$t = -8267ln(\frac{14Ct}{14Ci \cdot q}) \quad (3)$$

where t is the estimated groundwater residence time (years), ^{14}Ct is the measured raw radiocarbon activity of groundwater DIC at the time of sampling (pMC), ^{14}Ci is the initial ^{14}C activity of groundwater DIC at recharge (pMC), and q is the fraction of DIC derived from soil-zone carbon following correction for carbonate dissolution and other geochemical processes. q is calculated per Pearson, (1965) and Clark & Fritz (1997) as follows (Equation 4):

$$q = \frac{\delta^{13}C_{DIC} - \delta^{13}C_{calcite}}{\delta^{13}C_{recharge} - \delta^{13}C_{calcite}} \quad (4)$$

where q is the fraction of DIC derived from soil-zone carbon, $\delta^{13}C_{DIC}$ is the measured carbon isotopic composition of DIC in groundwater (‰ VPDB), $\delta^{13}C_{recharge}$ is the assumed isotopic composition of DIC at recharge derived from soil CO_2 (‰ VPDB), and $\delta^{13}C_{calcite}$ is the isotopic composition of carbonate minerals contributing dissolved carbon through carbonate dissolution (‰ VPDB). The equation assumes that groundwater DIC represents a mixture of carbon derived from soil-respired CO_2 and carbonate minerals and is commonly used to estimate the contribution of radiocarbon-dead carbonate carbon to the DIC pool prior to calculating corrected groundwater radiocarbon residence times (Clark & Fritz, 1997).

Dissolved Inorganic Carbon (DIC) and Carbon Isotope Systematics:

Dissolved inorganic carbon (DIC) represents the dissolved carbon species present in groundwater, including dissolved carbon dioxide ($CO_{2(aq)}$), bicarbonate (HCO_3^-), and carbonate (CO_3^{2-}) (Clark & Fritz, 1997). In most groundwater systems, DIC constitutes the dominant form of dissolved carbon, and the relative abundance of its constituent species is controlled primarily by pH-dependent carbonate equilibrium reactions (Clark & Fritz, 1997; Klaus, 2023). Groundwater is one of the largest active continental carbon reservoirs and plays an important role in global carbon cycling through the storage and transport of DIC (Klaus, 2023). Because

DIC originates from multiple sources, including soil-respired carbon dioxide, atmospheric carbon dioxide, carbonate mineral dissolution, and biogeochemical reactions, its concentration and isotopic composition provide valuable information regarding groundwater recharge, groundwater evolution, water-rock interactions, and subsurface carbon cycling (Clark & Fritz, 1997; Cook & Herczeg, 2000; Klaus, 2023).

DIC is of particular importance in radiocarbon hydrogeology because groundwater ^{14}C is measured within the dissolved inorganic carbon pool rather than within the water molecule itself (Clark & Fritz, 1997; Cook & Herczeg, 2000). Hence, processes affecting DIC concentrations and carbon isotope compositions may directly influence measured groundwater ^{14}C activities and the interpretation of groundwater residence times. Measurements of DIC concentrations are therefore commonly coupled with radiocarbon analyses to evaluate groundwater carbon sources and support interpretation of groundwater age tracer data (Clark & Fritz, 1997).

The isotopic composition of dissolved inorganic carbon ($\delta^{13}C$-DIC) provides additional information regarding carbon sources and biogeochemical processes within groundwater systems (Clark & Fritz, 1997; Cook & Herczeg, 2000). As soil-derived carbon, atmospheric carbon, carbonate minerals, and organic matter each possess characteristic $\delta^{13}C$ signatures, $\delta^{13}C$-DIC measurements can be used to distinguish between different carbon sources contributing to groundwater DIC. Consequently, $\delta^{13}C$-DIC is commonly used alongside DIC concentrations and radiocarbon measurements to evaluate groundwater evolution and support geochemical correction of groundwater ^{14}C ages (Clark & Fritz, 1997; Cook & Herczeg, 2000).

Tritium (^3H)

Tritium (^3H), is a radioactive isotope of hydrogen with a half life of 12.32 years that occurs naturally in the environment by the neutron of cosmic rays interacting with nitrogen (N_2), producing ^{12}C and ^3H (Vogel et al., 1974; Okada & Momoshima, 1993; Lucas & Unterweger, 2000; Clark & Fritz, 1997). Tritium concentrations are commonly reported in Tritium Units (TU), where 1 TU corresponds to one tritium atom per 10^{18} hydrogen atoms, equivalent to approximately 0.118 Bq/L in water (Clark & Fritz, 1997). In addition to this natural production, a vast amount of ^3H was generated and released into the upper atmosphere during the 1950s and 1960s, due to the testing of nuclear weapons which generated a major bomb ‘spike’ which entered the hydrogeologic cycle through precipitation (Vogel et al., 1974; Okada & Momoshima, 1993). For example, precipitation in South Africa showed a rise from

around 20 TU in the year 1958 to 50 TU by 1963 (Okada & Momoshima,1993). This 'spike' makes ^{3}H a useful tracer to distinguish pre-modern (pre-1950s) groundwater from modern groundwater (past 1950s) (Vogel et al., 1974; Okada & Momoshima, 1993; Lindsey et al., 2019). Age estimation of groundwater using ^{3}H is often simplified into a binary classification system by applying a defined threshold to separate modern from pre modern groundwater (Okada & Momoshima, 1993). Due to its relatively short half-life and the introduction of large quantities of ^{3}H into the atmosphere during nuclear weapons testing, tritium is widely used to distinguish groundwater recharged before and after the bomb-pulse period of the 1950s and 1960s. In addition, when atmospheric input functions are known, ^{3}H concentrations can be used to estimate groundwater residence times and evaluate groundwater recharge processes (Vogel et al., 1974; Clark & Fritz, 1997; Lindsey et al., 2019; Okada & Momoshima, 1993). The radioactive decay of tritium follows the same first-order decay relationship described in Equation 1. For ^{3}H, the decay constant (λ) is 0.05626 yr^{-1}, corresponding to a half-life of 12.32 years (Lucas & Unterweger, 2000). Due to this relatively short half-life, ^{3}H is primarily used to identify modern groundwater recharge and estimate groundwater residence times on decadal timescales. However, local recharge processes such as mountain-front recharge and irrigation-driven recharge can introduce younger groundwater into aquifer systems, resulting in elevated ^{3}H concentrations relative to regional expectations (Scanlon et al., 2006; Lindsey et al., 2019). These anomalies highlight the influence of local hydrogeological conditions on groundwater age interpretations and are not unique to tritium-based assessments.

^{3}H is a useful tracer for groundwater residence time, however, its effectiveness in accurately predicting groundwater age diminishes with increasing groundwater age. Specifically, groundwater older than ~60 years have tritium levels close to or below detection limits due to radioactive decay, making it impossible to accurately estimate residence times of groundwater older than 60 years by solely using ^{3}H as an age tracer. Therefore, in systems where older groundwaters are liable to be present coupling ^{3}H analyses with other tracers such as ^{14}C is essential (Clark & Fritz, 1997; Cartwright et al., 2020; Okada & Momoshima, 1993). Additional limitations arise from groundwater mixing and other subsurface transport processes that may alter tritium concentrations and complicate groundwater age interpretations (Clark & Fritz, 1997; Cartwright et al., 2020; Okada & Momoshima, 1993). As bomb-derived tritium continues to decay toward natural background levels, the ability of tritium alone to distinguish pre-bomb and post-bomb groundwater is expected to become indistinguishable in many regions

by approximately 2030, increasing the importance of combining tritium with other environmental tracers for robust groundwater age interpretation (Eastoe et al., 2012).

Stable Isotopes ($\delta^{18}O$ and $\delta^{2}H$):

The stable isotopes of water ($\delta^{18}O$ and $\delta^{2}H$) are used to understand the recharge mechanisms such as temperature and altitude at the point of recharge and identify the potential mixing of different groundwater sources in the subsurface (Leketa & Abiye, 2021). Because oxygen and hydrogen isotopes undergo systematic mass-dependent fractionation during evaporation and condensation processes, $\delta^{18}O$ and $\delta^{2}H$ typically co-vary in natural waters (Craig, 1961). This relationship forms the basis of the Global Meteoric Water Line (GMWL), which was defined as (Craig, 1961) (Equation 5):

$$\delta^{2}H = 8 \times \delta^{18}O + 10 \quad (5)$$

Subsequent monitoring of the stable isotopic composition of precipitation worldwide (IAEA Global Network for Isotopes in Precipitation - GNIP) has refined this relationship (Figure 1).

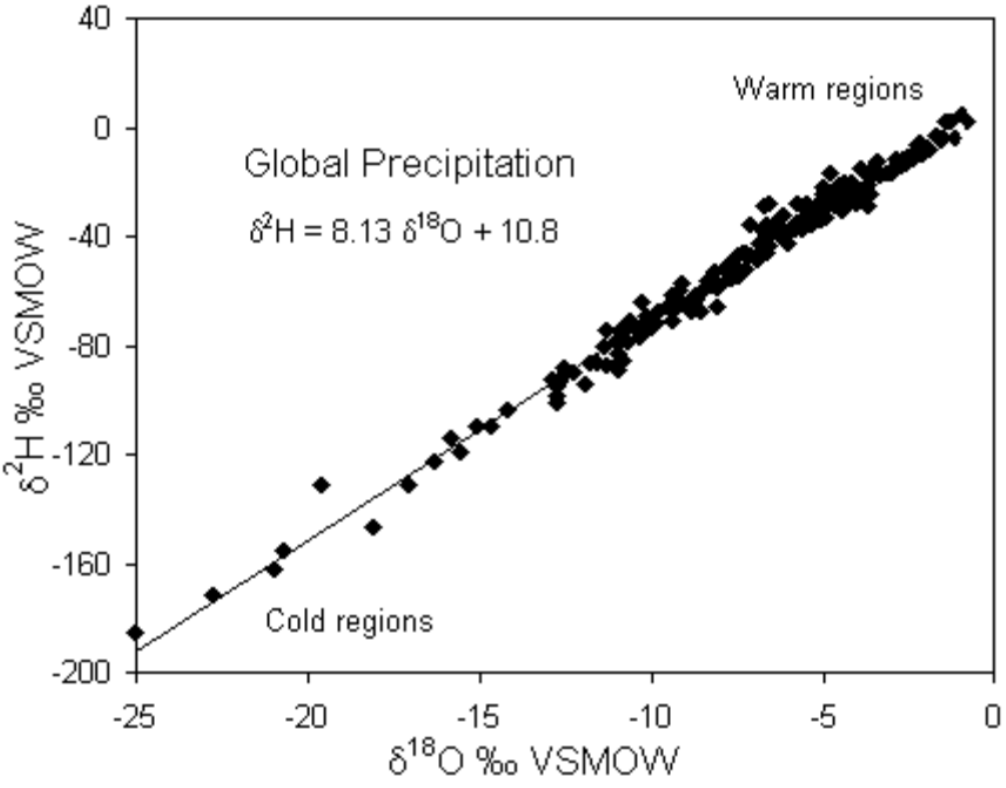


Figure 1. Global Meteoric Water Line (GMWL) Showing the Relationship Between $\delta^{2}H$ and $\delta^{18}O$ in Precipitation. Global Meteoric Water Line (GMWL) showing the linear relationship between $\delta^{2}H$ and $\delta^{18}O$ in global precipitation. Data represent weighted average

annual values from the IAEA Global Network for Isotopes in Precipitation (GNIP), compiled by Rozanski et al. (1992) (Figure 1 is reproduced from Clark & Fritz, 1997, Chapter 2).

Each region has a Local Meteoric Water Line (LMWL) that slightly deviates from the GMWL (Clark & Fritz, 1997). As no LMWL has been established specifically for the Montérégie Est region, the Basses-Laurentides Meteoric Water Line (BLMWL) was selected as the most representative regional comparison. The BLMWL was established by Cloutier et al. (2006) from precipitation samples by Cloutier (2004). Cloutier et al. (2006) also demonstrated via least-squares regression that 146 groundwater samples from the region were distributed around the BLMWL, indicating recharge from local precipitation with no significant isotopic modification by evaporation. Therefore, the BLGWL is used in this study as the most representative regional isotopic reference line for comparison with groundwater samples from Montérégie Est. The BLGWL is defined by Equation 6 and is plotted in Figure 2:

$$\delta^2H = 6.70 \times \delta^{18}O - 0.02 \quad (6)$$

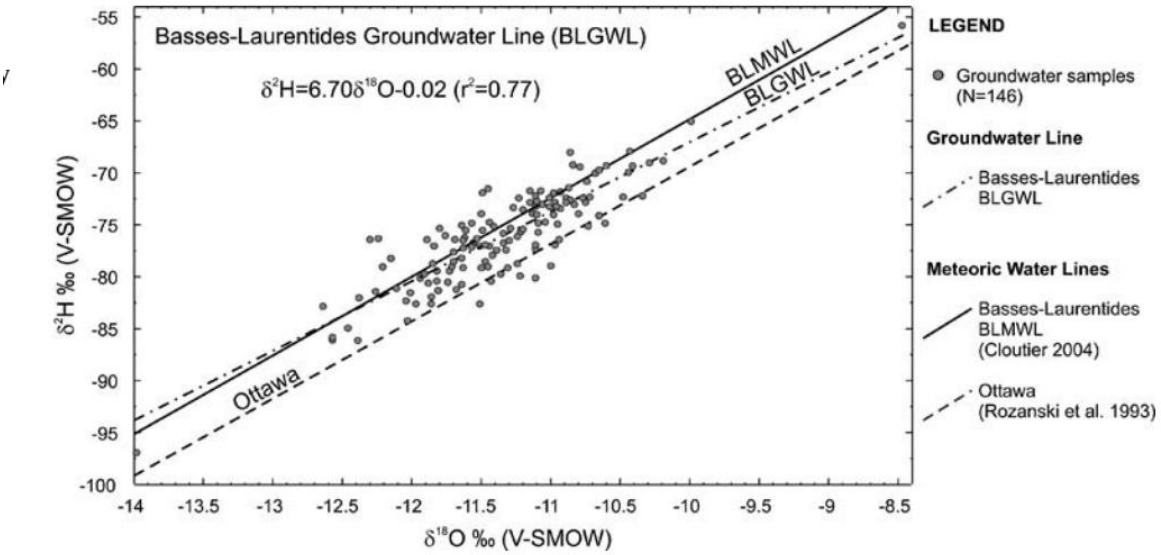


Figure 2. Basses-Laurentides Groundwater Line (BLGWL) Relative to the Basses-Laurentides and Ottawa Meteoric Water Lines. The Basses - Laurentides Groundwater Line (BLGWL; dashed line) reflects the isotopic composition of local groundwater from 146 samples collected during Cloutier et al.'s 2004 study, while the Basses- Laurentides Meteoric Water Line (BLMWL; solid line) represents the isotopic signature of local precipitation. The Ottawa meteoric water line (Rozanski et al., 1993) is also shown for regional comparison. (Figure 2 is reproduced from Cloutier et al., 2006).

Comparison of groundwater stable isotope compositions with the BLMWL provides important information regarding groundwater recharge conditions and post-recharge processes. Groundwater samples plotting close to the BLMWL generally indicate recharge derived directly from meteoric precipitation with limited isotopic modification following infiltration (Clark & Fritz, 1997). In contrast, groundwater samples plotting below the BLMWL commonly indicate evaporative enrichment of the heavier isotopes (^{18}O and ^{2}H), as evaporation preferentially removes lighter isotopes and produces a lower $\delta^{2}H/\delta^{18}O$ slope than expected for meteoric precipitation (Clark & Fritz, 1997; Gat, 1996). Deviations from the BLMWL may also reflect mixing between different water sources, seasonal recharge biases, or secondary isotopic fractionation processes occurring before groundwater reaches the saturated zone (Clark & Fritz, 1997).

The d-excess or deuterium-excess, which is calculated by $\delta^{2}H - 8 \times \delta^{18}O$, represents the extent of deviation from the GMWL and can provide additional information about the temperature and humidity conditions at sea surface at the time of initial ocean evaporation, moisture conditions along the air mass trajectory, and the potential for secondary evaporation (or re-evaporation) of water droplets in the sub-cloud level within a region (Leketa & Abiye, 2021; Dansgaard, 1964; Clark & Fritz, 1997).

Major ions:

Major ion chemistry provides important information regarding groundwater recharge sources, groundwater evolution, water-rock interactions, and geochemical processes occurring within aquifer systems (Appelo & Postma, 2005; Clark & Fritz, 1997). Variations in major ion concentrations commonly reflect mineral weathering, dissolution and precipitation reactions, ion exchange, groundwater mixing, and residence time-related geochemical evolution along groundwater flowpaths (Freeze & Cherry, 1979; Appelo & Postma, 2005). Major ions are typically classified as either cations, which carry a positive charge, or anions, which carry a negative charge (Appelo & Postma, 2005). The major cations measured in this study include calcium (Ca^{2+}), magnesium (Mg^{2+}), sodium (Na^{+}), and potassium (K^{+}), while the major anions include chloride (Cl^{-}), sulfate (SO_4^{2-}), fluoride (F^{-}), bicarbonate (HCO_3^{-}), and carbonate (CO_3^{2-}) (Appelo & Postma, 2005). Unlike the other major ions, bicarbonate and carbonate concentrations were not measured directly but were calculated from measured pH, temperature, alkalinity, and dissolved inorganic carbon (DIC) concentrations using carbonate equilibrium relationships (Clark & Fritz, 1997).

1.2 Water - Rock interaction and carbonate dissolution

1.2.1 Dissolution and Dead Carbon Addition

Carbonate dissolution refers to the reaction between carbonic-acid-bearing groundwater and carbonate minerals such as calcite or dolomite (Clark & Fritz, 1997). During groundwater recharge, soil-derived CO_2 dissolves into infiltrating water and forms carbonic acid, which can react with carbonate minerals present within soils, sediments, and aquifer rocks (Clark & Fritz, 1997; Agrawal et al., 2024). A commonly applied series of calcite dissolution reactions is (Equation 7&8) (Freeze and Cherry, 1979; Clark & Fritz, 1997):

$$CO_2 + H_2O \leftrightarrow H_2CO_3 \quad (7)$$

$$CaCO_3 + H_2CO_3 \leftrightarrow Ca^{2+} + 2HCO_3^- \quad (8)$$

These two reactions increase DIC, primarily as bicarbonate (HCO_3^-), while simultaneously increasing dissolved calcium concentrations within groundwater (Clark & Fritz, 1997). Carbonate dissolution is particularly common in carbonate-bearing lithologies such as limestone, dolostone, marlstone, calcareous sediments, carbonate-rich tills, and aquifer materials containing calcite or dolomite minerals (Clark & Fritz, 1997; Nowak et al., 2017). In limestone aquifer systems, recharge waters containing biogenic soil CO_2 can also react directly with carbonate minerals in the aquifer matrix, producing DIC derived from both soil-respired and rock-derived carbon sources (Nowak et al., 2017).

The evolution of carbon isotopes during carbonate dissolution is particularly important for groundwater radiocarbon dating. Soil-derived carbon dioxide originates from recently fixed atmospheric carbon and therefore contains naturally occurring ^{12}C, ^{13}C, and ^{14}C isotopes (Clark & Fritz, 1997; Agrawal et al., 2024). Alternatively, carbonate minerals are typically millions of years old and contain abundant ^{12}C and ^{13}C but negligible ^{14}C because any original radiocarbon has decayed over geological timescales (Clark & Fritz, 1997; Seltzer et al., 2021). As a result, dissolution of carbonate minerals can significantly alter the isotopic composition of DIC in groundwater (Clark & Fritz, 1997; Han & Plummer, 2016). Because groundwater radiocarbon dating is based on the ratio of ^{14}C to stable carbon isotopes within the DIC pool, dissolution of carbonate minerals introduces large quantities of geologically old carbon containing ^{12}C and ^{13}C but virtually no measurable ^{14}C. Hence, the abundance of stable carbon isotopes increases relative to ^{14}C, lowering the $^{14}C/^{12}C$ ratio independently of radioactive decay (Fontes & Garnier, 1979; Han & Plummer, 2016). This may produce an apparent decrease in

radiocarbon activity that may cause groundwater to appear older than its true residence time if geochemical corrections are not applied (Han & Plummer, 2016; Clark & Fritz, 1997).

The extent of these isotopic changes depends strongly on whether dissolution occurs under open-system or closed-system conditions (Clark & Fritz, 1997; Schlegel et al., 2024). In open-system dissolution, groundwater remains in contact with soil CO_2 during carbonate weathering, allowing continued isotopic exchange with the soil-gas reservoir and generally maintaining relatively high ^{14}C activities (Clark & Fritz, 1997; Seltzer et al., 2021). In closed-system dissolution, groundwater becomes isolated from the soil-gas reservoir prior to carbonate dissolution, causing additional carbonate-derived DIC to dilute groundwater ^{14}C activities and therefore 'age' the groundwaters, while shifting $\delta^{13}C$-DIC values toward those characteristics of carbonate minerals (Clark & Fritz, 1997; Schlegel et al., 2024).

As groundwater moves along regional flowpaths, continued water-rock interaction, groundwater mixing, carbonate dissolution, microbial respiration, and isotopic exchange may further modify DIC concentrations and carbon isotope compositions (Cook & Herczeg, 2000; Nowak et al., 2017; Schlegel et al., 2024). Consequently, observed reductions in groundwater ^{14}C activity commonly reflect a combination of radioactive decay, groundwater mixing, and geochemical evolution rather than groundwater age alone (Clark & Fritz, 1997; Cook & Herczeg, 2000). As $\delta^{13}C$-DIC responds differently to soil-derived and carbonate-derived carbon sources, it is commonly used alongside ^{14}C activities to evaluate dead-carbon contributions and support interpretation of groundwater residence times per Equation 4 (Clark & Fritz, 1997). For this reason, interpretation of groundwater residence times using radiocarbon commonly requires integration of DIC concentrations, $\delta^{13}C$-DIC measurements, and hydrogeochemical observations to distinguish radioactive decay from independent geochemical modification of the carbon system via low temperature soil/water-rock interactions (Clark & Fritz, 1997; Cook & Herczeg, 2000).

1.2.2 Cation Exchange and Groundwater Evolution

Cation exchange is a hydrogeochemical process where dissolved cations in groundwater are exchanged with cations adsorbed onto mineral surfaces, particularly clay minerals (Appelo & Postma, 2005; Clark, 2015). Together with mineral dissolution and weathering reactions, cation exchange is recognized as one of the primary processes controlling the chemical evolution of groundwater flow systems (Hem, 1985; Appelo & Postma, 2005; Carol et al., 2012). Clay minerals possess negatively charged surface and interlayer sites that

attract and retain exchangeable cations including Na^+, Ca^{2+}, Mg^{2+}, and K^+ (Clark, 2015). These negatively charged exchange sites originate from imperfections within clay mineral crystal structures and from surface charge development on clay particles, giving clay-rich sediments a high capacity to adsorb and exchange dissolved cations with groundwater (Appelo & Postma, 2005; Clark, 2015). Changes in groundwater chemistry can modify the equilibrium between groundwater and these exchange sites, causing adsorbed cations to be replaced by dissolved cations present in groundwater (Carol et al., 2012; Clark, 2015). Therefore, groundwater chemistry may evolve substantially through cation exchange reactions even in the absence of significant mineral dissolution or precipitation processes.

Common clay minerals including smectite, illite, and kaolinite contain negatively charged exchange sites capable of adsorbing and releasing dissolved cations from groundwater (Clark, 2015). Clay minerals may occur within weathered bedrock, fracture fillings, glacial tills, shale units, fine-grained sedimentary deposits, and clay-rich overburden materials, providing abundant opportunities for groundwater-clay interactions during subsurface flow (Clark, 2015). As groundwater migrates through these materials, cation exchange reactions may progressively modify groundwater composition and contribute to hydrochemical evolution along groundwater flowpaths.

One of the most commonly observed consequences of cation exchange is the progressive evolution of groundwater from Ca-HCO_3 groundwater in recharge areas toward Na-HCO_3 groundwater in discharge areas (Carol et al., 2012; Capuano & Jones, 2020). This process occurs when calcium-rich recharge water encounters clay minerals containing exchangeable sodium. Under these conditions, dissolved Ca^{2+} ions are adsorbed onto clay surfaces while Na^+ ions are released into groundwater, resulting in increasing sodium concentrations and decreasing calcium concentrations along groundwater flowpaths (Carol et al., 2012; Capuano & Jones, 2020). Carol et al. (2012) identified Ca^{2+}–Na^+ exchange as the primary mechanism responsible for groundwater evolution from Ca-HCO_3 waters in recharge zones to Na-HCO_3 waters in local discharge areas. Similarly, Capuano and Jones (2020) describe the exchange of calcium in recharging meteoric waters for sodium adsorbed on clay minerals as one of the most characteristic cation exchange processes occurring in clastic aquifers.

Cation exchange has been identified as an important process controlling groundwater evolution within the Montérégie Est fractured bedrock aquifer system. Beaudry et al. (2018) identified a large brackish groundwater zone within the northern St. Lawrence Lowlands and

reported that this zone is surrounded by sodic and alkaline groundwater resulting from Na^{+}–Ca^{2+} ionic exchange. Their study concluded that cation exchange, together with groundwater mixing and water-rock interactions, represents one of the principal mechanisms controlling groundwater chemistry across the region (Beaudry et al., 2018). As groundwater residence time increases and groundwater migrates away from recharge zones, cation exchange contributes to the development of chemically evolved groundwater characterized by elevated sodium concentrations, reduced calcium concentrations, and increasingly alkaline conditions (Beaudry et al., 2018).

1.3 Regional Hydrogeological Setting of Montérégie Est Region

The hydrogeological framework presented in this study is primarily based on the regional characterization developed through the Programme d'acquisition de connaissances sur les eaux souterraines (PACES) project and the conceptual groundwater flow model subsequently proposed by Beaudry et al. (2018) (Larocque et al., 2018 & Beaudry et al., 2018). These studies represent the most comprehensive regional investigations of groundwater occurrence, groundwater chemistry, groundwater flow systems, and groundwater residence times currently available for the Montérégie Est fractured bedrock aquifer system. The following sections summarize the regional geographic setting, geological framework, hydrogeological contexts, and groundwater flow concepts relevant to the development of the numerical modelling framework and interpretation of groundwater tracer data.

1.3.1 Geographic and Watershed Overview

The Montérégie Est region is located in southern Québec, Canada, immediately east of Montréal and covers approximately 9,218 km² (Beaudry et al., 2018). The study area is bounded by the St. Lawrence River to the northwest and by the United States border with Vermont and New York to the south (Beaudry et al., 2018). This region contains three major watersheds: the Richelieu River watershed, the Missisquoi Bay watershed, and the Yamaska River watershed. The Richelieu River and Missisquoi Bay watersheds are sub-watersheds of the broader Lake Champlain watershed, whereas the Yamaska River watershed constitutes the third major surface-water drainage system within the study area (Beaudry et al., 2018). The region encompasses 108 municipalities and supports a population of approximately 790,000

inhabitants, with agriculture representing one of the dominant land uses throughout much of the area (Beaudry et al., 2018). Groundwater resources and their appropriate management for sustainable long-term use are therefore of considerable importance for domestic, agricultural, industrial, and municipal water supply within the region.

To help with regional hydrogeological characterization, the Montérégie Est study area was divided into five hydrogeological contexts based on physiography, bedrock geology, surficial sediment distribution, and hydrogeological characteristics: the Northern St. Lawrence Lowlands, Southern St. Lawrence Lowlands, Appalachian Piedmont, Appalachian Uplands, and Monteregian Hills (Carrier et al., 2013; Parent et al., 2014; Beaudry et al., 2018; Figure 3). These hydrogeological contexts reflect major variations in topography, geological framework, groundwater recharge conditions, aquifer confinement, and groundwater flow dynamics across the region.

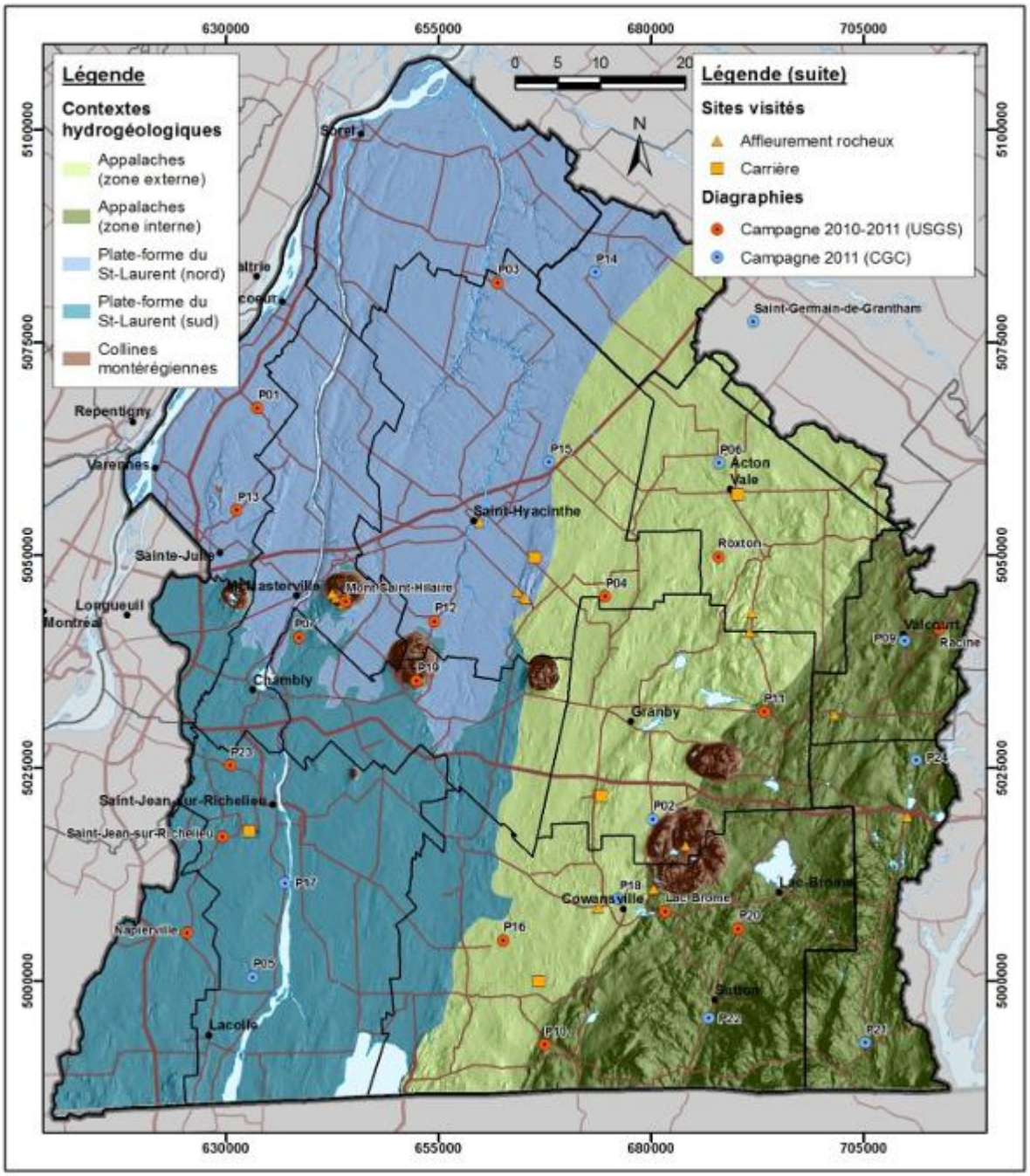


Figure 3: The Five Hydrogeological Contexts of the Montérégie Est Study Area (Carrier et al., 2013). Hydrogeological contexts of the Montérégie Est region, Québec, Canada, showing the five physiographic and hydrogeological subdivisions used for regional groundwater characterization: the Northern St. Lawrence Lowlands, Southern St. Lawrence Lowlands, Appalachian Piedmont (external Appalachian zone), Appalachian Uplands (internal Appalachian zone), and Monteregian Hills. Also shown are locations of geological outcrops, quarries, and borehole geophysical logging sites investigated during the PACES groundwater characterization program. Figure 3 is from Carrier et al. (2013).

The Montérégie Est region occupies a transitional position between the St. Lawrence Lowlands and Appalachian geological provinces, resulting in pronounced variability in physiography, bedrock geology, surficial sediments, recharge conditions, and groundwater flow dynamics across the study area (Parent et al., 2014; Carrier et al., 2013; Beaudry et al., 2018). The St. Lawrence Lowlands are underlain by relatively undeformed Cambrian–Ordovician sedimentary rocks consisting primarily of shale, dolostone, and limestone, whereas the Appalachian Piedmont and Uplands are composed of deformed and faulted metasedimentary rocks including sandstone, mudstone, limestone, and locally volcanic units associated with the Appalachian orogen. The region also contains the Monteregian Hills, which consist of Cretaceous alkaline intrusive complexes that form prominent topographic highs and locally influence groundwater recharge and flow patterns (Parent et al., 2014; Carrier et al., 2013; Beaudry et al., 2018).

Surficial sediment distributions also vary substantially between hydrogeological contexts. The northern St. Lawrence Lowlands are characterized by thick Champlain Sea clay and silt deposits that commonly create confined groundwater conditions, whereas the southern Lowlands contain more discontinuous marine sediments and till deposits. In contrast, the Appalachian Uplands are generally covered by thin and discontinuous till with thicker sediment accumulations restricted to glacial valleys, promoting predominantly unconfined conditions and enhanced groundwater recharge. Elevations increase from the relatively flat St. Lawrence Lowlands toward the Appalachian Piedmont and Uplands, creating regional hydraulic gradients that drive groundwater flow from upland recharge zones toward lower-elevation discharge areas in the Lowlands (Parent et al., 2014; Carrier et al., 2013; Beaudry et al., 2018).

Regional hydrogeological characterization of the Montérégie Est fractured bedrock aquifer system was conducted as part of Québec's PACES project, which aimed to improve understanding of groundwater resources across the province (Carrier et al., 2013; Beaudry et al., 2018). One of the outcomes of this large-scale study was the dataset which was used as the basis for a conceptual hydrogeological framework developed by Beaudry et al. (2018). This pre-existing model and data form the primary basis for this MSc project which incorporated both into a new numerical modelling and tracer investigation.

1.3.2 Groundwater–Surface-Water Interactions

Groundwater and surface water are hydraulically connected components of the hydrological cycle, and water may move either from an aquifer into a river, lake, wetland, or spring, or from a surface-water body into the underlying aquifer (Winter et al., 1998; Sophocleous, 2002). The direction of exchange is controlled primarily by the hydraulic-head difference between the surface-water body and the adjacent groundwater system, together with the hydraulic properties of the intervening sediments and bedrock (Winter et al., 1998; Sophocleous, 2002).

Where groundwater levels are higher than the water level in a stream, groundwater discharges into the channel, producing a gaining stream (Winter et al., 1998; Woessner, 2000). This groundwater contribution, commonly referred to as baseflow, can sustain streamflow between precipitation and snowmelt events and during dry periods (Winter et al., 1998). Whereas when stream or lake levels are higher than the surrounding groundwater level, surface water may infiltrate through the bed or banks and recharge the aquifer, producing a losing stream or losing reach (Winter et al., 1998; Sophocleous, 2002). A single river may contain both gaining and losing streams, and the direction of exchange may change seasonally as river stage and groundwater levels vary (Winter et al., 1998; Woessner, 2000).

The magnitude of groundwater–surface-water exchange depends on factors including hydraulic gradients, streambed hydraulic conductivity, sediment thickness, aquifer confinement, topography, and fracture connectivity (Sophocleous, 2002; Woessner, 2000). Permeable sediments and connected bedrock fractures may facilitate exchange, whereas clay, silt, and till deposits may restrict hydraulic communication between surface water and the underlying aquifer (Winter et al., 1998; Sophocleous, 2002). These exchanges may also affect groundwater residence time, water chemistry, and environmental-tracer distributions by mixing recently infiltrated surface water with groundwater travelling along longer subsurface flowpaths (Winter et al., 1998; Sophocleous, 2002).

Meyzonnat et al. (2016) documented these regional recharge–discharge relationships within the fractured-bedrock aquifer of the Bécancour watershed in southern Québec, where groundwater generally flows from Appalachian recharge areas toward discharge in tributaries of the St. Lawrence River. They also identified localized recharge in the St. Lawrence Lowlands where Champlain Sea clay deposits are absent or discontinuous, whereas thick marine clays restrict recharge to the underlying bedrock aquifer (Meyzonnat et al., 2016).

1.3.3 Beaudry et al. (2018) and the PACES project

The primary hydrogeological groundwater framework developed in the Montérégie Est region was developed by the *Programme d'acquisition de connaissances sur les eaux souterraines* (PACES) project, which was carried out between 2009 and 2013 and culminated in the publication of the regional hydrogeological atlas and groundwater resource assessment reports in the Québec region, which includes the Montérégie Est region (Carrier et al., 2013).

The PACES project carried out in Montérégie Est region compiled and integrated extensive geological, hydrogeological, geophysical, hydraulic, and major ion datasets to develop a regional characterization of the Montérégie Est aquifer system (Carrier et al., 2013). Existing data were supplemented through field investigations conducted during 2010, including groundwater sampling, hydraulic testing, geophysical surveys, piezocone investigations, and the installation of observation wells, primarily in the fractured bedrock aquifer (Carrier et al., 2013). These collected data were then used to produce a series of thematic maps, including surface and bedrock geology, unconsolidated sediment thickness, bedrock topography, confinement conditions, hydraulic conductivity distributions, regional piezometry in the fractured bedrock aquifer, groundwater recharge estimates etc. (Carrier et al., 2013). The developed three-dimensional geological and hydrostratigraphic maps can be viewed on the Québec groundwater atlas - Montérégie Est: PACES - Montérégie - Est (MDDELCC, 2015).

Several maps developed by the PACES study have been used to develop the flow model for this study; those layers will be introduced in Chapter 2. These datasets provided the first integrated regional-scale characterization of groundwater resources in Monteregie Est and formed the basis for future groundwater studies especially studies in the fractured bedrock aquifer, including the conceptual hydrogeochemical study that this study primarily built upon (Carrier et al., 2013). Building upon the regional geological and hydrogeological framework established through the PACES project, Beaudry et al. (2018) conducted a regional hydrogeochemical and isotopic investigation of the Montérégie Est fractured-bedrock aquifer to improve understanding of groundwater origins, hydrochemical evolution, recharge and discharge areas, and regional groundwater circulation. Groundwater was sampled from 206 bedrock wells during the 2010–2011 field campaign, and 190 samples meeting the required analytical and ionic-balance criteria were included in a multivariate statistical analysis based on 16 physicochemical and geochemical parameters (Beaudry et al., 2018). Hierarchical cluster analysis and principal component analysis were used to define eight hydrogeochemical water groups, while stable isotopes of water, tritium, radiocarbon, and carbon-isotope data provided

additional constraints on groundwater recharge conditions, residence times, mixing, and geochemical evolution (Beaudry et al., 2018). The study found an approximately 2,200 km² zone of brackish groundwater of Champlain Sea origin in the Northern St. Lawrence Lowlands and identified younger groundwater and important recharge areas in the Appalachian Uplands, the northern Appalachian Piedmont, and portions of the Southern St. Lawrence Lowlands (Beaudry et al., 2018). The resulting conceptual model provides the principal conceptual and tracer-based framework upon which the numerical groundwater-flow and transport models developed in the present study are based.

1.3.4 Previous Studies of the Montérégie Est Region

Previous investigations established the geological, hydraulic and geochemical framework of the Montérégie Est aquifer system. The regional PACES project integrated geological mapping, hydraulic testing, geophysics, groundwater levels, recharge estimates and groundwater chemistry to characterize the unconsolidated and fractured-bedrock aquifers and define five principal hydrogeological contexts (Carrier et al., 2013). Using samples from 206 bedrock wells, Beaudry et al. (2018) subsequently combined major-ion chemistry with $\delta^{2}H$, $\delta^{18}O$, ^{3}H, $\delta^{13}C$-DIC and ^{14}C-DIC to identify eight groundwater groups and develop a conceptual model of regional groundwater flow and geochemical evolution. Their results associated young groundwater with recharge in the Appalachian Uplands, Piedmont and southern Lowlands, suggested deeper flow from the Appalachian Uplands toward mixing zones near the Appalachian front and Monteregian Hills, and identified old brackish groundwater of Champlain Sea origin beneath the confined northern Lowlands. Laurencelle (2018) complemented these investigations by evaluating the depth-dependent hydraulic properties of the fractured-rock aquifer and numerically reconstructing its postglacial evolution, including Champlain Sea-water invasion and subsequent freshwater flushing. Together, these studies supplied the principal hydrostratigraphic, hydraulic, geochemical and isotopic foundation for the present groundwater-flow and age-tracer model, but they did not explicitly simulate the regional transport of ^{3}H and ^{14}C and compare modelled activities with the available isotope observations.

1.3.5 Previous Regional Studies Using Age Tracers Combined with ModelMuse

Environmental age tracers have been incorporated into regional MODFLOW-based models using both particle-tracking and solute-transport approaches. Reilly et al. (1994) combined ^{3}H and chlorofluorocarbon measurements with MODFLOW and MODPATH to constrain groundwater velocities in a shallow aquifer, demonstrating that calibration based

solely on hydraulic heads may not adequately reproduce groundwater residence times. Zhu (2000) explicitly simulated ^{14}C transport and radioactive decay to constrain regional recharge, whereas Sanford et al. (2004) incorporated measured ^{14}C activities and hydrochemical zones into the calibration of a MODFLOW–MODPATH model for the Middle Rio Grande Basin. In New Zealand, Gusyev et al. (2013) used MODFLOW–MT3DMS to simulate transient tritium transport, including its historical atmospheric input and first-order radioactive decay, and calibrated transport parameters using measured tritium concentrations in river baseflow. Gusyev et al. (2014) subsequently compared MT3DMS transport simulations with MODPATH-derived transit-time distributions, finding that both approaches reproduced measured tritium concentrations but represented groundwater-age distributions differently because MODPATH describes advective particle travel, whereas MT3DMS also represents mixing and dispersion. In southern Québec, Gagné et al. (2018) compared MODPATH travel times with $^{3}H/^{3}He$- and ^{14}C-derived residence times to validate a regional fractured-bedrock groundwater-flow model; the model reproduced younger $^{3}H/^{3}He$ residence times more successfully than older ^{14}C ages, with the latter discrepancy attributed partly to groundwater mixing and limitations in representing long regional flow paths. Collectively, these studies demonstrate that age tracers provide constraints on groundwater velocity, recharge, effective porosity, mixing and flow-path duration that cannot be obtained from hydraulic-head calibration alone.

1.4 Regional hydrogeological characterization

1.4.1 Hydrogeochemical Classifications Based on Beaudry et al. (2018)

From the initial five hydrogeological contexts as defined by Carrier et al. (2013) (Figure 3), Beaudry et al. (2018) further independently categorised groundwater samples into eight hydrochemical groups based on their aqueous geochemistry. For this, 43 wells were selected and classified into eight identified hydrogeochemical water groups based on multivariate statistical analysis (HCA) using Ward's linkage method and Euclidean distance to group similar samples, and principal component analysis (PCA) to identify dominant geochemical trends, applied to groundwater chemistry data including major ions (e,g, Ca^{2+}, Mg^{2+}, Na^{+}, Cl^{-}, HCO_3^{-}, SO_4^{2-}), physiochemical parameters (e.g., pH, total dissolved solids, redox conditions), and selected trace elements (e.g., Ba, B, Mn) (Beaudry et al., 2018). These groupings were further supported by isotopic data, including stable isotopes (δ^2H and $\delta^{18}O$) used to infer groundwater recharge origin and meteoric relationships, and environmental tracers (^3H and ^{14}C) used to constrain groundwater residence times and flow system evolution, with characteristic ranges of tracer values observed across the different water groups (Beaudry et al., 2018). These results were interpreted in the context of hydrogeological setting and spatial distribution across the study area (Beaudry et al., 2018). Five sampling wells among the 43 were categorized as "Other", indicating that no water group was assigned (Beaudry et al., 2018).

1.4.2 Hydrogeological Contexts

The eight hydrochemical groups as defined by Beaudry et al. (2018) provide a basis for identifying recharge areas, groundwater mixing zones, discharge regions, and groundwater residence time distributions throughout the study area (Figure 4; Beaudry et al., 2018).

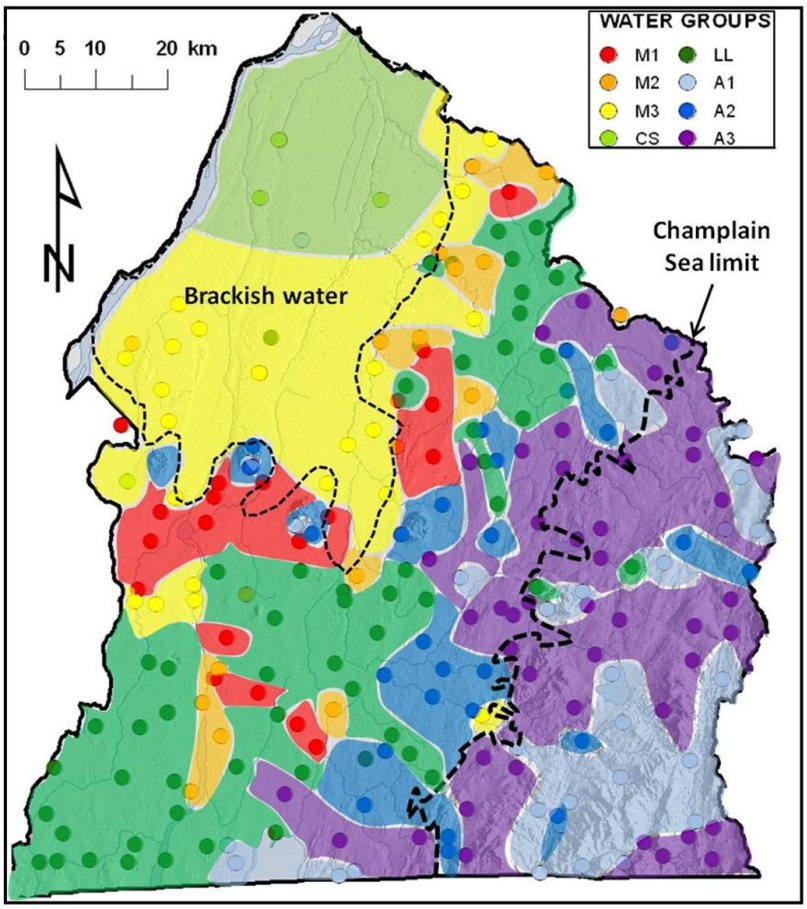


Figure 4. Spatial Distribution of Hydrochemical Water Groups and Brackish Groundwater Distribution in the Montérégie Est Region (Beaudry et al. 2018). Colored polygons represent groundwater classified into six hydrochemical water groups based on major ion chemistry, stable isotopes, radiocarbon (^{14}C), tritium (^{3}H), and dissolved gas data. Red areas (M1) represent recently recharged fresh groundwater with limited geochemical evolution. Orange areas (M2) indicate groundwater undergoing increasing water-rock interaction and hydrochemical evolution. Yellow areas (M3) correspond to chemically evolved brackish groundwater associated with long residence times and marine influence. Light blue areas (A1) represent recharge-dominated Appalachian groundwater characterized by relatively young groundwater and active circulation. Blue areas (A2) indicate intermediate groundwater evolution within the Appalachian region, while purple areas (A3) represent more geochemically evolved Appalachian groundwater associated with longer residence times and deeper circulation pathways. (CS) group is represented by light green color while the (LL) group is represented by dark green color. Colored circles indicate sampled groundwater wells

used for hydrochemical classification. The dashed line represents the maximum extent of the Champlain Sea transgression, illustrating the spatial relationship between marine sediments and the occurrence of brackish groundwater in the northwestern portion of the study area (Figure 4 is retrieved from Beaudry et al., 2018).

Hydrochemical and isotopic evidence presented by Beaudry et al. (2018) indicates that groundwater recharge occurs primarily within the Appalachian Uplands, portions of the Appalachian Piedmont, and selected areas of the Southern St. Lawrence Lowlands. Young groundwater characterized by elevated tritium concentrations, relatively modern radiocarbon signatures, and limited geochemical evolution was predominantly observed within these recharge regions (Beaudry et al., 2018). In comparison, groundwater located within confined portions of the Northern St. Lawrence Lowlands generally exhibited lower tritium concentrations, reduced radiocarbon activities, and greater evidence of water-rock interaction, indicating longer groundwater residence times and more extensive groundwater evolution (Beaudry et al., 2018). These observations suggest the presence of nested local, intermediate, and regional groundwater flow systems consistent with the conceptual framework originally proposed by Tóth (1963). Local groundwater flow systems are characterized by relatively short flowpaths connecting nearby recharge and discharge zones and generally contain younger groundwater and are located within primarily the Appalachian Uplands. While regional flow systems involve longer flowpaths extending across multiple hydrogeological contexts and are commonly associated with older groundwater, greater hydrochemical evolution, and increased groundwater mixing, primarily associated with the Northern St. Lawrence Lowland (Tóth, 1963; Beaudry et al., 2018).

One of the most significant hydrogeological features identified by Beaudry et al. (2018) is a regional brackish groundwater zone occupying approximately 2,200 km² within the northern St. Lawrence Lowlands. This zone occurs beneath thick Champlain Sea clay and silt deposits where confined groundwater conditions restrict modern recharge and groundwater renewal. Hydrochemical and isotopic evidence indicates that the brackish groundwater originated from marine water that invaded the fractured bedrock aquifer during the Champlain Sea transgression approximately 13,000–11,000 years ago and has subsequently been modified through groundwater mixing, geochemical evolution, and long-term flushing by fresh groundwater (Beaudry et al., 2018).

The brackish groundwater zone is primarily represented by the Champlain Sea (CS) and M3 hydrochemical groups (Beaudry et al., 2018). These waters are characterized by elevated sodium, chloride, and total dissolved solids concentrations, low tritium activities, and

geochemical signatures indicative of long groundwater residence times. The CS group most closely preserves the original geochemical signature of Champlain Sea water within the fractured bedrock aquifer, whereas the M3 group represents a more diluted and geochemically evolved groundwater resulting from mixing between residual marine groundwater and fresh groundwater (Beaudry et al., 2018).

Outside of the brackish groundwater zone, progressive flushing by fresh recharge water has promoted widespread Na-Ca ion exchange and groundwater freshening (Beaudry et.al, 2018). This process generated several intermediate hydrochemical groups characterized by Na-HCO_3 groundwater compositions that represent transitional stages between marine-influenced groundwater and modern fresh recharge waters (Beaudry et.al, 2018). Beaudry et al. (2018) interpreted these hydrochemical patterns as evidence of long-term basin-scale groundwater evolution and incomplete flushing of marine groundwater from the regional fractured bedrock aquifer system. Therefore, the present-day groundwater chemistry of the Montérégie Est region reflects both contemporary recharge processes and the persistent hydrogeochemical influence of post-glacial marine inundation, while the continued presence of brackish groundwater provides evidence for slow groundwater circulation, prolonged groundwater residence times, and the existence of regional groundwater flow systems within the northern St. Lawrence Lowlands (Beaudry et al., 2018).

Regional groundwater circulation is interpreted to occur from elevated recharge areas located within the Appalachian Uplands and Appalachian Piedmont toward lower-elevation discharge zones situated within the St. Lawrence Lowlands and major river valleys (Beaudry et al., 2018). Hydrochemical and isotopic evidence further suggests that portions of the groundwater system participate in relatively deep basin-scale circulation pathways that extend beyond local watershed boundaries (Beaudry et al., 2018). Beaudry et al. (2018) proposed that groundwater may flow from the Appalachian Uplands toward mixing zones associated with Appalachian frontal thrust faults, the Monteregian Hills, and confined portions of the Lowlands where regional groundwater discharge and mixing occur. This conceptual model of basin-scale groundwater circulation forms the foundation for the MODFLOW-NWT, MODPATH 7, and MT3D-USGS simulations developed in the present study and provides a framework for evaluating groundwater residence times, groundwater evolution, and environmental tracer behaviour along regional groundwater flowpaths.

1.4.3 Flow regime predictions

Previous regional-scale, two-dimensional groundwater-flow and transport simulations of the Montérégie Est fractured-bedrock aquifer predicted a nested Tóthian flow system composed of local, intermediate, and regional flow subsystems (Laurencelle et al., 2013, as cited in Beaudry et al., 2018). In a Tóthian system, short and shallow local flowpaths are superimposed on progressively longer and deeper intermediate and regional flowpaths driven by differences in topographic elevation. The hydrogeochemical and isotopic results of the 2010–2011 PACES campaign subsequently provided field evidence supporting this general framework and allowed the original conceptual flow model to be refined (Beaudry et al., 2018).

Young, relatively unevolved Ca–HCO_3 groundwaters represented by water groups A1 and LL were interpreted as evidence of active recharge and comparatively short and shallow flow pathways. A1 occurs primarily in the Appalachian Uplands and locally around the Monteregian Hills, whereas LL represents slower recharge within the Southern St. Lawrence Lowlands. The more evolved A3 groundwater has longer radiocarbon residence times and was interpreted as either the product of a longer and relatively deeper Appalachian flowpath originating partly from A1 recharge, or as a mixture of modern recharge with older groundwater. A3 groundwater was inferred to evolve toward the A2 water group as deeper Appalachian groundwater discharges in the Piedmont and enters areas formerly affected by the Champlain Sea. This relationship supports an intermediate-to-regional freshwater flow pathway originating in the Appalachian Uplands and emerging along the western Appalachian margin.

Around the Monteregian Hills and parts of the Southern St. Lawrence Lowlands, the evolved M1 water group may similarly reflect contributions from long and relatively deep groundwater flow, potentially facilitated by fractured dykes and other structural features. However, Beaudry et al. (2018) noted that the origin of M1 remained uncertain because it contains both evidence of long residence time and detectable tritium, indicating mixing with recent recharge. Water groups M2 and M3 were interpreted mainly as transitional mixtures between freshened groundwater and either locally recharged LL water or older CS water. The CS group, located beneath the thick Champlain Sea deposits of the Northern St. Lawrence Lowlands, represents old brackish groundwater preserved under confined conditions and was considered to have little significant active groundwater circulation. Therefore, the CS zone should be viewed primarily as a stagnant paleo-groundwater body rather than as the discharge end of an active regional freshwater flow system (Beaudry et al., 2018).

1.5 Existing Knowledge Gaps

The PACES project, and the resulting data which was interpreted by Beaudry et al. in 2018 in the qualitative and conceptual model have substantially improved the understanding of the Montérégie Est aquifer system. However, several study gaps still remain regarding groundwater flow dynamics, groundwater residence times, and the long-term evolution of groundwater chemistry.

The primary knowledge gap addressed by this study is the absence of a quantitative regional-scale groundwater flow and transport model capable of incorporating groundwater age tracers within the Montérégie Est aquifer system to generate a spatio-temporal hydrogeologic flow model. Although the PACES project established the geological and hydrogeological framework of the region, its primary focus was regional characterization rather than numerical groundwater flow and transport modelling (Carrier et al., 2013). Within Montérégie Est, ^{3}H and ^{14}C-DIC measurements collected through the PACES program have been used to distinguish recently recharged groundwater from older groundwater, estimate groundwater residence-time ranges, evaluate groundwater mixing and hydrochemical evolution, and refine conceptual interpretations of recharge and regional groundwater circulation (Carrier et al., 2013; Beaudry, 2013; Beaudry et al., 2018). However, these published regional studies reviewed here focused primarily on groundwater-flow behaviour, hydraulic properties, and the postglacial invasion and flushing of Champlain Sea water, rather than explicitly simulating ^{3}H and ^{14}C as advective–dispersive, radioactively decaying tracers (Laurencelle et al., 2013, 2016, 2017; Laurencelle, 2018). Therefore, the regional spatial distribution of groundwater age tracers and their relationship to simulated groundwater flow systems remain largely unexplored. Specifically, to date, no published study has developed a coupled and quantitative regional groundwater flow and transport model for the Montérégie Est aquifer system capable of evaluating and reproducing both flow pathways and groundwater residence time, validated via observed ^{14}C and ^{3}H distributions. This study addresses this gap through the integration of groundwater flow modelling, particle tracking, groundwater transport simulation, and historic and newly generated environmental tracer and geochemical data to evaluate groundwater residence times and regional groundwater flow behaviour.

The second knowledge gap relates to the temporal evolution of groundwater geochemistry and groundwater residence times. Climate change and anthropogenic activities are altering groundwater systems by modifying the amount, intensity, and seasonality of precipitation, increasing evaporative demand, and shifting the seasonal timing of runoff and

recharge. These changes can affect groundwater recharge, discharge, storage, and regional flow patterns, although the magnitude and direction of the response vary according to climatic aridity, aquifer properties, and the dominant recharge mechanism (Epting et al., 2021; Kuang et al., 2024; Berghuijs et al., 2024). Groundwater recharge may be particularly sensitive in regions where potential evapotranspiration is similar to or slightly greater than precipitation, such that relatively small increases in aridity can produce disproportionately large reductions in recharge (Berghuijs et al., 2024). In addition, groundwater abstraction, irrigation, land-use change, and urban development may further modify recharge, groundwater storage, and regional flow regimes, either intensifying or obscuring climate-driven changes (Kuang et al., 2024; Berghuijs et al., 2024). However, despite the considerable regional dependence on groundwater, any similar temporal changes remain unclear for the Monteregie Est region. Specifically, primary interpretations of groundwater conditions in the fractured bedrock aquifer in this region are based on data collected during the 2010 PACES field campaign. However, no information has been available regarding any change over time in groundwater chemistry, stable isotopes, and environmental tracer for the region. This study also will address this through the generation of a new dataset which will allow assessment of groundwater temporal changes over a 15-year interval in groundwater chemistry and age tracer signatures through resampling of several selected wells present in the PACES dataset.

1.6 Study Objectives

1. Quantify regional groundwater-flow regimes, flow directions, and travel times in the Montérégie Est fractured-bedrock aquifer by integrating numerical modelling with published hydraulic, hydrochemical, and isotopic data from 2010.
2. Evaluate and refine predicted groundwater-flow and residence-time patterns by comparing model results with measured ^{14}C, ^{3}H, hydraulic, and hydrochemical observations from 2010 and an independent field dataset collected in 2025.
3. Determine how water–rock interactions and carbonate dissolution influence groundwater chemistry and age-tracer evolution, particularly the interpretation of ^{14}C and ^{3}H as indicators of groundwater residence time.
4. Assess temporal changes in groundwater chemistry and isotopic composition between 2010 and 2025 and determine what these changes indicate about the stability of regional groundwater-flow conditions.
5. Evaluate the principal limitations, sensitivities, and uncertainties affecting regional groundwater-flow and tracer-transport predictions, including aquifer simplification, boundary conditions, hydraulic properties, recharge, groundwater mixing, and tracer-transport assumptions.

Chapter 2. Numerical Modelling Framework

2.1 Overview of Numerical Modelling Framework

2.1.1 General Modelling Framework

Numerical modelling was conducted using ModelMuse, a graphical user interface developed by the U.S. Geological Survey for the construction and visualization of MODFLOW-based groundwater models (Winston, 2009). Within this framework, MODFLOW-NWT was used to simulate regional groundwater flow and hydraulic head distributions under steady-state conditions (Niswonger et al., 2011), MODPATH-7 was used to simulate advective groundwater flowpaths and regional particle tracking (Pollock, 2016), and MT3D-USGS was used to simulate groundwater age-tracer transport, mixing, and radioactive decay processes for ^{3}H and ^{14}C (Bedekar et al., 2016). Together, these coupled modelling approaches were used to evaluate regional groundwater flow dynamics, groundwater residence times, and tracer evolution within the fractured bedrock aquifer system of the Montérégie Est region. The specific parameters for MODFLOW-NWT, MODPATH-7 and MT3D-USGS are outlined in the following sections.

2.1.2 Summary of Numerical Modelling Parameters and Components

The hydrogeologic components/parameters which were incorporated into MODFLOW-NWT, MODPATH-7 and MT3D-USGS are outlined in Table 1.

Table 1. Summary of the major groundwater flow and solute transport model parameters and components used in the MODFLOW-NWT, MODPATH 7, and MT3D-USGS numerical modelling framework. Brief descriptions are provided to illustrate the hydrogeological role of each parameter and its influence on simulated groundwater flow, particle tracking, tracer transport, mixing, and groundwater residence time estimation within the Montérégie Est fractured bedrock aquifer system.

Model parameter / component	Function in the model	Parameters, units, and values used
Model domain and spatial discretization	Defines the physical extent of the study area and divides it into finite-difference cells in which the groundwater-flow and transport equations are solved.	Domain ≈ 9,218 km²; structured grid: 250 m × 250 m; EPSG:32198; length unit: m.
Model time unit	Defines the time unit used for flow, particle tracking, transport, hydraulic conductivity, recharge, and radioactive decay.	Years.
Groundwater-flow temporal configuration	Determines whether hydraulic heads and groundwater flows vary with time.	Steady state.
Storage parameters	Specific yield and specific storage describe changes in groundwater storage during transient simulations.	Not applicable to the steady-state flow solution.
Active model domain and external boundaries	Defines the cells in which groundwater flow and transport are simulated and prevents flow through inactive areas outside the study boundary.	Cells inside the Montérégie Est boundary active; cells outside inactive/no-flow.
Number of model layers	Represents the principal hydrogeological units in the subsurface.	2 layers: Upper Aquifer and Middle Aquifer.
Upper Aquifer top elevation	Defines the upper surface of the fractured-bedrock layer.	PACES bedrock-surface raster: topographie_roc.tif.

Upper Aquifer bottom elevation	Defines the thickness of the upper fractured-bedrock layer while preventing the initial head from occurring at or below the layer bottom.	$z_{bot,1} = z_{top} - 100$ m where $h_0 > z_{top} - 100$ m; otherwise $z_{bot,1} = h_0 - 10$ m.
Middle Aquifer bottom elevation	Defines the lower boundary of the regional groundwater-flow model.	−500 m above sea-level datum.
Initial hydraulic head	Provides the starting estimate used by the MODFLOW-NWT nonlinear solver. It is not a fixed-head boundary and does not necessarily equal the final simulated head.	PACES piezometric raster: Piézométrie roc.tif.
Horizontal hydraulic conductivity, Kx	Controls the ease of groundwater movement in the model-row direction.	PACES hydrogeological-context values scaled using scaling factor = 0.135335.
Horizontal hydraulic conductivity, Ky	Controls groundwater movement in the model-column direction.	$K_y = K_x$.
Vertical hydraulic conductivity, Kz	Controls vertical groundwater movement and represents reduced vertical fracture connectivity relative to horizontal connectivity.	$K_z = K_x/20$.
Deep-layer hydraulic conductivity	Represents low-permeability, matrix-dominated groundwater flow in the deeper bedrock layer.	$K_x = K_y = K_z = 0.0315576$ m/year.
Upstream Weighting package	Assigns hydraulic properties and supports the treatment of unconfined conditions and drying cells in MODFLOW-NWT.	UPW package activated.
Groundwater recharge	Represents water entering the fractured-bedrock groundwater system from precipitation and infiltration.	PACES SWAT recharge raster × 0.135335; units: m/year.
Drain boundary locations	Represents one-way groundwater discharge from the aquifer where simulated head rises above the assigned drain elevation.	PACES preferential-discharge zones.

Drain elevation	Defines the hydraulic elevation above which groundwater may discharge through a drain boundary.	hdrn = model top/bedrock-surface elevation.
Drain discharge equation	Calculates groundwater outflow through the drain when simulated head exceeds the drain elevation.	QDRN = CDRN(h − hdrn) for h > hdrn; otherwise QDRN = 0.
Drain conductance	Controls the rate at which groundwater leaves the aquifer for a given head difference above the drain elevation.	ModelMuse Calculated conductance; CDRN = K_zA/M.
MODFLOW-NWT head convergence tolerance	Defines the maximum acceptable change in hydraulic head between nonlinear solver iterations.	HEADTOL = 0.0001 m.
MODFLOW-NWT flux convergence tolerance	Defines the acceptable residual flow imbalance used by the nonlinear solver when determining convergence. It is not the overall percentage groundwater-budget discrepancy.	FLUXTOL = 500 m^3/year.
Maximum nonlinear iterations	Limits the number of outer Newton iterations available to achieve convergence.	MAXITEROUT = 500.
Dry-cell smoothing parameter	Smooths the transition between wet and dry conditions and improves numerical stability in unconfined cells.	THICKFACT = 0.00001.
MODFLOW-NWT linear solver	Solves the linearized groundwater-flow equations during each Newton iteration.	LINMETH = 2 (Chi-MD).
Groundwater-flow convergence	Confirms that the steady-state hydraulic-head solution satisfied the specified numerical tolerances.	Converged steady-state solution.
Effective porosity, n_e	Represents the interconnected mobile pore and fracture volume through which groundwater and dissolved tracers move. It controls seepage velocity and particle travel time but does not directly	n_e = 0.02.

	change the MODFLOW hydraulic-head solution.	
MODPATH 7 simulation type	Determines the form of particle-tracking output.	Pathlines.
MODPATH tracking direction	Determines whether particles move with or against the simulated groundwater-flow direction.	Forward.
MODPATH particle starting locations	Defines where groundwater particles enter the particle-tracking simulation.	Centres of PACES-defined major recharge zones; release time = 0.
MODPATH recharge-face treatment	Determines where areal recharge enters the uppermost active cells for particle tracking.	IRCHTP top-face recharge option.
MODPATH weak-sink treatment	Determines whether particles terminate or continue through cells containing minor groundwater sinks.	Pass Through.
MODPATH zone restrictions	Determines whether particles terminate when entering user-defined model zones.	Disabled.
MODPATH maximum tracking time	Defines the maximum time over which particles may be tracked.	60,000 years.
MT3D-USGS Basic Transport package	Defines transport-grid information, porosity, concentration arrays, transport periods, output times, and transport time-step controls.	BTN package activated; porosity = 0.02.
MT3D-USGS governing transport equation	Represents advection, hydrodynamic dispersion, source and sink mixing, molecular diffusion, and first-order radioactive decay.	Advection–dispersion–reaction equation with first-order radioactive decay.
Advection package	Simulates transport of tracer mass carried by moving groundwater.	ADV activated; MIXELM = −1 (third-order TVD).

Longitudinal dispersivity, αL	Controls mechanical spreading parallel to the principal groundwater-flow direction.	αL = 376.09 m.
Horizontal transverse dispersivity ratio, TRPT	Defines horizontal transverse dispersivity relative to longitudinal dispersivity. TRPT is a dimensionless ratio, not a dispersivity in metres.	TRPT = 0.10; αTH = 37.61 m.
Vertical transverse dispersivity ratio, TRPV	Defines vertical transverse dispersivity relative to longitudinal dispersivity. TRPV is dimensionless.	TRPV = 0.03; αTV = 11.28 m.
Cross-dispersion terms	Allow dispersion to occur in multiple spatial directions rather than only parallel to the model axes.	Enabled.
Molecular diffusion coefficient, DMCOEF	Represents tracer movement caused by concentration gradients within the equivalent porous-medium mobile domain. It does not explicitly simulate fracture–matrix mass transfer.	DMCOEF = 0.00315576 m²/year.
Longitudinal hydrodynamic-dispersion coefficient	Combines velocity-dependent mechanical dispersion and molecular diffusion in the direction of groundwater flow.	$DL = \alpha L v_e + DMCOEF$.
Dispersion package	Calculates the hydrodynamic-dispersion tensor using longitudinal and transverse dispersivities, groundwater velocity, and molecular diffusion.	DSP activated.
Source/Sink Mixing package	Assigns tracer concentrations to recharge and other source or sink terms already defined in the MODFLOW flow model. It adds tracer mass without changing MODFLOW recharge rates or hydraulic heads.	SSM activated; specified-concentration sources: ITYPE = −1.

^{3}H recharge concentration	Defines the tritium activity assigned to direct modern recharge entering major recharge zones.	14 TU in PACES-defined major recharge zones.
^{14}C recharge concentrations	Defines the radiocarbon activity assigned to recharge sources entering the transport model.	0, 35, 38, 58, and 100 pMC, assigned by recharge-zone confinement and hydrochemical group.
Reaction package	Simulates radioactive decay of ^{3}H and ^{14}C during transport.	RCT activated; first-order decay; ISOTHM = 0.
Radioactive-decay equation	Calculates the reduction in tracer concentration caused by radioactive decay.	$C(t) = C_0e^{(-\lambda t)}$.
^{3}H decay constant	Represents radioactive decay of tritium.	$t_{1/2}$ = 12.32 year; λ = 0.05624 year^{-1}.
^{14}C decay constant	Represents radioactive decay of radiocarbon.	$t_{1/2}$ = 5,730 year; λ = 0.00012097 year^{-1}.
MT3D-USGS GCG solver	Iteratively solves the numerical tracer-transport equations at each transport time step.	GCG package activated.
^{3}H transport-simulation time	Defines the period over which the tritium concentration field was allowed to develop under the steady-state groundwater-flow field.	150 years.
^{14}C transport-simulation time	Defines the period over which the radiocarbon concentration field was allowed to migrate and decay under the steady-state groundwater-flow field.	60,000 years.
Flow–transport coupling	Transfers hydraulic heads and cell-by-cell groundwater-flow rates from MODFLOW-NWT to MT3D-USGS.	Converged MODFLOW-NWT flow field used by MT3D-USGS.
Péclet-number diagnostic	Evaluates the relative importance of advective transport compared with hydrodynamic dispersion.	Pe = 13.29; grid-cell analysis used Δx = 250 m.

2.2 Modelling Platform

2.2.1 MODFLOW-NWT Flow Model Setup

To successfully develop a regional hydrogeological numerical model, the groundwater flow system must first be established using MODFLOW-NWT to simulate regional groundwater flow dynamics and hydraulic head distributions. The MODFLOW-NWT solver was selected due to the heterogeneous fractured bedrock conditions, partially unconfined flow behaviour, and drying and rewetting processes present within the model domain. Solver parameters were selected to prioritize numerical stability while preserving physically realistic regional groundwater flow conditions. This initial model setup defines the fundamental hydrogeological framework of the simulation, including model discretization and grid cell dimensions, temporal configuration (steady-state or transient conditions), hydrostratigraphic layering, recharge and discharge processes, hydraulic properties, boundary condition implementation, and MODFLOW-NWT packages.

2.2.2 Basic Model Configuration

The MODFLOW-NWT model was implemented in ModelMuse as a steady-state, finite-difference groundwater flow model using a structured grid with a uniform cell size of 250 m × 250 m in the NAD 1983 Quebec Lambert coordinate system (EPSG:32198). The model domain covers approximately 9,218 km² and was discretized into two hydrogeological layers representing the fractured upper bedrock aquifer and the deeper bedrock matrix system. Length units in the model were defined in meters, consistent with the EPSG:32198 projection system and the spatial resolution of the regional geospatial datasets used in this study. Time units were defined in years, which is appropriate for regional-scale groundwater flow and groundwater age-tracer simulations involving ^{3}H and ^{14}C, while also allowing long simulation periods and radioactive decay processes to be represented more efficiently and interpreted more naturally. A head convergence tolerance (HEADTOL) of 0.0001 m and flux convergence tolerance (FLUXTOL) of 500 m³/year were used (Supplementary Material 1). The maximum number of nonlinear outer iterations (MAXITEROUT) was set to 500, while the dry-cell smoothing parameter (THICKFACT) was assigned a value of 0.00001 to improve numerical stability during transitions between saturated and unsaturated conditions. The Chi-MD linear solver option (LINMETH = 2) was selected for solving the asymmetric system of equations generated by the Newton–Raphson formulation. Detailed solver parameter ranges and sensitivity testing are provided in the Supplementary Material (See Supplementary Material 1).

2.2.3 Model Layer Configuration

The groundwater flow model was represented as a two-layer system consisting of an Upper Aquifer and a Middle Aquifer. The conceptual configuration of the two layered model setup is shown in figure 5 below for better understanding of the model setup (Figure 5). The Upper Aquifer represents the actively fractured bedrock zone, while the Middle Aquifer represents the deeper low-permeability bedrock matrix. The top surface of the Upper Aquifer (Model_Top) was defined using the raster dataset *topographie_roc.tif*, representing the regional bedrock surface elevation across the Montérégie Est study area (Carrier et al., 2013; Figure 6). It is important to note that in the model proposed here the upper model layer begins at the bedrock surface rather than at the ground surface because the model was designed specifically to represent the regional fractured-bedrock aquifer. Similar bedrock-focused regional modelling approaches have represented the fractured-rock aquifer as an equivalent porous medium while excluding overlying unconsolidated units when those units were outside the study objective or insufficiently characterized (Gagné et al., 2018). In Montérégie Est, the available regional data were insufficient to consistently define the heterogeneous thickness, hydraulic properties, continuity, and groundwater levels of the unconsolidated deposits as a separate model layer; including such a layer would therefore have introduced additional poorly constrained parameters. Recharge calculated at the bedrock surface was therefore applied directly to the upper fractured-bedrock layer. This simplification is appropriate for evaluating regional bedrock flow, but it may overlook local shallow flow paths, perched groundwater, lateral flow within unconsolidated deposits, and spatially variable exchanges between the unconsolidated and bedrock aquifers. The base of the fractured bedrock layer (Upper_Aquifer_Bottom) was defined using a conditional expression incorporating both bedrock elevation and the regional piezometric surface (Carrier et al., 2013) (See Supplementary Material 2). This approach allowed the thickness of the fractured bedrock layer to vary spatially while limiting the maximum fractured zone thickness to 100 m, consistent with the conceptual depth of active bedrock fracturing within the region (Laurencelle (2018). In areas of lower hydraulic head, the base of the fractured zone was defined relative to the initial hydraulic head distribution using a hydraulic head offset of initial hydraulic head – 10 m, improving numerical stability by preventing simulated hydraulic heads from falling below the lower boundary of the upper model layer during MODFLOW-NWT simulations. The initial hydraulic head is set using the raster dataset Piézométrie roc.tif, representing the elevation of the regional fractured-bedrock aquifer's hydraulic head relative to mean sea level and indicates

the general direction of groundwater flow from areas of higher head toward areas of lower head (Carrier et al., 2013; Figure 7).

The Middle Aquifer was defined beneath the fractured bedrock layer and represents deeper groundwater flow dominated by low-permeability bedrock matrix conditions. The bottom elevation of the model domain (Middle_Aquifer_Bottom) was assigned a constant elevation of –500 m below sea level following preliminary sensitivity testing of alternative model depths. This depth was selected to adequately capture the dominant regional groundwater flow system while avoiding unnecessary computational complexity and poorly constrained deep groundwater flow processes. Other depths testings shown in the Supplementary Material Section 3.

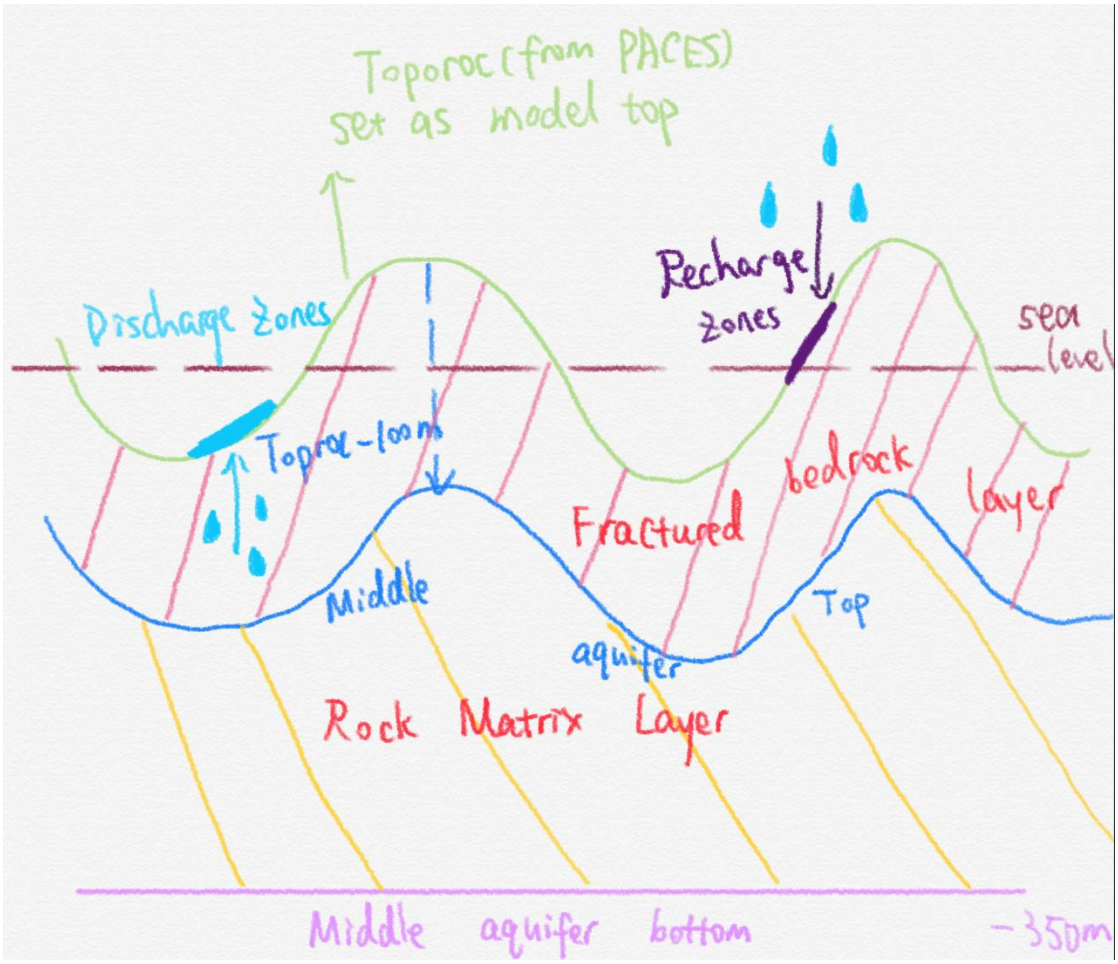


Figure 5. Conceptual figure of the two layered model. Here green shows the top of the fractured bedrock layer which was set up as Toporoc from the PACES dataset. Blue is the bottom of the fractured bedrock layer and the top of the bedrock matrix layer. The purple indicates bedrock matrix layer bottom and is -500m below asl.

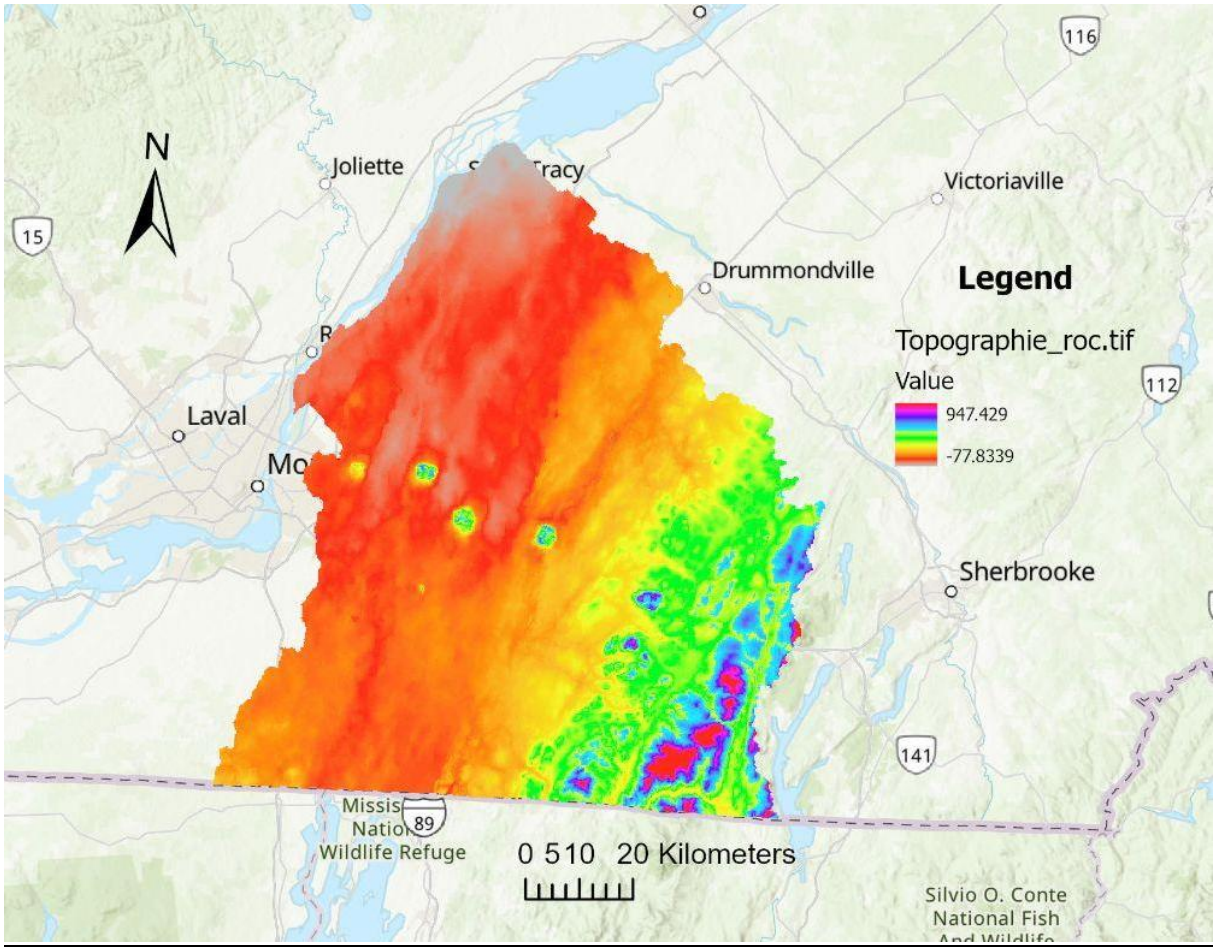


Figure 6. Bedrock-surface topography of the Montérégie Est study area. Bedrock-surface elevation is expressed in metres relative to mean sea level and was estimated by subtracting the total thickness of unconsolidated deposits from the digital elevation model (Carrier et al., 2013). The resulting 250 m × 250 m raster generally follows surface topography but identifies sediment-filled Appalachian valleys, the Monteregian Hills, and a northward-deepening bedrock surface toward Lake Saint-Pierre. Figure 5 is redrawn in ArcGIS Pro from Carrier et al. (2013).

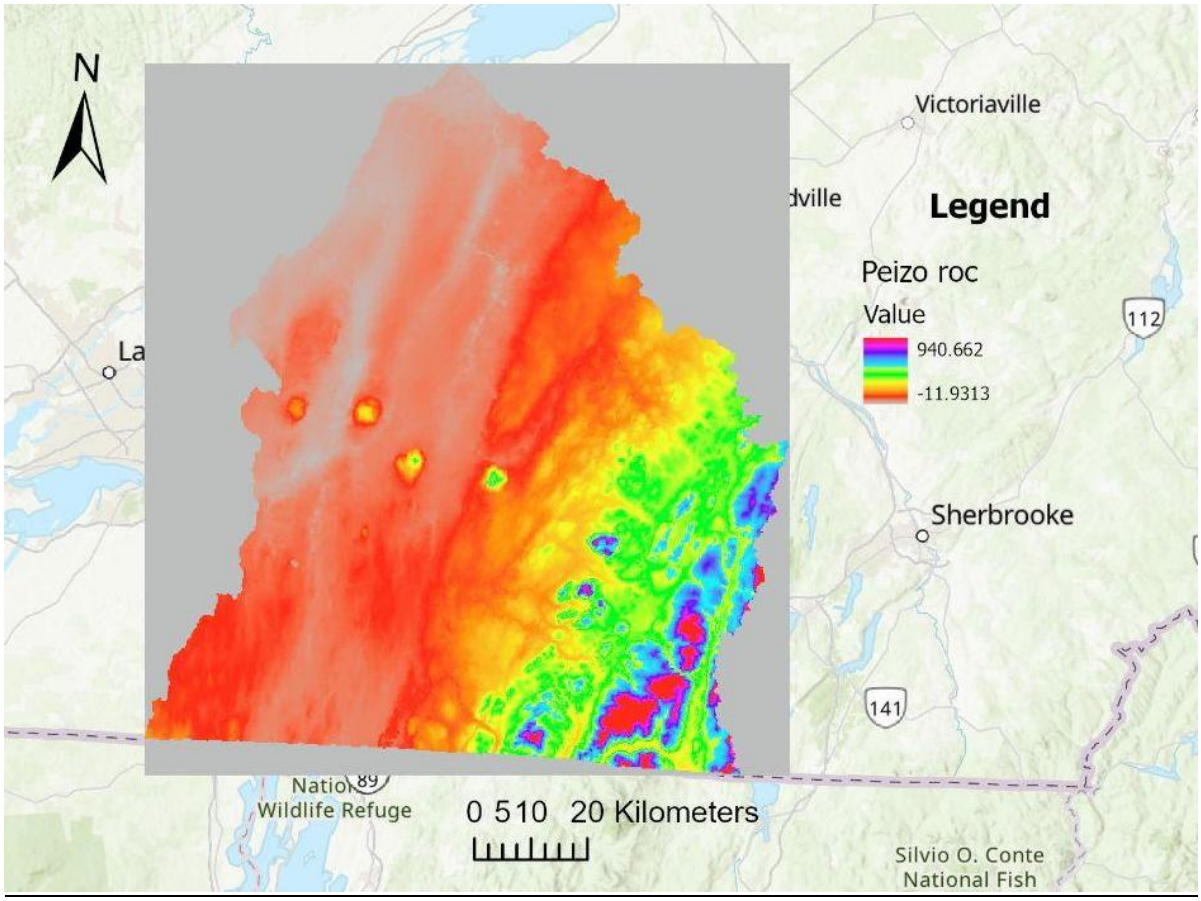


Figure 7. Regional piezometric surface of the fractured-bedrock aquifer in the Montérégie Est study area. Piezometric elevations are expressed in metres relative to mean sea level and were interpolated from selected and validated groundwater-level measurements in wells completed in bedrock (Carrier et al., 2013). Groundwater flow is generally directed from areas of higher hydraulic head toward areas of lower hydraulic head. The original 250 m × 250 m raster dataset was retrieved from Carrier et al. (2013), processed and redrawn in ArcGIS Pro, and used to define the initial hydraulic-head distribution in the MODFLOW-NWT groundwater-flow model developed in this study.

2.2.4 Hydraulic Parameters

Hydraulic conductivity (K) is the proportionality coefficient in Darcy's law that describes the capacity of a geological medium to transmit water under a hydraulic gradient and depends on both the properties of the medium and the fluid moving through it (Lohman et al., 1972). In ModelMuse, (K_x) and (K_y) represent hydraulic conductivity along the model-row and model-column directions, respectively, whereas (K_z) represents vertical hydraulic conductivity (Winston, 2024). Hydraulic conductivity values (K_x, K_y, and K_z) for the fractured-bedrock layer were assigned based on hydrogeological conductivity zones derived from the PACES project and supporting values reported for the Montérégie Est region (Carrier et al., 2013; Laurencelle, 2018). Hydraulic conductivity values (K_x, K_y, and K_z) for the fractured bedrock layer were assigned based on hydrogeological conductivity zones derived from the PACES project and supporting literature values for the Montérégie Est region (Carrier et al., 2013; Laurencelle, 2018). The PACES conductivity map itself was not directly implemented because variations in drilling depth between hydrogeological contexts and geological units introduce bias in the regional conductivity distribution (Laurencelle, 2018). Instead, representative horizontal hydraulic conductivity (K_x) values were assigned according to the hydrogeological-context classification established by the PACES project. For each context, the assigned value corresponds to the median of the range of hydraulic-conductivity values derived from field-based hydraulic tests and compiled by PACES, thereby grounding the parameterization in regional observations rather than assumed literature values (Carrier et al., 2013; Laurencelle, 2018). Because the fractured-bedrock aquifer was represented using an equivalent porous medium (EPM) approach, individual fractures were not simulated explicitly; consequently, field-constrained effective $K_x$values were required to represent the aggregate hydraulic behaviour of the fracture network at the 250-m model-cell scale. Previous statistical analyses found no significant differences among geological units within the same hydrogeological context, supporting the use of one median, field-constrained $K_x$value for each context (Laurencelle, 2018).

A systematic decrease in fractured bedrock hydraulic conductivity with depth has been documented throughout the Montérégie Est region due to decreasing fracture density with depth (Laurencelle, 2018). This gradual decrease represents the interpreted real-world hydrogeological condition; it was not implemented as a continuously varying hydraulic-conductivity profile within the MODFLOW model. Instead, because the simulated fractured-bedrock zone was represented by a single model layer, MODFLOW required one effective

hydraulic-conductivity value for each hydrogeological zone rather than a series of conductivity values that decreased vertically within the layer. As the fractured-bedrock zone was represented in the model by a single model layer with a thickness smaller than the 250 m horizontal grid spacing, a simplified exponential depth-scaling relationship was applied to the spatially distributed K_x values to approximate the regional decrease in hydraulic conductivity with depth. Therefore, a simplified exponential depth-scaling relationship was applied to the median, field-constrained surface K_x value assigned to each hydrogeological zone to approximate the regional decrease in hydraulic conductivity with depth. Following Laurencelle (2018), the reduction in hydraulic conductivity with depth was represented using (Equation 9):

$$K_x(z) = K_{x,0} \cdot e^{-\lambda z} \quad (9)$$

Where $K_{x,0}$ represents surface hydraulic conductivity (m/year) (Carrier et al., 2013), z is depth (m), and a value of λ=0.04 m^{-1} was adopted as a modelling approximation to represent the decrease in hydraulic conductivity with depth. This value was derived from the empirically determined fracture-density decay coefficient reported by Laurencelle (2018), rather than from a directly measured hydraulic-conductivity decay relationship. Its application in the K_z therefore assumes that the regional decrease in hydraulic conductivity broadly follows the observed decrease in fracture density with depth. The equation was used only to calculate a single reduction factor at the representative depth of the modelled fractured-bedrock layer; consequently, it did not replicate a gradual cell-by-cell decrease in K_x within that layer proposed for this natural system. Its application therefore assumes that the regional decrease in effective hydraulic conductivity broadly follows the observed decrease in fracture density with depth.

In this study, conductivity conditions at 50 m depth were selected as representative of the fractured bedrock layer, resulting in a decay factor of (Equation 10):

$$e^{-\lambda z} = e^{-0.04 \times 50} = e^{-2} = 0.135335283236613 \quad (10)$$

For each hydrogeological zone, the median surface $K_{x,0}$ value was multiplied by 0.135335, producing one effective K_x value that was applied throughout that zone in the single fractured-bedrock layer. Thus, the regional depth-decay relationship informed the selection of the modelled effective conductivity, but the continuous real-world decrease with depth was not explicitly resolved by the model. This simplified exponential scaling approach provided stable MODFLOW-NWT convergence behaviour while improving agreement between simulated and measured groundwater heads and age-tracer distributions during MT3D-USGS calibration and

sensitivity testing (See Supplementary Material 4). The same scaling factor was also applied to recharge and DRN package inputs to maintain consistency between groundwater recharge, discharge and conductivity conditions at the conceptual depth represented by the fractured bedrock layer (See Supplementary Material 4). Horizontal anisotropy was simplified by assigning $K_y=K_x$, while vertical hydraulic conductivity was assigned as (Equation 11):

$$K_z=K_x/20 \quad (11)$$

to represent reduced vertical fracture connectivity relative to horizontal groundwater flow. Isotropic hydraulic conductivity value of 0.0315576 m/year to approximate matrix-dominated groundwater flow conditions based on a conductivity of 0.000000001 m/s subtracted by Laurencelle (2018) (See Supplementary Material 5). No directional horizontal anisotropy was represented in the model; instead, horizontal hydraulic conductivity was assumed isotropic by setting ($K_y = K_x$), while vertical hydraulic conductivity was reduced according to Equation 11 to represent lower vertical fracture connectivity relative to horizontal groundwater flow.

Recharge was applied through the MODFLOW Recharge (RCH) package using the spatially distributed mean annual recharge estimated for the Montérégie Est region with the Soil and Water Assessment Tool (SWAT), a semi-distributed watershed model that simulates surface and subsurface components of the hydrological cycle (Carrier et al., 2013). The SWAT-derived recharge layer was selected instead of the layer produced using the Hydrologic Evaluation of Landfill Performance (HELP) model, a one-dimensional water-balance model used to simulate vertical infiltration through soil and surficial-material profiles. In the PACES study, HELP recharge represented water infiltrating vertically to the bedrock surface, whereas SWAT recharge represented water transferred to the deep aquifer after accounting for water returning to streams through the shallow aquifer. The SWAT estimates were therefore considered more representative of recharge entering the regional fractured-bedrock groundwater-flow model (Carrier et al., 2013). The SWAT recharge layer was selected instead of the HELP-derived layer because SWAT represents water transferred to the deep aquifer, which more closely corresponds to recharge entering the regional fractured-bedrock groundwater-flow model, whereas HELP represents vertical infiltration reaching the bedrock surface (Carrier et al., 2013). In addition, the SWAT model was calibrated and validated against measured river discharge at regional hydrometric stations and extended beyond the rooting zone, while the PACES report identified potential limitations in the HELP estimates, including underestimated evapotranspiration and locally artificial reductions in recharge caused by interpolated low-permeability sediment layers, so in comparison to the SWAT layer, the HELP

layer is higher predicting than the SWAT layer (Carrier et al., 2013). However, both methods produced broadly comparable spatial recharge patterns, and the selection of SWAT should therefore be interpreted as a modelling choice based on conceptual compatibility rather than proof that SWAT provides universally more accurate recharge estimates. Before implementation in MODFLOW, the SWAT recharge values were multiplied by the same depth-scaling factor applied to fractured-bedrock hydraulic conductivity (0.135335 per Equation 10) to maintain consistency with the effective hydraulic conditions represented at the conceptual depth of 50 m and to prevent unrealistically elevated simulated hydraulic heads (see Supplementary Material 5).

Groundwater discharge was represented using sink-type boundary conditions, including drain boundaries in low hydraulic head regions consistent with regional groundwater discharge zones: Résurgence préférentielle (Carrier et al., 2013). Preferential groundwater-discharge zones were defined by the PACES project as areas where exfiltration from the regional fractured-bedrock aquifer was considered significant at the regional scale (Carrier et al., 2013). The layer was delineated using aquifer-confinement conditions, the regional piezometric surface, shallow water-table areas, and spatially distributed HELP recharge estimates, with many identified discharge zones corresponding to rivers, wetlands, and groundwater discharge along the Appalachian front (Carrier et al., 2013). This dataset was therefore used to guide the spatial placement of DRN boundaries representing discharge directly from the fractured-bedrock layer. Drain conductance defines the ease with which groundwater can leave a model cell through a drain boundary and therefore controls the rate of simulated groundwater discharge once groundwater levels rise above the assigned drain elevation. A drain boundary in MODFLOW represents locations where groundwater can leave the model once simulated hydraulic heads arise above a specified drain elevation, allowing the model to simulate natural groundwater discharge processes such as seepage to rivers, streams, wetlands etc., in this model, the drain elevation is set as the top of the model so consistent with the defined top of the fractured bedrock topography (Carrier et al., 2013).

Drain conductance controls the rate at which groundwater is exchanged between the aquifer and the drain boundary; higher conductance values allow for more efficient drainage for a given hydraulic head difference (Harbaugh, 2005). In MODFLOW, drain conductance (C) has units of m^2/year and is defined as (Harbaugh, 2005; Equation 12):

$$C = \frac{KLW}{M} \tag{12}$$

where K is the hydraulic conductivity of the material in the boundary condition, in this case K_z (m/year), L and W are the length and width of the boundary within a cell, and M is the thickness of the material separating the boundary from the aquifer, typically representing the vertical thickness of the material (Harbaugh, 2005).

In ModelMuse, conductance values for the DRN package can be defined by the user or calculated internally depending on the selected "Conductance Interpretation". In this study, the default "Calculated" conductance option was selected. Under this formulation, width of the polygon is automatically incorporated by ModelMuse, and the drain conductance input (C) therefore is reduced as follows (Harbaugh, 2005; Equation 13):

$$C = \frac{K}{M} \tag{13}$$

with a unit of 1/T where T is time in years.

To account for the vertically connected nature of fracture-controlled discharge pathways in the fractured bedrock aquifer, vertical hydraulic conductivity (K_z) was used for DRN conductance (Harbaugh, 2005), K_z ranges from 7.89 m/year to 321.94 m/year (Carrier et al., 2013), calculated using Equation 11, therefore, in this study, drain conductance can be calculated as follows (Equation 14):

$$C = \frac{K_z \ of \ the \ hydrogeological \ zone}{100 \ m} \tag{14}$$

A spatially uniform effective porosity of 0.02 (2%) was assigned to all active model cells. Effective porosity represents the interconnected pore and fracture volume that participates in mobile groundwater flow and solute transport, rather than the total void space within the rock (See Supplementary Material 7). ModelMuse requires porosity as an input for MODPATH particle tracking, while the same value is used by MT3D-USGS to represent the mobile pore volume involved in advective and dispersive tracer transport (Pollock, 2016; Bedekar et al., 2016; U.S. Geological Survey, 2025). Under the steady-state flow conditions used in this study, effective porosity controls simulated groundwater velocity and particle travel time but does not change the spatial trajectory of MODPATH flowlines; decreasing porosity increases particle velocity and reduces calculated travel time (Pollock, 2016). The selected value of 0.02 was applied uniformly as an equivalent-porous-medium simplification and falls within the effective-porosity range of 0.015–0.05 previously used for Ordovician fractured-bedrock units in a comparable regional groundwater model in southern Québec (Gagné et al., 2018).

2.2.4.1 Recharge and Discharge Boundary Conditions:

Groundwater recharge and discharge were represented in the model using specified-flux and head-dependent boundary conditions, respectively. Regional groundwater recharge was applied to the upper fractured-bedrock layer through the MODFLOW Recharge (RCH) package as a spatially distributed, specified flux derived from the PACES SWAT recharge dataset (Carrier et al., 2013). These recharge values represent the estimated water transferred to the regional fractured-bedrock aquifer after accounting for shallow groundwater return flow to streams. The SWAT recharge values were subsequently adjusted during model calibration, as described above. For the age-tracer simulations, the PACES preferential-recharge raster was used to identify the principal locations through which ^{14}C, and ^{3}H entered the fractured-bedrock aquifer. These major recharge zones were intersected with the PACES aquifer-confinement map so that tracer recharge concentrations could be assigned to individual 250 × 250 m model cells according to whether the aquifer was unconfined, semi-confined, or confined. Thus, the spatially distributed RCH dataset controlled the hydraulic recharge flux, whereas the preferential-recharge and confinement datasets controlled the location and concentration of tracer inputs.

Groundwater discharge was represented using the MODFLOW Drain (DRN) package within preferential-discharge zones identified by PACES from regional piezometric, confinement, recharge, and surface-water information (Carrier et al., 2013). These zones primarily correspond to rivers, streams, wetlands, shallow-water-table areas, and discharge areas along the Appalachian front. The DRN boundaries acted as one-way, head-dependent sinks: groundwater could leave the fractured-bedrock aquifer when the simulated hydraulic head exceeded the assigned drain elevation, but water could not enter the aquifer through the drains when the simulated head was lower. Drain elevations were assigned at the model top, corresponding to the bedrock-surface elevation, while drain conductance controlled the rate of discharge. Together, the RCH and DRN packages represented the principal regional inflows to and outflows from the modelled fractured-bedrock aquifer, while local exchanges within the unconsolidated deposits and small-scale surface-water interactions were not explicitly resolved.

2.3 MODPATH 7 Particle Tracking Setup

MODPATH 7 was used together with MODFLOW-NWT to simulate regional groundwater flow pathways and track the advective movement of groundwater through the fractured bedrock aquifer system. MODPATH 7 is a particle-tracking model that uses the hydraulic head and cell-by-cell flow outputs generated by MODFLOW simulations to calculate groundwater particle trajectories through the model domain (Pollock, 2016).

The simulation type applied in this model was *Pathlines*, allowing the complete trajectory of groundwater particles to be tracked from recharge zones toward regional discharge areas (Pollock, 2016). Particle tracking direction was set to *Forward*, such that particles followed the physical direction of groundwater flow from areas of recharge to areas of discharge (Pollock, 2012, 2016). Recharge flux was assigned to the upper face of the recharge cells using the IRCHTP top-face recharge option, representing areal recharge entering the groundwater system across the water table and contributing to the vertical velocity component within the uppermost active cells (Pollock, 2012, 2016). Weak sink treatment was defined as *Pass Through*, allowing particles to continue through minor sink cells without terminating particle tracks, thereby preserving regional scale advective flow pathways (Pollock, 2012, 2016). Zone restrictions were disabled, so no user-defined zone-based termination condition was imposed on the particle tracks; particles nevertheless remained subject to the standard MODPATH termination conditions associated with model boundaries, capturing sinks, and the maximum tracking time (Pollock, 2012, 2016).

Initial particle locations were assigned at the central point of major recharge zones defined from Recharge préférentielle (Carrier et al., 2013; Figure 8) and imported into ModelMuse as recharge-area objects. Particles were released at the start of the simulation (time = 0) and tracked under steady-state groundwater flow conditions for a total simulation duration of 60,000 years. This extended simulation period allowed regional groundwater flow paths to fully develop within the model domain and ensured that long regional flow trajectories could be captured for interpretation of groundwater residence times and groundwater age-tracer transport.

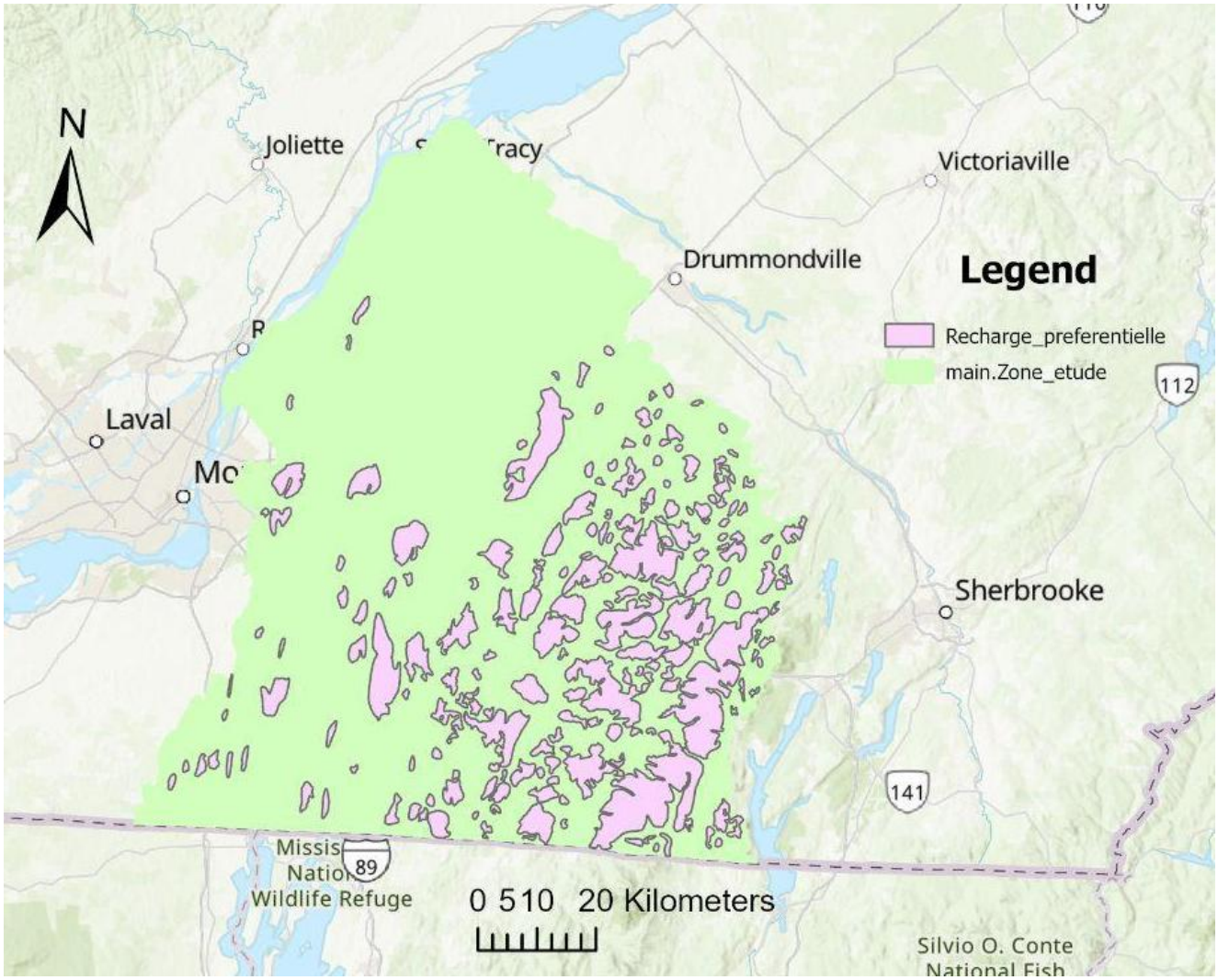


Figure 8. Preferential recharge zones to the regional fractured-bedrock aquifer in Montérégie Est (Carrier et al., 2013). Preferential recharge zones were identified as areas with estimated recharge greater than 250 mm/year and an associated regional piezometric high extending over more than 1 km². These zones occur mainly in the Appalachian Uplands and Piedmont and around the Monteregian Hills, with smaller areas in the southern St. Lawrence Lowlands. Spatial data were retrieved from Carrier et al. (2013) and redrawn in ArcGIS Pro.

2.4 MT3D-USGS setup

2.4.1 Advection and Dispersion Parameters

MT3D-USGS was used to simulate the transport, mixing, and radioactive decay of groundwater age tracers within the calibrated MODFLOW-NWT groundwater flow model. MT3D-USGS is an enhanced version of MT3DMS that supports additional MODFLOW flow packages and improved compatibility with MODFLOW-NWT, including handling of drying and rewetting cells (Bedekar et al., 2016). The transport simulations incorporated advection, mechanical dispersion, molecular diffusion, and first-order radioactive decay of ^{3}H and ^{14}C. A molecular diffusion coefficient of 0.00315576 m^2/year was assigned using the DMCOEF parameter. However, at the regional scale, tracer transport was expected to be controlled primarily by advection and mechanical dispersion, with molecular diffusion making only a minor contribution.

The Basic Transport (BTN), Advection (ADV), Dispersion (DSP), Sink and Source Mixing (SSM), Reaction (RCT), and Generalized Conjugate Gradient (GCG) packages were activated. Advection was simulated using the third-order Total Variation Diminishing (TVD) scheme (MIXELM = -1), which minimizes numerical dispersion while maintaining stable transport simulations. Mechanical dispersion was represented using a longitudinal dispersivity term (αL) together with the dimensionless horizontal and vertical transverse-to-longitudinal dispersivity ratios, TRPT and TRPV, which define tracer spreading parallel and perpendicular to the principal groundwater-flow direction respectively (Bedekar et al., 2016). Values of TRPT=0.1 and TRPV=0.03 were adopted in this study as model assumptions, representing lower transverse than longitudinal spreading and lower vertical than horizontal transverse mixing. For the selected longitudinal dispersivity of 376.09 m, these ratios correspond to horizontal and vertical transverse dispersivities of 37.61 m and 11.28 m, respectively. Cross-dispersion terms were enabled to allow multidirectional tracer spreading within the model domain.

Age tracers were introduced through the Sink and Source Mixing package using specified recharge concentrations. Chemical reactions were limited to first-order radioactive decay (IREACT = 1), which is appropriate for simulating the decay behaviour of ^{3}H and ^{14}C. Sorption, dual-domain mass transfer, and redox reactions were not simulated (ISOTHM = 0; IREACTION = 0), allowing the model to focus on advective-dispersive transport and radioactive decay processes. Dual-domain mass transfer was not included because site-specific

data required to constrain immobile-domain properties and mass-transfer coefficients were unavailable (Briggs et al., 2014).

Longitudinal dispersivity describes the spreading of dissolved tracers parallel to the main direction of groundwater flow (Freeze & Cherry, 1979). In groundwater systems, dissolved tracers such as tritium (^{3}H) and radiocarbon (^{14}C) do not move as a single uniform front because groundwater velocities vary between fractures, pore spaces, and flow pathways within the aquifer (Freeze & Cherry, 1979). As groundwater moves through the subsurface, some portions of the tracer plume travel faster while others move more slowly, causing the tracer to spread out along the direction of flow. This process is referred to as longitudinal dispersion and is represented in MT3D-USGS using the longitudinal dispersivity parameter (αL) (Bedekar et al., 2016). Longitudinal dispersivity therefore represents mechanical spreading caused by heterogeneity in groundwater velocities and flow pathways within the aquifer system (Gelhar et al., 1992).

Groundwater age transport in this study is represented using an advection–dispersion framework following the simulation approach described by Molson and Frind (2012; 2017), in which age is treated as a continuously increasing scalar transported by groundwater flow. Mean groundwater age is defined as the average age of a packet of water molecules at a given point in space (Molson and Frind, 2017; Bethke and Johnson, 2008). The governing equation for mean groundwater age is expressed as (Goode, 1996; Equation 15):

$$\frac{\partial}{\partial xi}\left(D_{i,j}\frac{\partial C}{\partial xj}\right) - vi\frac{\partial C}{\partial xi} + q_s C_s \qquad (15)$$

where C is the simulated solute concentration, D_{ij} is the hydrodynamic-dispersion tensor (m^2/year), x_i and x_j are the spatial coordinates in the three Cartesian directions v_i is the groundwater seepage-velocity component (m/year), qs is the volumetric flow rate per unit aquifer volume associated with a groundwater source or sink, and C_s is the solute concentration of the source or sink water (Xu and Eckstein, 1995). This formulation is mathematically equivalent to the steady-state advection–dispersion equation with a unit production term and forms the basis for simulating advective–dispersive groundwater ages. In this study, the equation is numerically solved using MT3D-USGS, computing advective transport from MODFLOW-determined seepage velocities and represents dispersion through a velocity-dependent tensor defined by longitudinal and transverse dispersivities along a local flowline (Xu and Eckstein, 1995). Model construction and transport parameters were assigned with ModelMuse, which does not alter the governing transport formula as it serves as a graphical

interface. Therefore, defining the parameter “Longitudinal dispersivity" in Modelmuse is a key control on dispersive mixing and transport behaviour in the model, which will ultimately influence the outcomes of the ^{14}C and ^{3}H MT3D-USGS models.

For numerical modelling, macrodispersion is often used. Molson and Frind describe macrodispersion as a means of representing uncertainty and mixing arising from local-scale heterogeneities that cannot be resolved by the numerical grid (Molson and Frind, 2012). This approach accounts for advective-dispersive transport which accounts for this uncertainty which isn’t factored into pure particle tracking (Molson and Frind, 2012). It is emphasized that macrodispersion is appropriate for field to watershed scale modelling, with the caution that overly large dispersivities in numerical models can lead to excessive numerical smearing and loss of physically meaningful age gradients (Molson and Frind, 2012). Therefore, it is important to select scale-consistent dispersions that are appropriate for the model scale, such that artificial numerical dispersion is limited while also allowing realistic mixing of groundwater through dispersion during transport (Molson and Frind, 2012). In this study, longitudinal dispersivity (αL) was defined based on the empirical dispersivity macro-scaling relationship developed by Neuman (1990) for where L ≥ 100 m (Neuman, 1990; Janos et al., 2018; Equation 16):

$$\alpha_L = 0.32L^{0.83} \tag{16}$$

where *L* represents a characteristic transport length scale (Neuman, 1990) and 0.83 is a dimensionless empirical scaling exponent derived from regression of field-scale dispersivity data.

The approximate flow path length was determined to maximize around 5 km in local flow systems in neighbouring regions with similar local flow systems (Janos et al., 2018): $\alpha_L = 0.32 * (5000\ m)^{0.83} = 376.09$ m. Accordingly, the longitudinal dispersivity here was set at 376.09 m for ModelMuse.

The primary limitation of Neuman’s (1990) macro-scaling relationship is that it assumes a power law increase of longitudinal dispersivity with field scale, whereas field data in future studies indicate that the rate of increase becomes very small at kilometre scales (Janos et al., 2018; Xu and Eckstein, 1995). Xu and Eckstein (1995) show that fitting separate linear trends for different scale ranges can lead to loss of data and discontinuities, while a single regression as described by Neuman (1990) may overestimate dispersivity at large scales (Janos

et al., 2018; Xu and Eckstein, 1995). Therefore, it should only be used as an effective field - scale dispersivity (Janos et al., 2018; Xu and Eckstein, 1995). Despite these limitations, Neuman's (1990)'s relationship provides a physically based estimate of effective longitudinal dispersivity that is appropriate for regional-scale transport models with grid resolutions on the order of hundreds of metres, where sub-grid heterogeneity cannot be resolved. For a grid size of 250 m, this relationship yields dispersivity values that are consistent with MT3D-USGS ^{14}C and ^{3}H outputs (see Supplementary Material 7), therefore can be used as a field-scale macrodispersion, with uncertainties addressed through further sensitivity analyses (see Results section).

2.4.2 Péclet Number Analysis and Numerical Stability Assessment

In regional-scale models with coarse spatial discretization, transport is commonly advection-dominated (Neumann et al., 2011; Alecsa et al., 2020). The Péclet number (P_e) is used as a diagnostic measure to evaluate the relative importance of advection and dispersion and numerical transport stability threshold (Hossain and Yonge, 1999; 14). P_e is often defined based on the first variation of the Péclet number (DHI,2025; Hossain and Yonge, 1999; Equation 17):

$$Pe = \frac{V_e L}{D_L} = \frac{V_D L}{n_e D_L} \quad (17)$$

where V_e is the effective groundwater velocity (m/year), L is a reference length representing transport distance (m), defined here as the distance from major recharge zones, which are considered the primary source of groundwater ^{14}C input in this study, D_L is the longitudinal hydrodynamic dispersion coefficient (m^2/year), V_D is Darcy velocity (m/year) and n_e is the effective porosity for advection (Fetter 1999; Sauty 1980) (Hossain and Yonge, 1999). D_L here includes both molecular diffusion (mass transport)/ thermal conduction (heat transport) and mechanical dispersion (m^2/year) (DHI, 2025; Equation 18):

$$D_L = \alpha_L v_e + D_m + D_h, \quad (18)$$

where α_L is again the longitudinal dispersivity, v_e is the effective groundwater velocity (L/T), and D_m is the effective molecular diffusion coefficient (m^2/year) (Hossain and Yonge, 1999). D_m was defined as 0.00315576 m^2/year based on a study on a neighbouring hydrogeologic region (Laurencelle, 2018). D_h was not included in this study since it represents thermal conduction contributions to hydrodynamic dispersion, while this study focuses on groundwater solute transport rather than coupled heat transport processes. Molecular diffusion is negligible in comparison to mechanical flow (α_L multiplied by v_e) in a fractured bedrock system, therefore Equation 17 can be simplified into Equation 19 and Equation 20:

$$P_e \simeq \frac{v_e L}{\alpha L v_e} = \frac{L}{\alpha L} \quad (19)$$

$$\therefore P_e \simeq \frac{L}{\alpha L} = \frac{5000\,m}{376.09\,m} = 13.29 \quad (20)$$

When Pe is low ($\ll 1$), groundwater transport simulation in the numerical model is diffusion/dispersion dominated; when Pe is high ($\gg 1$), groundwater flow is advection dominated in the numerical model (Hossain and Yonge, 1999). Here, Pe is 13.29, indicating advection flow dominated transport regime, consistent with the fractured bedrock aquifer

system in Montérégie Est (Beaudry et. al, 2018). Because the calculated (Pe) value is dependent on the selected characteristic length, a separate cell Péclet-number analysis was conducted using the model-grid spacing to evaluate the adequacy of the spatial discretization for numerical solute transport; the calculation and results are presented in the Supplementary Material 8.

2.5 Data Screening and Selection Criteria

2.5.1 Historic hydrochronologic data used to calibrate model

The 2010–2011 PACES Montérégie Est campaign collected groundwater samples from 206 locations across the study region. The data generated during this campaign are hereafter referred to as the 2010 field campaign. Following quality-control review, 190 samples were incorporated by Beaudry et al. (2018), building upon the regional PACES characterization of Carrier et al. (2013), to define eight hydrochemical water groups distributed across five hydrogeological contexts (see Introduction).

This 2010 field campaign dataset contained 43 samples used for groundwater age interpretation. From these, five samples were classified as “Other” because they were not assigned to one of the hydrochemical water groups defined by Beaudry et al. (2018) and were therefore excluded from the present model evaluation. This left 38 water-group-assigned samples as the initial candidate dataset for construction and evaluation of the MT3D-USGS transport model (Figure 9).

For generating the model for this project, an additional precautionary screening step was applied to the initial candidate dataset to remove wells located within 500 m of a mapped river or lake, thereby reducing potential localized effects of groundwater–surface-water interaction. This distance corresponds to two model cells at the model resolution of 250 m and therefore represents a conservative exclusion buffer defined relative to the spatial discretization of the model. Groundwater chemistry and environmental-tracer concentrations may be particularly sensitive to surface-derived recharge and mixing in shallow or hydraulically connected areas (Meyzonnat et al., 2016). Excluding wells near surface-water features therefore helped ensure that the calibration and evaluation dataset was more representative of regional groundwater flow and geochemical evolution rather than localized surface-water influence.

Application of this 500 m buffer excluded 11 additional samples (red circles in Figure 10). Together with the five samples classified as “Other,” 16 samples in total with age tracer data were excluded from the 2010 field data set, leaving 27 wells for model evaluation. These retained wells were distributed among the hydrochemical water groups defined by Beaudry et al. (2018) as follows: three wells in A1, six in A2, four in A3, four in M1, four in M2, one in M3, two in LL, and three in CS. Specific well identifiers, water-group assignments, and spatial coordinates are provided in Table 2.

These wells represent groundwater conditions ranging from actively recharged shallow

systems associated with relatively local flow to chemically evolved groundwater associated with longer residence times and regional circulation (Beaudry et al., 2018). The retained samples were obtained from boreholes completed in the fractured-bedrock aquifer, with casing installed through the surficial sediments and open-hole intervals within the underlying bedrock. Consequently, each groundwater sample may represent an integrated contribution from multiple water-producing fractures intersected by the open borehole rather than groundwater from a single discrete depth (Beaudry et al., 2018).

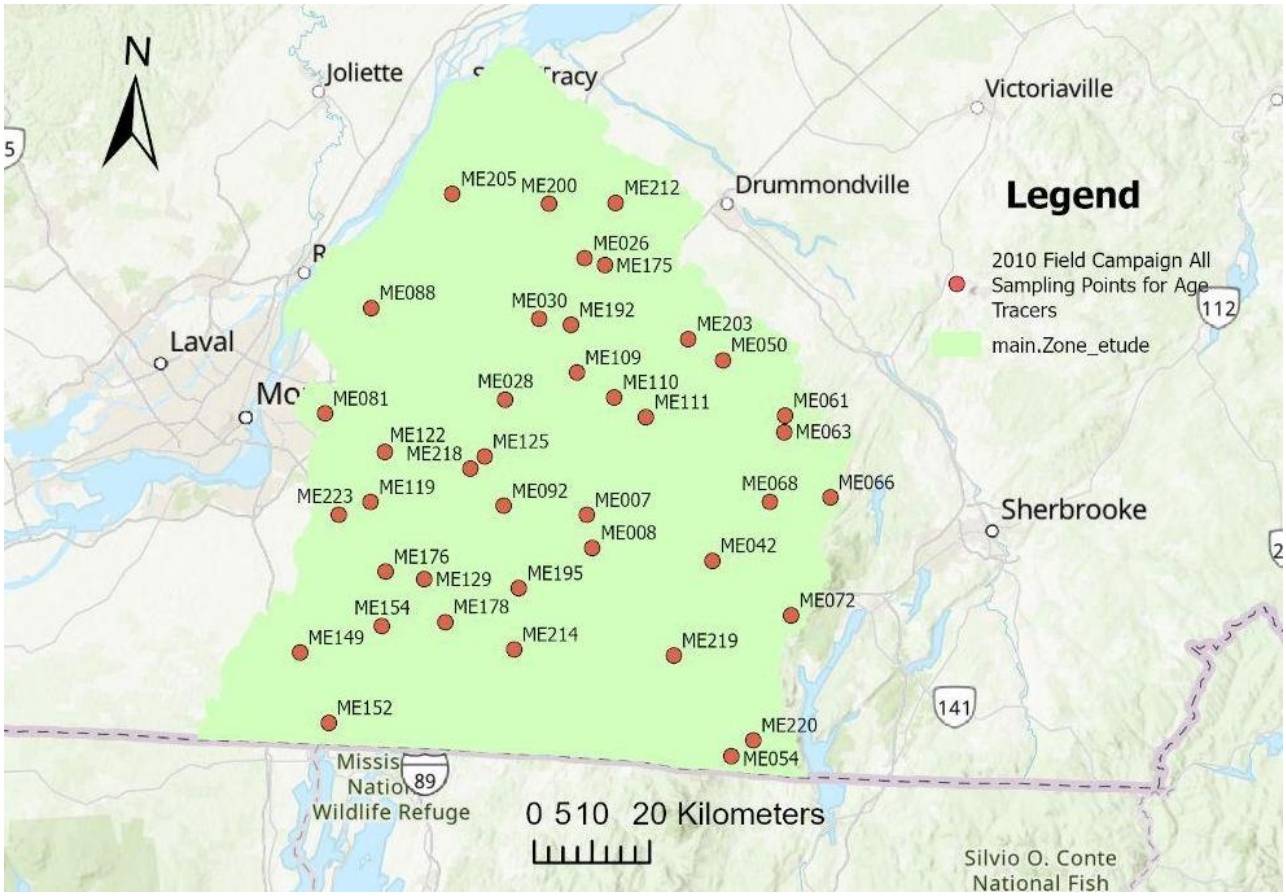


Figure 9. Spatial distribution of the 2010 PACES age-tracer sampling locations in the Montérégie Est study area (adapted from Beaudry et al., 2018). Red circles indicate groundwater sampling locations included in the 2010 age-tracer dataset, with labels corresponding to their ME site identifiers. The green polygon delineates the Montérégie Est study area. Sites RS02_ROC and P11 (DUP20) are not shown because corresponding ME identifiers and spatial coordinates were unavailable in the compiled database (Beaudry et al., 2018).

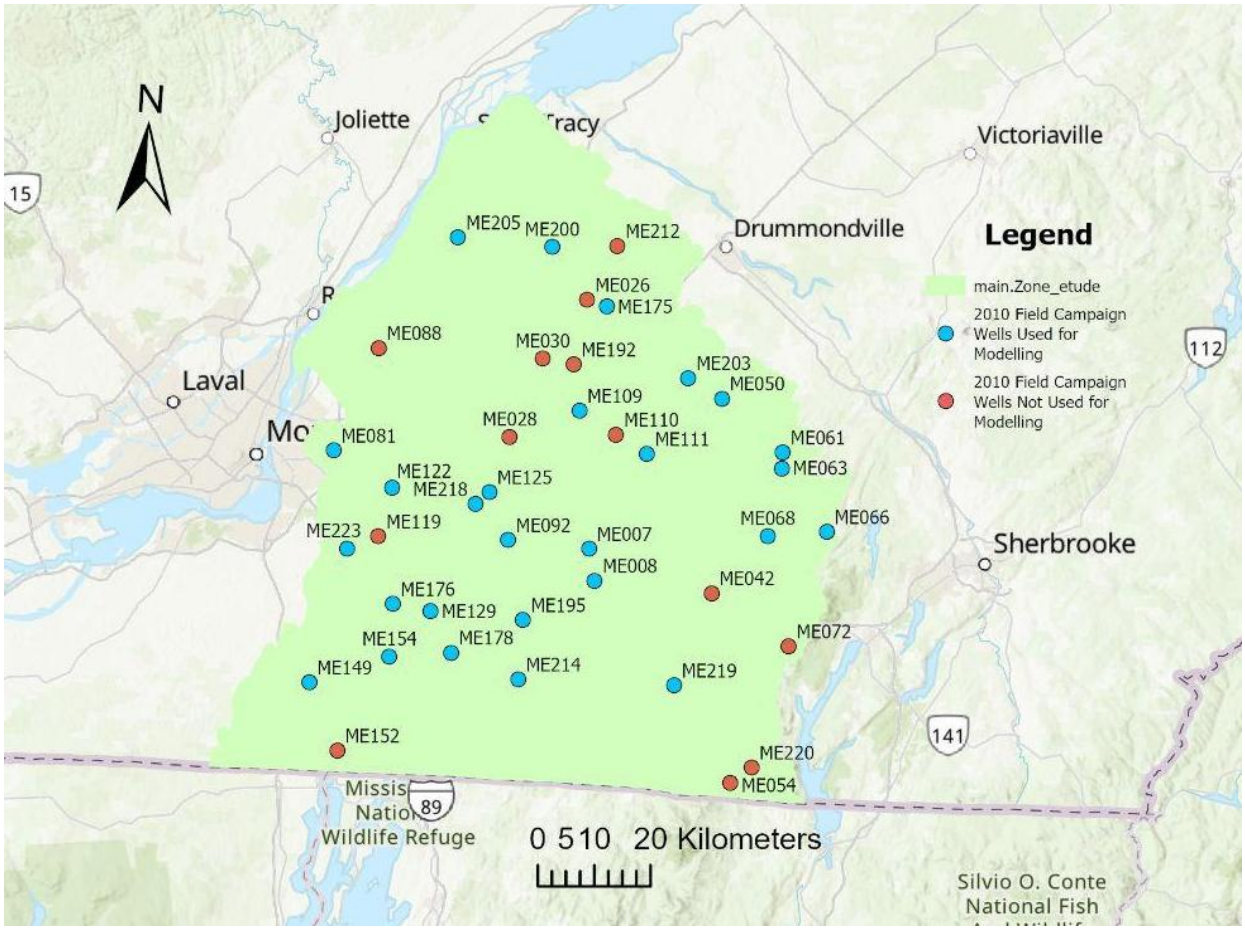


Figure 10. Spatial distribution of 2010 PACES groundwater age-tracer sampling locations in the Montérégie Est study area. The green polygon outlines the modelled study area. Blue points indicate 2010 groundwater sampling locations retained for model calibration and evaluation, while red points indicate 2010 sampling locations excluded from modelling because of missing hydrochemical group assignment or proximity to mapped surface-water features. Sample IDs are labelled beside each point, and the basemap is shown for regional geographic context.

Table 2. 2010 Groundwater wells used to evaluate and calibrate simulated model predictions against measured groundwater conditions in the Montérégie Est region.

Sample ID	PACES INRS ID	Water Group	X_QL	Y_QL
ME007	INRS108	A1	-335938.75	165255.65
ME050	INRS151	A1	-312382.03	192106.48
ME066	INRS167	A1	-293770.45	168282.27

ME068	INRS169	A2	-304207.11	167536.63
ME195	INRS300	A2	-347663.13	152598.68
ME203	P06	A2	-318318.44	195761.3
ME214	P16	A2	-348544.22	141999.7
ME218	P19	A2	-356076.31	173305.99
ME219	P20	A2	-320892.39	140939.27
ME008	INRS109	A3	-334966.94	159596.64
ME061	INRS162	A3	-301570.39	182509.61
ME063	INRS164	A3	-301773.15	179650.08
ME111	INRS213	A3	-325665.07	182226.04
ME109	INRS211	M1	-337667.42	189884.39
ME122	INRS224	M1	-370847.93	176134.97
ME125	INRS227	M1	-353629.22	175436.46
ME178	INRS280	M1	-360479.41	146774.78
ME092	INRS193	M2	-350311.14	166857.02

ME154	INRS256	M2	-371366.57	146053.7
ME175	INRS277	M2	-332832.69	208508.58
ME176	INRS278	M2	-370828.41	155433.41
ME223	P23	M3	-378834.91	165325.32
ME129	INRS231	LL	-364118.99	154147.78
ME149	INRS251	LL	-385601.64	141453.52
ME081	INRS182	CS	-381300.6	182836.52
ME200	P03	CS	-342489.58	219121.23
ME205	P08	CS	-359203.13	220842.48

Note: These wells were used to compare model predictions with measured 2010 groundwater data. Wells assigned to the CS hydrochemical group are included in the table for completeness but are excluded from most subsequent model-evaluation figures and discussions because this group exhibits the strongest influence from brackish groundwater processes, which are not reproduced accurately by the present model (see Supplementary Material 9 and Discussion).

2.5.2 Model Evaluation and Calibration Using Historical Data

The regional hydraulic-head distribution shown in Figure 11 was generated by the steady-state MODFLOW-NWT simulation using the PACES-derived model inputs described above, rather than being interpolated directly from the 2010 field measurements. The water budget reported by the MODFLOW water budget output in the .lst file is displayed below in Table 3. As shown in Table 3, the total inflow of the model is 73,543,248 m^3/yr with a storage inflow of 0 m^3/yr; while the outflow of the model is 73,532,160 m^3/yr with a total storage outflow of 0 m^3/yr. The reported percentage discrepancy is therefore approximately 0.00012%, therefore reported by MODFLOW as 0.00%. These confirms that this model performs as a steady state model, and the internal water budget of this steady state model has a consistent internal water-budget, while physical representativeness of this model is additionally evaluated using hydraulic heads, regional recharge information and tracer observations. The simulated surface reproduces the broad regional pattern of higher hydraulic heads in recharge areas and decreasing heads toward regional discharge zones (Figure 11). The PACES piezometric surface was used to initialize the model, while model performance was evaluated by comparing the final simulated heads with hydraulic-head observations from the modelled 2010 field campaign wells.

Table 3. Water budget output reported by MODFLOW-NWT.

Water-budget component	Inflow (m^3/yr)	Outflow (m^3/yr)
Recharge	73,532,248	0
Drains	0	73,532,160
Storage	0	0
Constant-head flow	0	0
Total	**73,532,248**	**73,532,160**

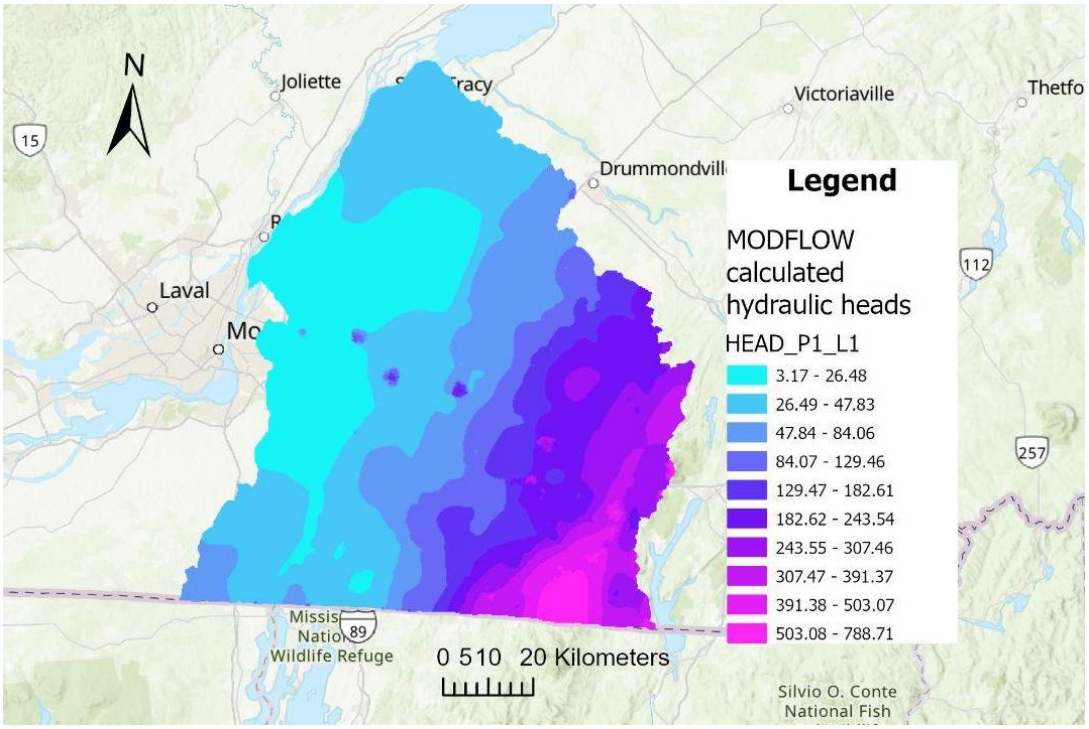


Figure 11. Simulated hydraulic head distribution in the Montérégie Est regional groundwater flow model. Spatial distribution of simulated hydraulic heads generated using the steady-state MODFLOW-NWT groundwater flow model for the Montérégie Est fractured bedrock aquifer system (represented by HEAD_P1_L1 in the MODFLOW-NWT model output, indicating the MODFLOW-NWT calculated hydraulic head in layer 1: the fractured bedrock layer). Per the legend, warmer colors (pink) represent regions of higher hydraulic head associated with regional recharge zones, while cooler colors (i.e. blue) indicate lower hydraulic head regions corresponding to regional groundwater discharge areas.

Although the model reproduced the principal regional hydraulic gradient and the general distribution of hydraulic highs and lows, the maximum simulated hydraulic head of 788.71 m was 151.95 m, or approximately 16.2%, lower than the maximum value of 940.66 m represented by the PACES piezometric surface (Figures 7 and 11). This reasonably good agreement (within 20%) is considered acceptable within the regional modelling framework because the PACES surface is an interpolated regional representation developed at approximately 1:100,000 scale and may not reproduce local conditions precisely (Carrier et al., 2013). Some of the highest values on the PACES piezometric surface also occur within spatially restricted areas. Although both the piezometric raster and the MODFLOW grid have a nominal resolution of 250 × 250 m, differences in interpolation and cell-based averaging may smooth or omit localized piezometric peaks when the source data are transferred to the numerical model. A spatial pattern of hydraulic-head overestimation was observed in the Northern St. Lawrence Lowlands (Figure 11). This area is extensively confined by low-permeability Champlain Sea sediments and was conceptualized as a regional discharge zone

with relatively slow or locally stagnant groundwater conditions. In the model, discharge was represented only within the principal PACES preferential-discharge zones using regional-scale DRN boundaries. As a result, smaller or spatially distributed discharge pathways, including local groundwater seepage and exchanges with surface-water or unconsolidated sediment systems, may not have been fully represented. The limited removal of groundwater from this confined area may therefore have caused simulated heads to remain higher than the measured values (Figure 11). This interpretation is also consistent with the ^{14}C results for the Champlain Sea (CS) water group, for which the model generally underestimated measured ^{14}C activities. These low simulated ^{14}C activities suggest groundwater residence times are significantly overestimated here, supporting the interpretation that groundwater flow and flushing were simulated as too slow in the Northern St. Lawrence Lowlands. The two-layer conceptualization and use of representative regional hydraulic properties further average local topographic and fracture-controlled variations that may produce sharper hydraulic-head highs in the physical aquifer than would be simulated in the modelling approach outlined here. Differences may also arise from uncertainty and non-uniqueness in recharge, hydraulic conductivity, anisotropy, and discharge-boundary conductance, all of which influence simulated hydraulic heads (Reilly & Harbaugh, 2004; Hill & Tiedeman, 2007). The empirical scaling factor of 0.135335 applied to hydraulic conductivity, recharge, and DRN conductance may also have contributed to the lower maximum simulated head; however, because these parameters were scaled simultaneously, their individual effects cannot be isolated without additional sensitivity testing (see Supplementary Material 5).

Model performance was evaluated by comparing simulated steady-state hydraulic heads with measured hydraulic heads from the 2010 PACES wells (Figure 12). The simulated heads showed strong agreement with the observations, with a regression slope close to unity ($y = 1.029x - 3.341$), a high coefficient of determination ($R2 = 0.981$), and a root mean square error of 12.57 m. Most observations plot close to the 1:1 line, indicating that the model reproduced both the magnitude and regional variation of hydraulic head with little overall systematic bias, despite a small number of larger residuals. This level of agreement was considered sufficient to support the use of the simulated groundwater-flow field for subsequent MODPATH 7 particle-tracking and MT3D-USGS age-tracer simulations.

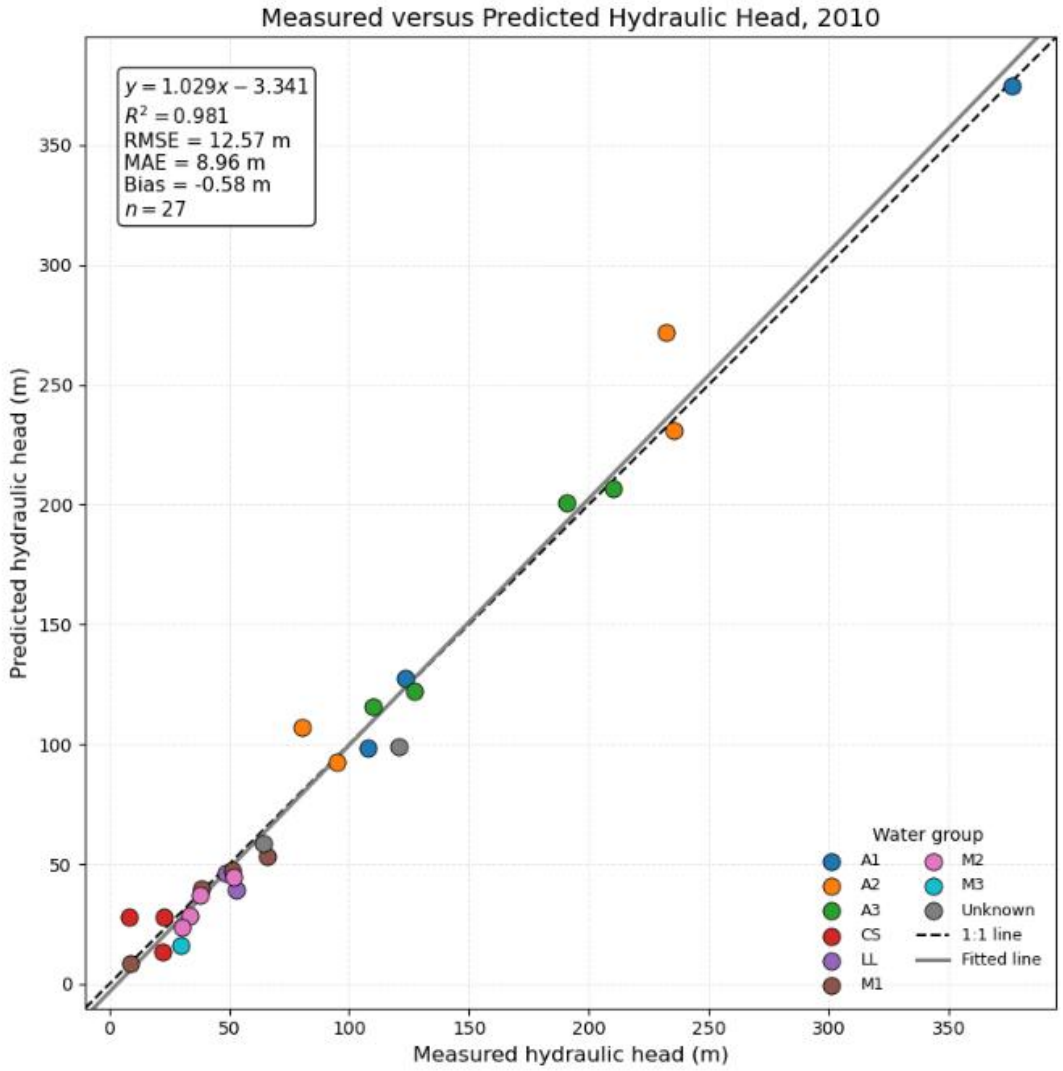


Figure 12. Comparison of measured and simulated hydraulic heads for the 2010 PACES model-evaluation wells. Simulated steady-state hydraulic heads are plotted against measured 2010 hydraulic heads. The solid green line represents the 1:1 relationship, while the dashed red line represents the fitted linear regression (y = 1.029x − 3.341). Model performance was characterized by $R^2 = 0.981$ and an RMSE of 12.57 m (data in Supplementary Material 1 Table 17).

Following evaluation of the hydraulic-head simulation, the final steady-state MODFLOW-NWT solution was used to define the groundwater-flow field for particle tracking. The hydraulic gradients and cell-by-cell groundwater flows calculated by MODFLOW-NWT were transferred to MODPATH 7 to generate dominant regional groundwater pathlines through the fractured-bedrock aquifer system. These pathlines, shown in Figure 13, illustrate the simulated connections between regional recharge and discharge areas and provided the advective-flow framework subsequently used for the MT3D-USGS age-tracer transport simulations.

2.5.3 Delineation of Major Advection Groundwater Flowpaths

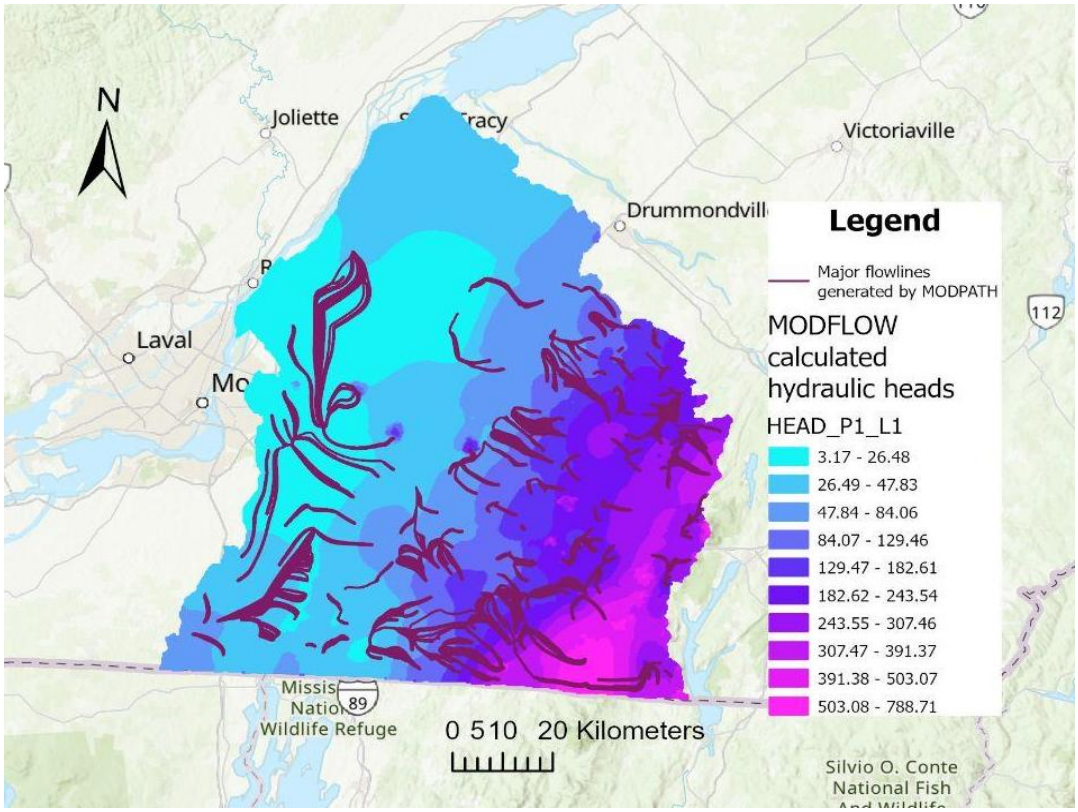


Figure 13. Simulated regional groundwater flow regimes and flow system dynamics. Simulated regional groundwater flow regimes and advective flow system dynamics generated using MODFLOW-NWT and MODPATH 7 for the Montérégie Est fractured bedrock aquifer system. Background colors represent simulated hydraulic head distributions (per Figure 11), while purple pathlines indicate simulated groundwater flow trajectories originating from regional recharge zones and moving toward lower hydraulic head discharge regions. The simulated flow systems illustrate dominant regional groundwater flow directions and spatial variations in groundwater transport pathways across the study area generated by the model.

The simulated hydraulic-head distribution and MODPATH 7 pathlines shown in Figure 13 are broadly consistent with the conceptual groundwater-flow model proposed by Beaudry et al. (2018). Higher hydraulic heads in the eastern Appalachian Uplands and Piedmont generate predominantly westward and northwestward groundwater flow toward the lower-elevation St. Lawrence Lowlands, while shorter, more localized flow paths occur around individual topographic highs and nearby discharge areas. The longer pathlines extending from the Appalachian region toward the Lowlands and the Monteregian Hills support the conceptual interpretation of regional groundwater circulation from upland recharge areas toward mixing and discharge zones located west of the Appalachian Front and around the Monteregian Hills. Overall, the numerical results provide quantitative support for the principal regional flow directions inferred independently from the hydrogeochemical and isotopic evidence.

2.5.4 ^{3}H Transport Model

^{3}H transport was simulated using MT3D-USGS to evaluate groundwater residence times and compare predicted tritium distributions against measured groundwater tritium concentrations within the Montérégie Est fractured bedrock aquifer system. Unlike ^{14}C, ^{3}H is incorporated directly into the water molecule and therefore behaves conservatively during groundwater transport, with minimal influence from carbonate dissolution, cation exchange, or other water-rock interaction processes that commonly affect dissolved inorganic carbon and radiocarbon activities (Clark & Fritz, 1997; Cook & Herczeg, 2000). Therefore, ^{3}H transport was assumed to be controlled primarily by groundwater mixing and radioactive decay processes.

Recharge-zone ^{3}H concentrations were assigned using the Source-Sink Mixing (SSM) package in MT3D-USGS. Recharge objects were assigned using the "Specified Concentration" option (ITYPE = −1), which allows a defined concentration to be introduced as a transport boundary condition while groundwater flow rates remain controlled by the MODFLOW flow solution (Zheng & Wang, 1999; Bedekar et al., 2016; Figure 8; Figure 11), ensuring ^{3}H mass is added to the transport simulation without modifying the groundwater flow field, recharge rates, or hydraulic heads calculated by MODFLOW-NWT. A similar approach was used for the ^{14}C transport model.

An initial recharge concentration of 14 TU was assigned to the PACES-defined major recharge zones where the fractured bedrock aquifer is unconfined and directly connected to modern meteoric recharge. This value was selected based on groundwater samples located within approximately 250 m of PACES defined main recharge zones (Figure 8), which exhibited average measured tritium concentrations of approximately 14 TU during the 2010 field campaign. Because the objective of the initial model calibration was comparison against the 2010 tritium dataset, 14 TU was considered representative of modern recharge entering the fractured bedrock aquifer during the PACES sampling period. Although ^{3}H was treated as a conservative groundwater tracer, the 14 TU concentration was not assigned to every area receiving recharge in the MODFLOW flow model. Instead, it was applied only to the PACES defined major recharge zones where the fractured bedrock aquifer is unconfined and modern meteoric water can enter the aquifer relatively directly. In confined portions of the study area, low-permeability surficial sediments restrict and delay recharge to the bedrock, and any downward leakage is expected to contain a much more attenuated and mixed tritium signal. Applying the same modern recharge concentration to these confined areas would therefore

serve to overcontribute tritium to the model from these second order and minor recharge zones and would result in unrealistically young simulated groundwater. The restricted concentration boundary condition was consequently intended to represent the principal locations of direct modern recharge to the fractured bedrock aquifer, rather than all cells assigned a groundwater-recharge flux in the MODFLOW model.

Radioactive decay was simulated using the MT3D-USGS Reaction (RCT) package assuming first-order decay kinetics. A decay constant of 0.05624 yr^{-1} was assigned based on the accepted tritium half-life of 12.32 years (Lucas & Unterweger, 2000). Tritium transport was then simulated through advection, hydrodynamic dispersion, and radioactive decay under steady-state groundwater flow conditions derived from the calibrated MODFLOW-NWT flow model. The transport simulation was run for 150 years, allowing tritium signals introduced at recharge zones to migrate throughout the model domain and develop spatial concentration gradients consistent with regional groundwater flow patterns.

The ability of the model to reproduce the regional distribution of tritium was evaluated by comparing the measured 2010 (^3H) concentrations with those predicted from the model across the hydrochemical water groups (Figure 14). Overall, the model reasonably reproduced the broad regional pattern, with low measured tritium concentrations generally corresponding to low predicted concentrations and higher measured values corresponding to higher predicted values. The ordinary least-squares regression produced an (R^2) value of 0.796, indicating that approximately 80% of the variability in predicted tritium concentrations was associated with variability in the measured concentrations. The regression equation, ($y = 0.989x + 0.653$), had a slope close to unity, although the positive intercept indicates a slight tendency to overpredict at low measured concentrations.

Several predictions cluster at approximately 14 TU because recharge zones in the upper fractured-bedrock layer were assigned a fixed tritium concentration of 14 TU (See Supplementary Material 11). Predicted values extracted directly from cells located within, or immediately adjacent to, these recharge zones therefore partly reflect the imposed recharge concentrations rather than a fully simulated transport history. Therefore, the agreement of the highest-concentration points are primarily due to the model setup and may provide limited independent evidence of model performance. Deviations below this imposed upper boundary likely reflect groundwater mixing, dispersion, variation in recharge history, and local hydrogeological conditions that are not fully represented by the regional steady-state model. No clear systematic separation among the hydrochemical water groups is evident. Overall, the

model captures the first-order regional distribution of tritium, but its predictive performance is weaker than suggested by the upper-end points alone and remains sensitive to the prescribed recharge concentration.

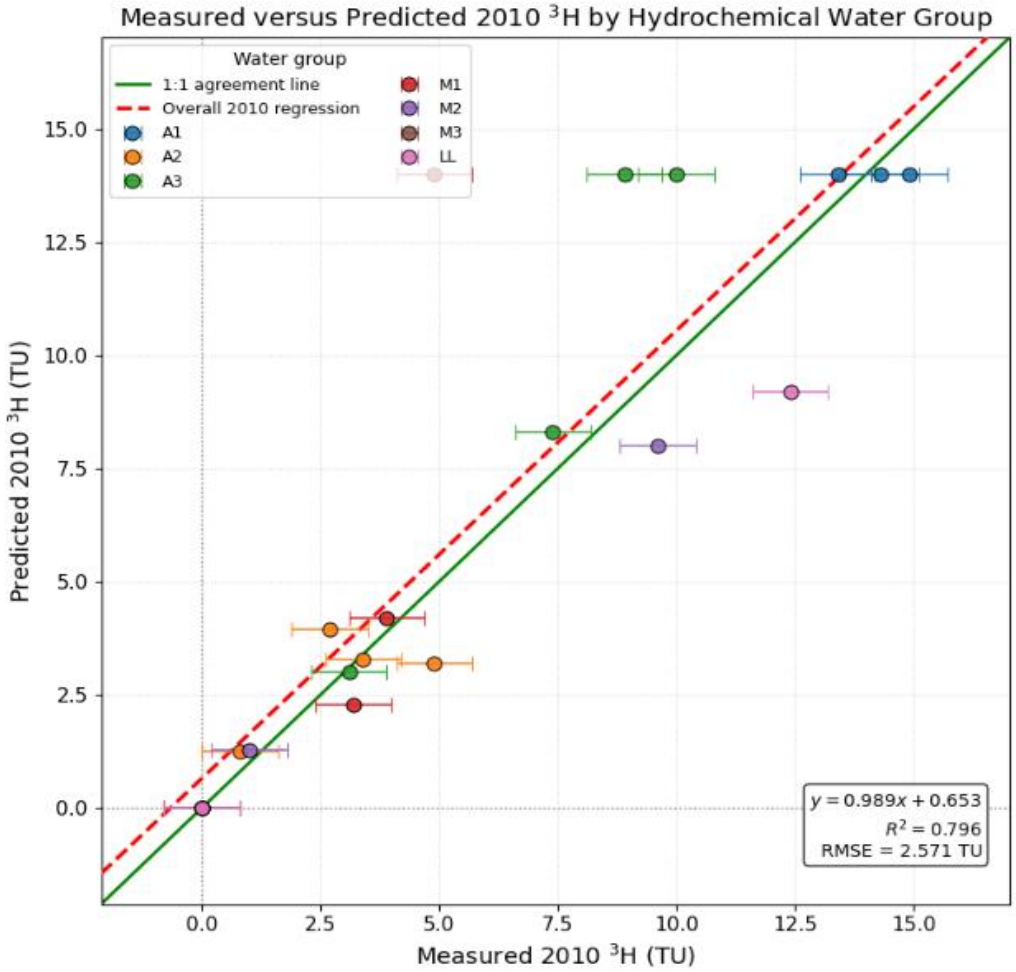


Figure 14. Measured versus Predicted 2010 Tritium Concentrations by Hydrochemical Water Groups. Comparison of measured and model predicted 2010 ^{3}H concentrations for 22 groundwater samples used for modelling from the 2010 dataset, classified by hydrochemical water group. Measured ^{3}H concentrations are plotted on the x-axis and predicted ^{3}H concentrations on the y-axis, with horizontal error bars representing the uniform analytical uncertainty of ±0.8 TU for the measured values. Water groups are distinguished by color: A1 = blue, A2 = orange, A3 = green, M1 = red, M2 = purple, M3 = brown, and LL = pink. Measured or predicted values below the 0.55 TU detection threshold were assigned a value of 0 TU for plotting and statistical analysis. Following this treatment, five samples—ME214, ME122, ME176, ME223, and ME149—share the same coordinate at (0,0) and therefore overlap visually as a single point, although all five observations were retained in the regression, R^2, and RMSE calculations. The solid green line represents perfect 1:1 agreement, and the dashed red line represents the ordinary least-squares regression between measured and predicted concentrations. (The CS group including ME 175 are excluded, ME 175 and ME 195 were not included due to suspected river influence). (Data used for this figure is in Supplementary Material 11 Table 24)

2.5.5 ^{14}C Transport Model

Similar to the ^{3}H model, radiocarbon transport was simulated using MT3D-USGS by treating ^{14}C as a dissolved tracer subject to first-order radioactive decay. Groundwater flow velocities were obtained from the calibrated MODFLOW-NWT flow model, while transport was simulated through advection, hydrodynamic dispersion, and radioactive decay. A first-order decay constant of 0.00012097 yr^{-1} was assigned based on the accepted radiocarbon half-life of 5,730 years (Clark & Fritz, 1997). Recharge-zone concentrations were assigned through the MT3D-USGS Source-Sink Mixing (SSM) package and transported throughout the model domain according to the groundwater flow field generated by MODFLOW-NWT. Similar to the ^{3}H model, the transport simulation was equilibrated, this time using a longer runtime of 60,000 years, allowing radiocarbon signals introduced at recharge zones to migrate throughout the model domain and develop spatial concentration gradients consistent with regional groundwater flow patterns.

An initial transport simulation was performed assuming that all recharge entering the fractured bedrock aquifer at the major recharge zones possessed a uniform radiocarbon activity of 100 pMC, representing modern recharge conditions. Under this assumption, recharge concentrations were assigned uniformly to all major recharge zones identified through MODPATH particle tracking and regional hydrogeological interpretation. Following simulation of advective transport and radioactive decay, predicted radiocarbon activities were compared against measured groundwater ^{14}C activities from the PACES dataset. However, this initial simulation systematically overestimated ^{14}C activities in several semi-confined and confined hydrogeological contexts relative to measured data, particularly in groundwater samples located close to major recharge zones but exhibiting substantially lower measured radiocarbon activities (See Supplementary Material 10). This led to the second iteration of the model.

For the second iteration of the model, the ^{14}C activity at the point of recharge was decreased in line with observations from the 2010 data set. Specifically, several groundwater samples located close to PACES-defined major fractured recharge zones were found to have measured radiocarbon activities of approximately 35 pMC. This suggested that the assumption of uniform modern recharge at 100 pMC may have likely overestimated the initial radiocarbon signal entering the fractured bedrock aquifer. Therefore, a second transport model was developed in which all major recharge zones were assigned a reduced initial radiocarbon activity of 35 pMC. This model was designed to test whether a lower effective recharge

concentration, based on measured radiocarbon activities near recharge areas, could explain the systematic overestimation observed in the initial 100 pMC simulation. Although the 35 pMC model improved agreement in some areas, it also produced underestimation in other regions, indicating that simply applying a single reduced recharge concentration across all recharge zones was too restrictive and did not adequately represent spatial variability in recharge-zone geochemical conditions (See Supplementary Material 10).

To address this, a third and final transport model was then developed using assigned zone-specific recharge-zone radiocarbon activities to reflect local soil-water-rock interactions and confinement conditions according to the hydrochemical water groups associated with each recharge area as follows.

First, within the PACES-defined major fractured-bedrock recharge areas, recharge zones associated with water groups M2 and CS were all assigned an initial radiocarbon activity of 100 pMC. Secondly, cells associated with hydrochemical groups A1, M3, and LL were treated according to confinement conditions. Unconfined recharge cells were assigned a radiocarbon activity of 100 pMC, whereas no specified radiocarbon recharge concentration was applied to semi-confined or confined cells. In these confined cells, simulated ^{14}C activity was therefore determined by transport from surrounding areas, mixing, and radioactive decay (as opposed to any input via direct recharge).

Finally, for hydrochemical groups A2, A3 and M1, recharge cells associated with unconfined conditions again retained an activity of 100 pMC while recharge cells associated with semi-confined and confined conditions were this time assigned an initial radiocarbon activity of 35 pMC. Sensitivity analyses indicated that this intermediate value provided the best reproduction of measured groundwater ^{14}C activities. Beaudry et al. (2018) identified Na–Ca ion exchange, evolved rates of carbonate dissolution and groundwater freshening as dominant processes affecting these water groups, providing supporting hydrochemical evidence that recharge waters in these areas may undergo partial geochemical modification prior to entering the fractured bedrock aquifer. To account for the distinct ^{14}C signature associated with the A3 water group, an additional recharge concentration of 58 pMC was assigned to recharge cells associated with the Monteregian Hills. This adjustment reflects the enhanced groundwater circulation and mixing potentially promoted by the Monteregian dyke and fracture network described by Beaudry et al. (2018). The value of 58 pMC was selected because groundwater samples located within these recharge areas exhibited raw ^{14}C activities of approximately 58 pMC. Similarly, M1 recharge zones were slightly increased to 38 pMC to account for the

recharge signals there.

Following incorporation of these refinements to reflect local recharge conditions, the final iteration of the model showed very strong agreement between simulated and measured raw ^{14}C activities. The results are presented graphically in Figure 15, while the corresponding measured and model-predicted values for each well are provided in Supplementary Material 11 Table 24. The regression slope (1.013) and high coefficient of determination ($R^2 = 0.993$) indicate that the final model successfully reproduced the regional distribution of raw ^{14}C activities across the 2010 calibration dataset. The exception to this was the CS group which is extensively influenced by the brackish water group in the Northern St.Lawrence Lowland (Beaudry et al., 2018) and is not plotted in Figure 15.

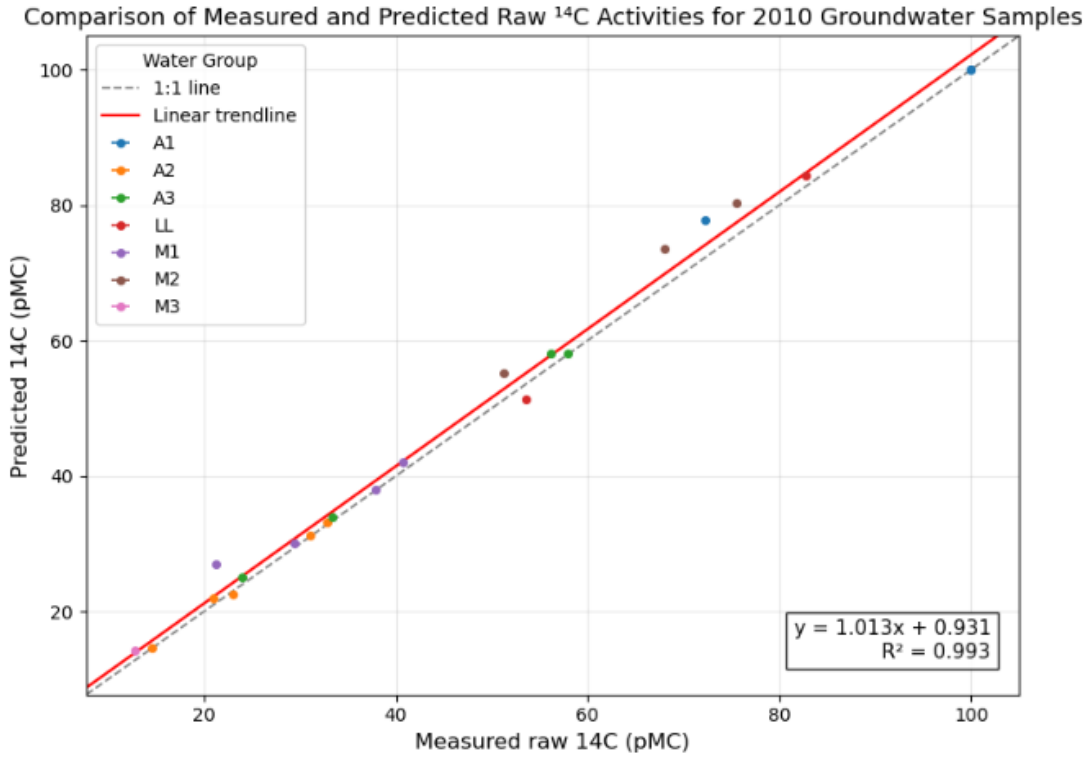


Figure 15. Comparison of raw measured and model-predicted (^{14}C) values for the 2010 calibration dataset. Measured raw (^{14}C) values are plotted against model-predicted (^{14}C) values for groundwater samples collected during the 2010 field campaign and used for regional model calibration before the 2025 field campaign. Points are coloured according to the hydrogeochemical water groups defined by Beaudry et al. (2018): A1 = blue, A2 = orange, A3 = green, M1 = purple, M2 = brown, M3 = pink, and LL = red. The dashed line represents the linear regression between measured and predicted values, while the solid redline represents the 1:1 agreement relationship. The strong agreement between measured and simulated (^{14}C) values ($R^2 = 0.993$) indicates that the calibrated model reproduces the first-order regional groundwater (^{14}C) distribution. Samples belonging to the CS group were excluded due to

extended brackish water group influence (Including ME 175). ME 175 and ME195 were also excluded because of suspected localized river influence. Data used to construct this figure are provided in Supplementary Material 11, Table 25.

The calibrated model successfully reproduced the regional groundwater-flow field and the 2010 age-tracer distribution for all evaluated hydrochemical groups except CS (Figure 15). This project then was able to independently assess its predictive capability by sampling new wells during a targeted field campaign in 2025 for age-tracer and supporting hydrochemical analyses.

Chapter 3. Targeted field data to evaluate model

3.1 Field Sampling and Well Sites Selection

3.1.1 New geochemical data used to validate calibrated model

Data collected during the 2010 field campaign were used to develop an initial hydrochemical and numerical groundwater model, as outlined in Section 3.3. This model provided a conceptual and quantitative framework for identifying dominant flow pathways and groundwater evolution across the study area. Building on this framework, and to evaluate its reliability over time, a targeted field campaign was conducted in 2025 (hereafter referred to as the 2025 field campaign). This campaign was specially designed to evaluate the modelled groundwater dynamics and major advection flow pathways by sampling new data points along identified flowlines as well as resampling wells from Beaudry et al., 2018 to compare legacy data from the 2010 field campaign with resampled data, providing a 15-year interval to identify any potential major temporal trends. Additionally, three river samples (R1-R3) were collected as well as Well ME175 and Well ME 195 from the 2010 dataset which were 256 and 104 metres from a river respectively to evaluate the extent to which localized surface water-groundwater interactions may influence tracers at the local (individual site) level.

This field campaign included two separate field trips, for the first field trip in August 2025, during which ^{3}H and major ion samples were collected; and a second field trip in September 2025, where ^{14}C and DIC samples were collected. This 2025 campaign focused on sampling borehole wells located along major groundwater flow paths within the Montérégie Est region. To evaluate the dominant outcomes of the initial model, sample locations were selected based on proximity (500 m) of MODPATH identified flow pathways and one conceptual major flow pathway going from MODFLOW calculated hydraulic high to hydraulic low. These additional samples and their relation to the 2010 field campaign are given in Figure 16 and Table 4.

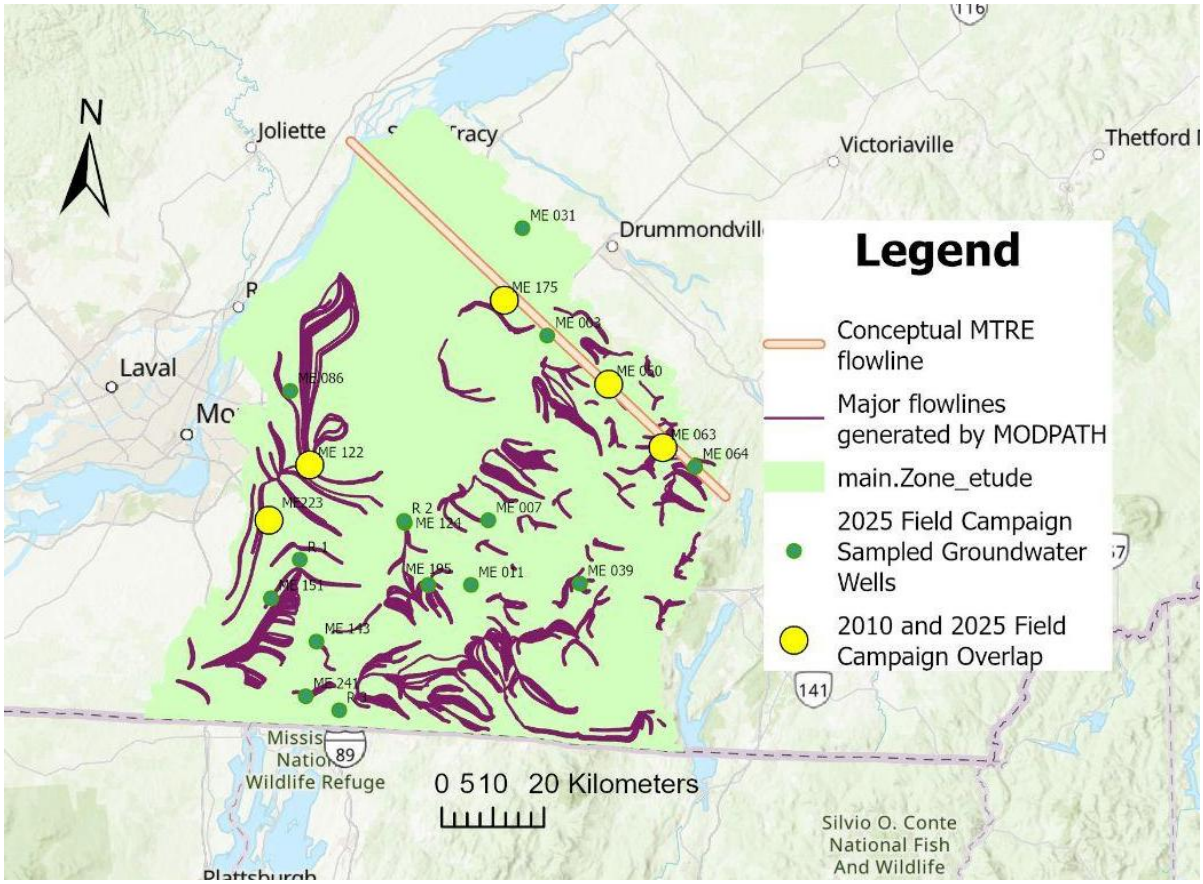


Figure 16. Model-guided selection of groundwater sampling locations for the 2025 field campaign. The pale-green polygon delineates the Montérégie Est regional model domain. Purple lines show major groundwater flowpaths generated using MODPATH 7, while the orange line represents the conceptual Montérégie Est regional groundwater-flow path going from predicted hydraulic high to predicted hydraulic low. Green circles indicate wells sampled only during the 2025 field campaign, and yellow circles indicate wells sampled during both the 2010 and 2025 field campaigns. Selected well identifiers are labelled beside the sampling locations. The distribution of the 2025 sampling sites was designed to intersect contrasting modelled flow pathways and hydrogeological settings across the study area.

Table 4. Summary of groundwater tracer and hydrochemical analyses of the 2010 field campaign (Beaudry et al.,2018) and additional data collected by the 2025 field campaign as part of this study, the coordinate system is in Quebec Lambert.

Site ID (2025)	PACES ID	X_QL	Y_QL	2010 and 2025 Field Campaign Analyses Overlap	Additional 2025 Field Campaign Analyses
ME 241	X23	−371682.88	130698.06	Major ions	^{14}C, ^{3}H, $\delta^{18}O$, $\delta^{2}H$

ME 143	INRS 245	−369544.21	141513.67	Major ions	^{14}C, ^{3}H, $\delta^{18}O$, $\delta^{2}H$
ME 122	INRS 224	−370847.93	176134.97	^{14}C, ^{3}H, $\delta^{18}O$, $\delta^{2}H$, major ions	—
ME 063	INRS 164	−301773.15	179650.08	^{14}C, ^{3}H, $\delta^{18}O$, $\delta^{2}H$, major ions	—
ME 175	INRS 277	−332832.69	208508.58	^{14}C, ^{3}H, $\delta^{18}O$, $\delta^{2}H$, major ions	—
ME 050	INRS 151	−312382.03	192106.48	^{14}C, ^{3}H, major ions	$\delta^{18}O$, $\delta^{2}H$
ME 003	INRS 103	−324335.33	201574.34	Major ions	^{14}C, ^{3}H, $\delta^{18}O$, $\delta^{2}H$
ME 064	INRS 165	−295457.30	175846.64	Major ions	^{14}C, ^{3}H, $\delta^{18}O$, $\delta^{2}H$
ME 195	INRS 300	−347663.13	152598.68	^{14}C, ^{3}H, $\delta^{18}O$, $\delta^{2}H$, major ions	—
ME 007	INRS 108	−335938.75	165255.65	^{14}C, ^{3}H, major ions	$\delta^{18}O$, $\delta^{2}H$
ME 011	INRS 112	−339385.29	152609.57	$\delta^{18}O$, $\delta^{2}H$, major ions	^{14}C, ^{3}H
ME 031	INRS 132	−329264.44	222680.73	Major ions	^{14}C, ^{3}H, $\delta^{18}O$, $\delta^{2}H$
ME 039	INRS 140	−317970.96	152891.89	Major ions	^{14}C, ^{3}H, $\delta^{18}O$, $\delta^{2}H$
ME 124	INRS 226	−352339.96	164762.56	Major ions	^{3}H

ME 086	INRS 187	−374753.94	190700.04	Major ions	^{3}H
ME 151	INRS 253	−378568.43	150031.88	Major ions	^{3}H
R 1	New river site — Richelieu River	−357316.91	239512.52	New site	^{14}C, ^{3}H, $\delta^{18}O$, $\delta^{2}H$, major ions
R 2	New river site — Yamaska River	−342695.52	246041.38	New site	^{14}C, ^{3}H, $\delta^{18}O$, $\delta^{2}H$, major ions
R 3	New river site — Missisquoi Bay	−365188.99	127950.67	New site	^{14}C, ^{3}H, $\delta^{18}O$, $\delta^{2}H$, major ions

Groundwater and surface-water samples were collected from 19 field sites during the 2025 campaign, comprising 16 active groundwater wells and three surface-water sites representing the Richelieu River, Yamaska River, and Missisquoi Bay. The analytical suite completed at each well varied according to private-well owner consent, site accessibility, and sample availability. Thirteen wells were analyzed for major ions, ^{14}C, ^{3}H, $\delta^{18}O$, and $\delta^{2}H$, whereas ME124, ME086, and ME151 were analyzed for major ions and ^{3}H only. Among the 13 wells sampled for the complete analytical suite, 11 were classified as fractured-bedrock wells (R) and two as granular wells (G) in the PACES database (Beaudry et al., 2018). This classification reflects the mapped hydrogeological or surficial context rather than necessarily identifying the water-producing interval (Carrier et al., 2013). In practice, the wells are cased through the surficial sediments and extend into the underlying fractured bedrock; Therefore, the sampled groundwater was interpreted as representative of the fractured-bedrock aquifer system (Beaudry et al., 2018; Carrier et al., 2013).

The sampled wells were distributed across the Appalachian Uplands, Piedmont, and the northern and southern St. Lawrence Lowlands. Five wells—ME050, ME063, ME122, ME175, and ME195—were re-sampled for the complete analytical suite to evaluate consistency and identify potential temporal changes where corresponding measurements from the 2010 campaign were available. Additional wells were selected within 500 m of major advective

groundwater-flow pathways identified using MODPATH (Figure 16). All sampled wells were in active residential use, and the complete inventory of groundwater and surface-water sites and their respective analyses is presented in Table 4. Although ME031 is included in the complete sampling inventory, it has been excluded from subsequent figures and quantitative model comparisons because it is suspected to be influenced by nearby river water and is therefore evaluated separately in the Discussion section - 5.4 River Influence.

3.1.2 Well Access Permissions and Landowner Consent

All groundwater sampling conducted during the 2025 field campaign was performed at privately owned borehole wells. Access to each sampling location was obtained only after permission and informed consent were granted by the respective property owners prior to fieldwork.

3.2 Field Sampling Procedures and Analytical methods

3.2.1 Field Sampling Procedures

Prior to sampling, all wells were flushed for five minutes to remove stagnant water and ensure representative samples were collected. Temperature, pH, electrical conductivity (EC) and total dissolved solids (TDS) were measured in the field using Hanna HI98194 (Hanna Instruments Canada, HI98194).

Stable Isotopes ($\delta^{18}O$ and $\delta^{2}H$)

The water stable isotope samples were collected using 60 mL HPDE bottles pre-rinsed three times with sample water (Thermo Scientific, 2104-0002) and were filled with no headspace (Los Gatos Research, 2025).

Major Ion Field Sampling Procedures

The cation and anion collection bottles were collected using 60 mL HPDE bottles pre-rinsed three times with sample water (Thermo Scientific, 2104-0002). Cation samples were acidified immediately after collection to pH < 2 with 1-2 mL of 1% HNO_3 to preserve dissolved metals by preventing precipitation and adsorption before analysis (U.S. EPA, 2015). Samples were transported in ice packages filled coolers then refrigerated 4 °C until analysis.

^{3}H Field Sampling Procedures

The groundwater ^{3}H samples were sampled following the protocol of the Tritium Laboratory at the André E. Lalonde AMS Laboratory. Specifically, the groundwater samples for ^{3}H were collected in FisherScientific™ 1L HDPE bottles (Wheaton, W082130) pre-rinsed with sample water for three times with minimal headspace before capping. No treatments were done to the ^{3}H samples until analysis.

DIC and ^{14}C Field Sampling Procedures

The water samples for ^{14}C and DIC were sampled according to established protocols (Murseli et al., 2019). Samples were either collected in 40 mL pre-cleaned borosilicate amber EPA ThermoFisherScientific™ vials with PTFE-lined silicone septa caps (Thermo Fisher Scientific, 0333914E), with the PTFE side against the water (Chromatographic Specialties Inc., C8850522C). ^{14}C samples with expected low DIC concentrations (< 25 mg C/L) based on existing data were collected in requiring larger volumes to ensure the minimum 1 mg of total

carbon for analysis was sampled. These were collected in 1 L WheatonTM glass bottles that had been acid-soaked in HCl for one hour, thoroughly rinsed with Milli-Q water, and baked at 500 °C for three hours prior to use (Wheaton, W219419; Murseli et al., 2019), with caps and septa cleaned following the same protocols but without baking, lightly covered with aluminum foil to air dry (ME 063 and ME 050) (Wheaton, 33-430). All samples were filtered with 0.45 um nylon filters which had been pre-rinsed three times with sample water (Thermo Fisher Scientific, CH4525-NN) and were collected with minimal head space to prevent carbon isotope fractionation and were capped immediately after filling (Murseli et al., 2019). Samples were stored in coolers with ice packs in the field, then refrigerated at 4 °C in the fridge until analysis.

3.2.2 Post-Field Laboratory Analytical Procedures

Stable Isotopes ($\delta^{18}O$ and $\delta^{2}H$)

Stable isotopes of water ($\delta^{18}O$ and $\delta^{2}H$) were analyzed at the Ján Veizer Stable Isotope Laboratory, University of Ottawa, using a Los Gatos Research (LGR) Triple Isotope Water Analyzer in liquid-injection mode for fresh waters (<3 PSU) (ABB Measurement & Analytics, 2017). For analysis, 1.0 mL of 0.45 µm pre-filtered field sample was pipetted into a 2 mL glass GC vial. Each measurement used a 0.9 µL injection of sample water, up to 20 injections were averaged to improve precision (ABB Measurement & Analytics, 2017). Isotopic results were normalized to VSMOW using three calibrated internal standards within natural ranges, and a fourth calibrated standard was analyzed as an unknown concentration sample for long-term quality control. Routine analytical precision was ±0.2‰ for $\delta^{18}O$ and ±2.0‰ for $\delta^{2}H$.

Major Ion Analysis

Anions and cations were analyzed at the Geochemistry Laboratory, University of Ottawa. Anions (Cl^-, SO_4^{2-}, HCO_3^-) were analyzed by ion chromatography (IC) using a Dionex ion chromatograph (Cickaric et al., 2005). Ion chromatography separates dissolved ions based on their different affinities to ion-exchange resin (Cickaric et al., 2005). Major cations (Ca^{2+}, Mg^{2+}, Na^+, $Fe^{2+/3+}$, Sr^{2+}) were analyzed by using inductively coupled plasma emission spectroscopy (ICP-ES) on an Agilent 5110 Synchronous Dual View ICP emission spectroscopy (ICP-ES) (Agilent Technologies, 2016). Samples were introduced into an argon plasma where different ions were excited to emit light at different characteristic wavelengths (Thompson & Walsh, 1989). The emitted radiation wavelength was measured by a detector, elemental concentrations were determined based on the intensity of the emitted signal, which is proportional to analyte concentrations (Thompson & Walsh, 1989).

Dissolved Inorganic Carbon (DIC)

DIC concentrations were measured prior to the analysis of ^{14}C to ensure 1 mg minimum total dissolved carbon in each sample. DIC analysis took place at the Ján Veizer Stable Isotope Laboratory, University of Ottawa. DIC concentrations were measured using a modified OI Analytical Model 1030 wet TOC analyser equipped with a Model 1088 autosampler (OI Analytical, 2005). An aliquot of sample water was withdrawn via an automated needle into the reaction chamber, where it was acidified with 5% H_3PO_4 to convert all dissolved inorganic carbon into CO_2 (OI Analytical, 2005). The produced CO_2 was then purged from the reaction chamber using ultra-pure helium carrier gas, passing through water traps to remove moisture (OI Analytical, 2005). The CO_2 concentration in the headspace was then measured using a non-

dispersive infrared detector (OI Analytical, 2005). Calibration was carried out using two internal standards, potassium hydrogen phthalate (KHP) and sucrose, to generate a calibration curve for determining carbon concentrations (OI Analytical, 2005).). Results are reported in parts per million carbon (ppmC) (OI Analytical, 2005). The analytical precision of the DIC measurements is ±0.2 ppmC (OI Analytical, 2005).

Tritium (^{3}H)

^{3}H analyses were performed at the André E. Lalonde Accelerator Mass Spectrometry Laboratory (AEL-AMS), University of Ottawa following the laboratory's standard electrolytic-enrichment and low-level liquid-scintillation-counting protocol. ^{3}H measurements were conducted using the Tritium – Enriched by Electrolysis – Low Precision (LE) method. Due to the low ^{3}H activity typically observed in bedrock groundwater samples that travelled extended from a recharge point, water samples were electrolytically enriched to increase the relative abundance of ^{3}H, prior to analysis in order to improve detection limits per standard protocols. Following enrichment, samples were mixed with 10 mL of Ultima Gold scintillation cocktail and decay was counted using a low-background Quantulus liquid scintillation counter. The detection limit for the LE method at AEL-AMS is approximately 0.7-0.9 TU and is reported individually per sample. Tritium concentrations are reported in tritium units (TU), where 1 TU corresponds to one tritium atom per 10^{18} hydrogen atoms in water (Clark & Fritz, 1997).

Radiocarbon (^{14}C-DIC)

^{14}C-DIC samples were analyzed at the André E. Lalonde Accelerator Mass Spectrometry Laboratory (AEL-AMS), University of Ottawa. For ^{14}C analysis, pre-filtered water samples were transferred into pre-evacuated borosilicate bottles containing H_3PO_4 to acidify the samples and convert dissolved inorganic carbon species into CO_2 (Murseli et al., 2019). The samples were then heated at 60°C for an hour to convert all dissolved DIC into CO_2 (Murseli et al., 2019). After cooling to room temperature, CO_2 was extracted using a low flow helium carrier system with a vacuum extraction line in the end (Murseli et al., 2019). Purified CO_2 was cryogenically trapped, quantified, graphitized by hydrogen reduction, and measured on a IonPlus MICADAS 0.2 MV AMS (Murseli et al., 2019). The AEL-AMS laboratory reports a typical analytical precision of approximately 3–10‰ for this sample category, depending on sample type and analytical conditions. Radiocarbon results are reported as fraction modern carbon ($F^{14}C$), calculated as the ratio of the sample $^{14}C/^{12}C$ to that of the Oxalic Acid II (Ox-II) standard (Reimer et al., 2004).

Chapter 4. Results and model comparisons

4.1 Stable Isotopes

The stable isotope compositions of groundwater samples collected during the 2025 field campaign plot closely along the BLMWL (Cloutier et al., 2006), indicating that groundwater within the study area predominantly derived from meteoric recharge (Figure 17). Additionally, these groundwater samples collected during the 2025 field campaign show $\delta^{18}O$ values from −11.72‰ to −9.83‰ and $\delta^{2}H$ values from −79.49‰ to −65.14‰ (Table 5; Figure 16).

The close clustering of groundwater samples along the BLMWL suggests that there was limited evaporation prior to recharge (Rey et al., 2018; Figure 16). In comparison to groundwater samples, river water samples (R1–R3) are isotopically enriched relative to groundwater and plot further from the groundwater cluster, reflecting the greater influence of surface-water processes such as evaporation, seasonal variability, and direct atmospheric exchange. Although located further to the BLMWL in comparison to the groundwater samples, the river samples generally remain near the BLMWL and do not exhibit strong evaporative trends.

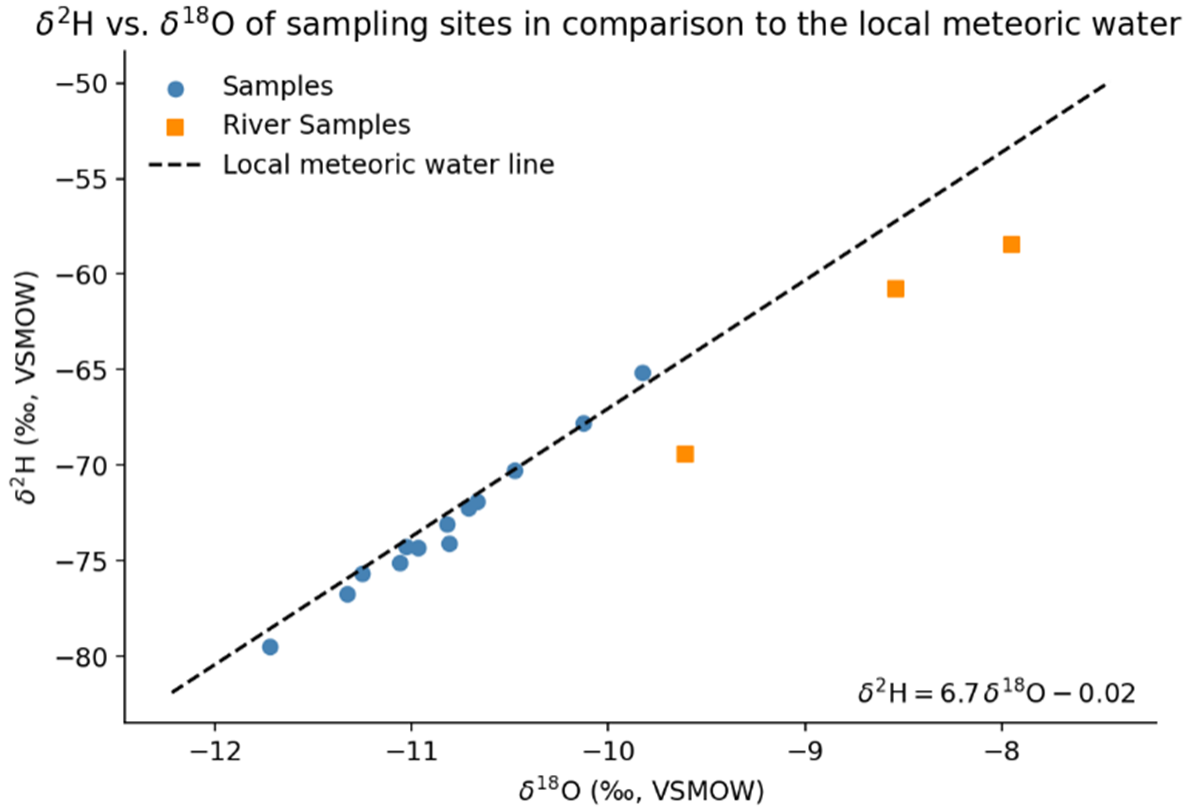


Figure 17. δ²H versus δ¹⁸O values of groundwater samples (blue circles) and river water samples (orange squares) collected during the 2025 field campaign in the Montérégie Est study area, Québec. The dashed black line represents the Basses-Laurentides Meteoric Water Line (BLMWL; Cloutier et al., 2006), expressed as $\delta^2H = 6.7\delta^{18}O - 0.02$. Isotopic compositions are reported relative to Vienna Standard Mean Ocean Water (VSMOW).

Table 5. Stable isotope compositions (δ²H and δ¹⁸O) of groundwater and surface water samples collected during the 2025 field campaign in the Montérégie Est study area, Québec, measured at the Ján Veizer Stable Isotope Laboratory, University of Ottawa. Deuterium excess (d-excess) values were calculated as $d = \delta^2H - 8\delta^{18}O$ and are reported in per mil (‰) relative to Vienna Standard Mean Ocean Water (VSMOW).

Sample ID	δ²H (‰ VSMOW)	δ¹⁸O (‰ VSMOW)	d-excess (‰)
ME 241	-71.89	-10.67	13.47
ME 143	-65.14	-9.83	13.5
ME 122	-75.08	-11.06	13.4

ME 063	-79.49	-11.72	14.27
ME 175	-70.25	-10.48	13.59
ME 050	-74.29	-10.97	13.47
ME 003	-67.76	-10.13	13.28
ME 064	-75.66	-11.25	14.34
ME 195	-73.08	-10.82	13.48
ME 007	-74.06	-10.81	12.42
ME 011	-72.25	-10.71	13.43
ME 039	-76.74	-11.33	13.9
R1	-58.46	-7.95	4.14
R2	-69.4	-9.61	7.48
R3	-60.77	-8.54	7.55

The d-excess can be used to evaluate the extent of evaporation prior to infiltration (Dansgaard, 1964), therefore providing additional information on the climatic and hydrological conditions that affect groundwater recharge conditions. Groundwater samples collected during the 2025 field campaign show relatively consistent d-excess values ranging from 12.42‰ to 14.34‰ (Table 5). This narrow range of d-excess values further supports that groundwater recharge occurred under broadly similar atmospheric and climatic conditions across the study area. Specifically, the relatively consistent and low d-excess values observed among groundwater samples indicate that evaporation prior to recharge was limited. If significant evaporation had occurred before infiltration, lower d-excess values would be expected due to preferential enrichment of heavy isotopes in the remaining water (Dansgaard, 1964). This

observation provides additional evidence that the sampled wells receive recharge from a common regional meteoric source.

River water samples all show lower d-excess values than groundwater. Sample R1 shows d-excess value of approximately 4‰, while R2 and R3 have values in the range of 7–8‰ (Table 5). These lower values are consistent with greater exposure to surface-water processes, particularly evaporation, which can reduce d-excess through kinetic fractionation (Dansgaard, 1964). The isotopic distinction between groundwater and river water samples suggests that groundwater recharge within the study area is not strongly influenced by evaporated surface waters and further supports the interpretation that most sampled groundwater represents direct meteoric recharge.

Overall, the d-excess data are consistent and indicate that groundwater recharge throughout the study area occurred under relatively similar climatic conditions with limited evaporative modification prior to infiltration. D-excess values also provide additional confidence that the observed variability in groundwater age tracers and hydrochemical parameters is primarily related to groundwater flow, mixing, residence time, and water-rock interaction processes occurring after recharge.

As part of this project focus, five wells from the 2010 were additionally resampled for stable isotopes to evaluate whether any temporal evolution had occurred. The data for these wells from both 2010 and 2025 field campaigns are compared in Table 6 and Figure 18. All values of the resampled data fall within 2 σ the reported uncertainty for the data (1 σ= ± 0.2‰ for $\delta^{18}O$ and ± 2.0‰ for $\delta^{2}H$) indicating no significant isotopic shift has occurred.

Table 6. Comparison of Stable Isotope Compositions ($\delta^{18}O$ and $\delta^{2}H$) Between the 2010 INRS Field Campaign and the 2025 Groundwater Sampling Campaign for Revisited Wells. Most values of the resampled data fall within 2 σ the reported uncertainty for the 2010 data (1 σ= ± 0.2‰ for $\delta^{18}O$ and ± 2.0‰ for $\delta^{2}H$ for year 2010 analysis).

ME ID	INRS ID (2010)	$\delta^{18}O$ (2010) ‰	$\delta^{2}H$ (2010) ‰	$\delta^{18}O$ (2025) ‰	$\delta^{2}H$ (2025) ‰	$\Delta\delta^{18}O$ (2025–2010) ‰	$\Delta\delta^{2}H$ (2025–2010) ‰
ME063	INRS 164	-12.5	-83.1	-11.7	-79.5	0.783	3.61

ME122	INRS 224	-12	-74	-11.2	-75.1	0.943	-1.08
ME195	INRS 300	-11	-74	-10.8	-73.1	0.185	0.92
ME011	INRS 112	-11	-72	-10.7	-72.3	0.286	-0.25
ME175	INRS 277	-10.95	-71.3	-10.5	-70.3	0.474	1.05

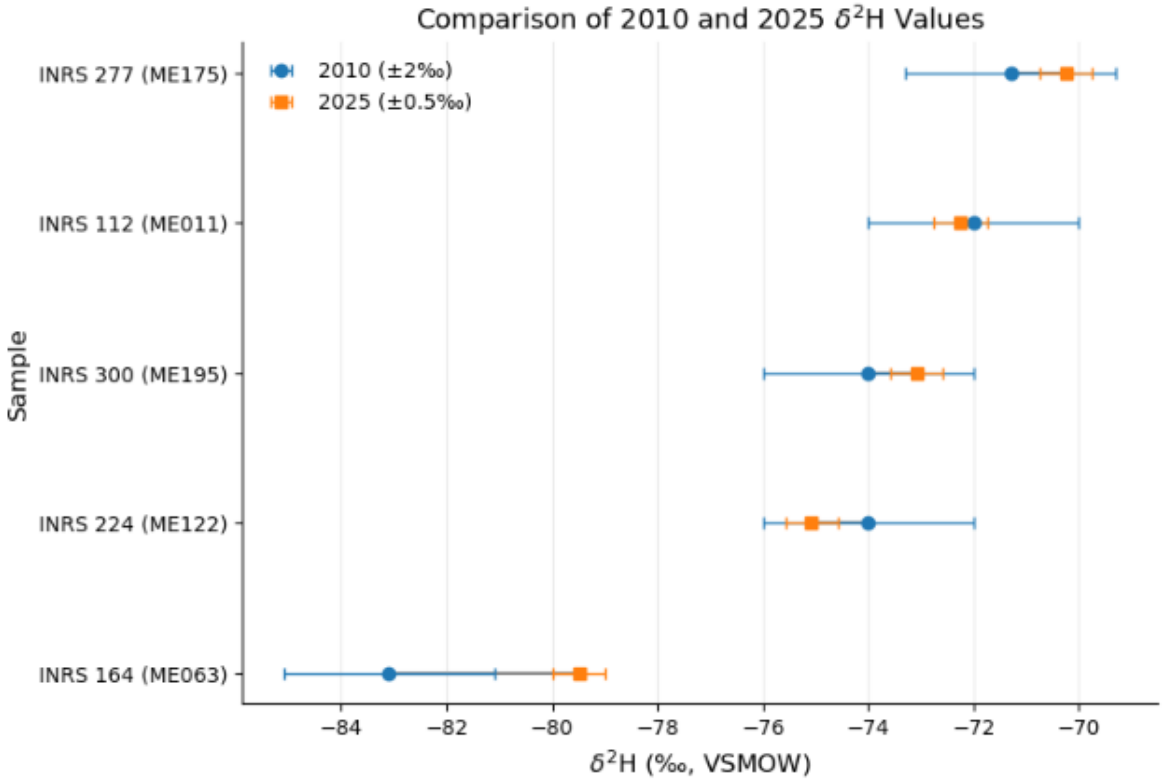


Figure 18. Temporal comparison of groundwater δ²H values at the resampled wells between the 2010 and 2025 field campaign. Comparison of groundwater δ²H values (‰ VSMOW) measured during the 2010 (blue circles) and 2025 (orange squares) field campaigns for five wells resampled in both years (INRS 164, INRS 224, INRS 300, INRS 112, and INRS 277). Each pair of symbols represents the measured δ²H value at the same well during the two sampling campaigns. Isotopic compositions are reported relative to Vienna Standard Mean Ocean Water (VSMOW). All values of the resampled data fall within 2 σ the reported uncertainty, although ME063 shows the largest observed δ²H shift among all the paired samples (1 σ= ± 2.0‰ for δ^2H in year 2010 and 1 σ= ± 0.5‰).

4.2. Aqueous geochemistry

4.2.1 Major Ion Trends

The major-ion chemistry of samples collected during the 2025 field campaign is summarized in Table 7 and Figure 19. Most groundwater samples exhibit Ca–Mg–HCO_3-type compositions, consistent with relatively less evolved groundwater affected by carbonate mineral dissolution. In contrast, ME122, ME175, and ME011 are comparatively enriched in Na and depleted in Ca and Mg, indicating greater hydrochemical evolution and possible ion exchange or mixing. ME241 and ME151 also display comparatively elevated Cl^- and SO_4^{2-} concentrations, respectively, while the river samples cluster more closely within the Ca–HCO_3 facies.

Table 7. Major ion concentrations and calculated carbonate species in groundwater samples collected during the 2025 field campaign in the Montérégie Est study area, Québec. HCO_3^- and CO_3^{2-} concentrations were not measured directly but were calculated from field alkalinity and pH measurements using carbonate equilibrium relationships (See Supplementary Material 12). Other reported major ion concentrations were analyzed at the Geochemistry Laboratory, Department of Earth and Environmental Sciences, University of Ottawa. All concentrations are reported in mg/L. With detection limit reported below in mg/L.

Sample ID	Ca (mg/L) (0.006963)	Mg (mg/L) (0.000235)	Na (mg/L) (0.014898)	K (mg/L) (0.001024)	HCO_3^- (mg/L)	CO_3^{2-} (mg/L)	Cl^- (mg/L) (0.010604)	SO_4^{2-} (mg/L) (0.005717)	F^- (mg/L) (0.007065)
ME241	82.03	14.48	75.67	3.37	277.6	0.74	105.58	31.94	0.138
ME143	73.18	17.12	8.76	1.39	143.82	0.25	4.3	43.12	0.18
ME122	0.58	0.17	317.52	3.69	274.87	8.71	84.79	0.65	4.829
ME063	62.98	10.66	11.07	0.9	54.29	0.06	23.76	20.19	0.072
ME175	0.19	0.01	172.05	0.23	224.89	0.16	38.82	27.62	0.136
ME031	16.67	5.55	40.37	3.25	46.82	0.62	4.11	6.17	0.359
ME050	19.72	3.26	74.66	1.02	63.97	0.4	5.34	16.36	0.195

ME003	133	21.23	18.45	15.77	629.86	1.8	6.67	53.62	0.122
ME064	43.76	16.16	3.91	0.82	211.32	0.27	3.41	8.38	0.052
ME195	82.89	17.05	25.38	2.89	375.28	0.6	12.28	82.64	0.084
ME007	58.56	7.24	54.63	2.89	187.2	0.04	68.75	21.49	0.068
ME011	14.53	1.23	98.41	1.23	162.53	1.33	70.75	33.14	0.345
ME039	53.24	20.58	35.47	1.27	293.18	1.09	36.08	19.8	0.187
ME151	86.29	32.25	57.1	5.64	63.97	0.4	81.76	103.37	0.349
R1	17.33	3.88	7.05	1.52	197.77	11.97	8.12	7.76	0.076
R2	18.29	2.87	8.35	1.56	329.81	6.25	9.34	5.78	0.068
R3	19.08	4.68	11.32	1.35	268.16	6.7	14.75	7.69	0.086

4.2.2 Piper Diagram Interpretation (Stosch, 2022)

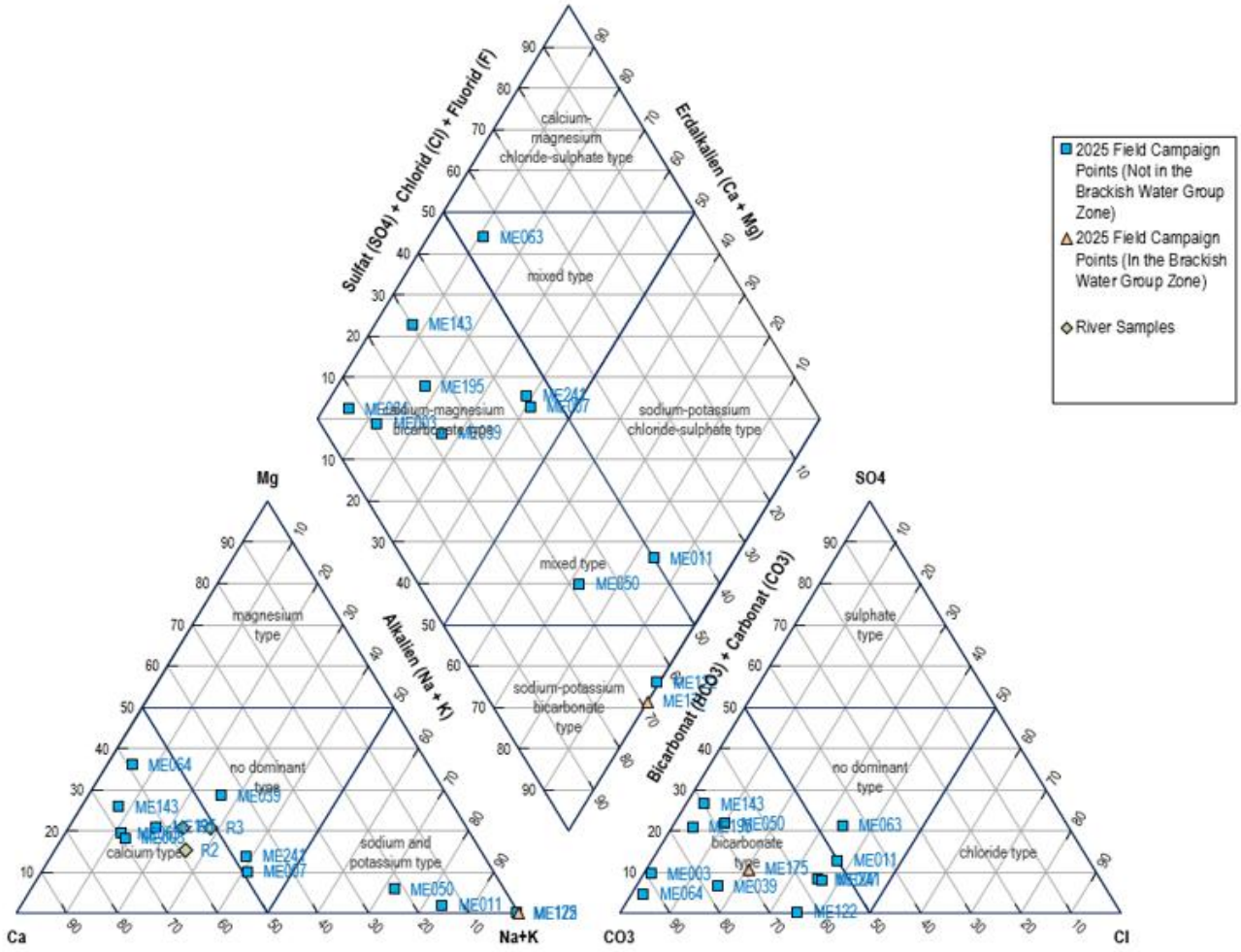


Figure 19. Hydrochemical facies of groundwater and surface water samples from the 2025 Montérégie Est field campaign using a Piper diagram. Piper diagram showing the major ion hydrochemical composition of groundwater and surface water samples collected during the 2025 field campaign within the Montérégie Est fractured bedrock aquifer system. Groundwater samples located within the mapped brackish groundwater zone (ME 175) is plotted separately from the remaining 2025 groundwater samples since they are located in the defined brackish water group, so they are highlighted in orange triangles out to represent potential hydrochemical evolution associated with brackish-zone influence (Beaudry et al., 2018). River samples (R1, R2, R3) are shown in green diamonds for comparison. The diagram illustrates variability in groundwater facies ranging from Ca- Mg - HCO3- type recharge waters to more evolved Na-rich groundwater associated with regional flow systems, ion exchanges, and potential water-rock interactions.

Table 8. Paired comparison of major-ion concentrations in groundwater samples collected during the 2010 and 2025 field campaigns in Montérégie Est, Québec. Values are presented as 2010 → 2025 concentrations in mg/L.

Well	Ca (mg/L)	Mg (mg/L)	Na (mg/L)	K (mg/L)	HCO_3^- (mg/L)	CO_3^{2-} (mg/L)	Cl^- (mg/L)	SO_4^{2-} (mg/L)
ME241	90.0 → 82.03	10.0 → 14.48	4.8 → 75.67	2.4 → 3.37	215.0 → 277.60	0.0 → 0.74	7.5 → 105.58	34.0 → 31.94
ME143	65.0 → 73.18	16.0 → 17.12	7.9 → 8.76	1.0 → 1.39	240.0 → 143.82	0.1 → 0.25	4.5 → 4.30	51.0 → 43.12
ME122	0.8 → 0.58	0.2 → 0.17	310.0 → 317.52	1.8 → 3.69	576.0 → 274.87	56.5 → 8.71	100.0 → 84.79	0.8 → 0.65
ME063	50.0 → 62.98	9.3 → 10.66	8.9 → 11.07	0.6 → 0.90	181.0 → 54.29	0.0 → 0.06	16.0 → 23.76	17.0 → 20.19
ME175	12.0 → 0.19	6.2 → 0.01	77.0 → 172.05	5.0 → 0.23	258.0 → 224.89	2.9 → 0.16	13.0 → 38.82	0.3 → 27.62
ME031	18.0 → 16.67	6.9 → 5.55	48.0 → 40.37	3.6 → 3.25	193.0 → 46.82	0.1 → 0.62	30.0 → 4.11	0.0 → 6.17
ME050	28.0 → 19.72	1.8 → 3.26	6.3 → 74.66	3.0 → 1.02	74.0 → 63.97	0.0 → 0.40	4.0 → 5.34	11.0 → 16.36
ME003	140.0 → 133.00	32.0 → 21.23	35.0 → 18.45	16.0 → 15.77	544.0 → 629.86	0.2 → 1.80	44.0 → 6.67	99.0 → 53.62
ME064	62.0 → 43.76	14.0 → 16.16	9.0 → 3.91	1.1 → 0.82	240.0 → 211.32	0.0 → 0.27	16.0 → 3.41	16.0 → 8.38
ME195	18.0 → 82.89	3.2 → 17.05	98.0 → 25.38	1.3 → 2.89	181.0 → 375.28	0.2 → 0.60	45.0 → 12.28	63.0 → 82.64
ME007	28.0 → 58.56	3.1 → 7.24	44.0 → 54.63	2.1 → 2.89	85.0 → 187.20	0.0 → 0.04	63.0 → 68.75	22.0 → 21.49

ME011	19.0	→	4.9	→	80.0	→	0.6	→	154.0	→	1.0	→	77.0	→	17.0	→								
	14.53		1.23		98.41		1.23		162.53		1.33		70.75		33.14									
ME039	39.0	→	20.0	→	32.0	→	0.7	→	189.0	→	0.7	→	62.0	→	26.0	→								
	53.24		20.58		35.47		1.27		293.18		1.09		36.08		19.80									
ME151	99.0	→	64.0	→	20.0	→	11.0	→	484.0	→	0.3	→	32.0	→	180.0	→								
	86.29		32.25		57.10		5.64		63.97		0.40		81.76		103.37									

Overall, the paired samples show site-specific hydrochemical variability rather than a consistent regional temporal trend. Several wells exhibit pronounced changes in Na, HCO_3^-, Cl^-, and SO_4^{2-} concentrations, indicating that local mixing, well conditions, water–rock interaction, or sampling variability may exert a stronger influence than uniform aquifer-wide change.

4.2.3 DIC and Alkalinity Patterns and other field parameters

Table 9. Comparison of hydrochemical parameters for groundwater samples collected in 2010 field campaign across the Montérégie Est study area (Beaudry et al., 2018).

Sample ID	INRS ID	Temp (°C)	DIC (ppmC)	pH	HCO_3^- (mg/L)	CO_3^{2-} (mg/L)	Alkalinity (mg/L as $CaCO_3$)
ME007	INRS108	13.6	43.2	6.1	85	0	70
ME008	INRS109	9.9	26	8.08	155	0.7	130
ME050	INRS151	10.4	47.4	5.99	74	0	61
ME061	INRS162	9	26	8.15	154	0.8	130
ME063	INRS164	10.4	54.6	6.53	181	0	150

ME066	INRS167	9	70.9	5.7	63	0	52
ME068	INRS169	9.9	25.8	7.48	145	0.2	120
ME092	INRS193	10.3	79.4	7.37	431	0.4	360
ME109	INRS211	10.6	54.7	8.62	324	6.1	280
ME111	INRS213	9	24.1	8.08	143	0.7	120
ME122	INRS224	10.5	107.2	9.33	576	56.5	580
ME125	INRS227	10.1	32.2	9.11	185	9.4	170
ME129	INRS231	10.7	110	7.12	540	0.3	460
ME149	INRS251	9.9	71.9	7.21	368	0.3	310
ME154	INRS256	10.2	69.7	7.8	405	1.1	340
ME175	INRS277	10.5	43.3	8.45	258	2.9	220
ME176	INRS278	11.7	64.4	8.02	378	1.8	320
ME178	INRS280	11	36.1	9.04	208	9.2	190

ME203	P06	9.9	43.2	8.5	258	3.3	220
ME214	P16	9	49	8.57	293	4.5	250
ME218	P19	10.7	18	9.38	94	9.3	98
ME219	P20	8.4	21.2	8.89	124	3.5	110
ME223	P23	9.3	119	8.95	665	31	620

Table 10. Hydrochemical parameters for groundwater samples collected in 2025 field campaign in the Montérégie Est study area (calculations of 2025 samples for HCO_3^-. CO_3^{2-} and alkalinity are shown in Supplementary Material 12).

Sample ID	**pH (2010)**	**HCO_3^- (2010) (mg/L)**	**CO_3^{2-} (2010) (mg/L)**	**Alkalinity (2010) (mg/L as $CaCO_3$)**	**pH (2025)**	**HCO_3^- (2025) (mg/L)**	**CO_3^{2-} (2025) (mg/L)**	**Alkalinity (2025) (mg/L as $CaCO_3$)**
ME003	6.93	544	0.2	460	7.9	629.86	1.8	520.4
ME007	6.1	85	0	70	6.8	187.2	0.04	153.11
ME011	8.22	154	1	130	8.5	162.53	1.33	136.7
ME031	7.26	193	0.1	160	8.5	46.82	0.62	39.4
ME039	7.94	189	0.7	160	7.9	293.18	1.09	242.02

ME050	5.99	74	0	61	8.2	63.97	0.4	53.24
ME143	7.03	240	0.1	200	7.6	143.82	0.25	118.14
ME151	7.05	484	0.3	410	8.2	—	—	—
ME063	6.53	181	0	150	7.4	54.29	0.06	44.48
ME064	6.41	240	0	200	7.4	211.32	0.27	173.55
ME122	9.33	576	56.5	580	8.9	274.87	8.71	239.09
ME175	8.45	258	2.9	220	7.2	224.89	0.16	185.91
ME195	7.49	181	0.2	150	7.6	375.28	0.6	308.43
ME241	6.4	215	0	180	7.8	277.6	0.74	228.23

Table 11. Comparison of carbonate system parameters for groundwater wells sampled for age tracers in 2010 and 2025 in the Montérégie Est study area (calculations of 2025 samples for HCO_3^-. CO_3^{2-} and alkalinity are shown in Supplementary Material 12).

	2025						2010					
Sample ID	Temperature °C	DIC ppmC	pH	HCO_3^- mg/L	CO_3^{2-} mg/L	Alkalinity mg/L as $CaCO_3$	Temperature °C	DIC ppmC	HCO_3^- mg/L	CO_3^{2-} mg/L	Alkalinity mg/L as $CaCO_3$	pH
ME007	25.6	49.7	6.8	187.2	0.04	153.11	9	43.2	85	0	70	6.10
ME050	17.2	12.9	8.2	59	0.46	48.5	10.4	47.4	74	0	61	5.99
ME063	19.1	11.7	7.4	54.29	0.06	44.48	10.4	54.7	181	0	150	6.53
ME122	18.8	55.8	8.9	274.87	8.71	239.09	10.5	107.2	576	56.5	580	9.33
ME175	20.6	51.3	7.2	249.8	0.18	205	10.5	43.3	258	2.9	220	8.45

4.3 Tritium

4.3.1 Tritium Model Accuracy Assessment

Measured (^{3}H) concentrations from the 2025 field campaign were compared with MT3D-USGS predictions generated using the transport model calibrated to the 2010 dataset (Figure 20; Table 26 in Supplementary Material 11). Overall, the model reproduced the broad range of tritium concentrations observed in 2025, including the absence of detectable tritium at ME064 and ME086 and the higher activities measured at ME241, ME143, and ME039. The regression between measured and predicted concentrations produced $R^2 = 0.866$ and an RMSE of 2.378 TU, indicating generally good agreement at the regional scale. The regression slope of 1.299 indicates that the model tended to overpredict tritium concentrations, particularly at several intermediate- and high-activity wells, including ME143, ME003, ME039, and ME151. In contrast, tritium was underpredicted at ME124. These differences likely reflect local variability in recharge, groundwater mixing, flowpath geometry, and recharge tritium concentrations that are not fully represented by the regional steady-state model. Despite these site-specific deviations, the agreement between the independently measured 2025 data and predictions generated from the 2010-calibrated model supports the model's overall ability to reproduce first-order regional patterns in modern groundwater occurrence.

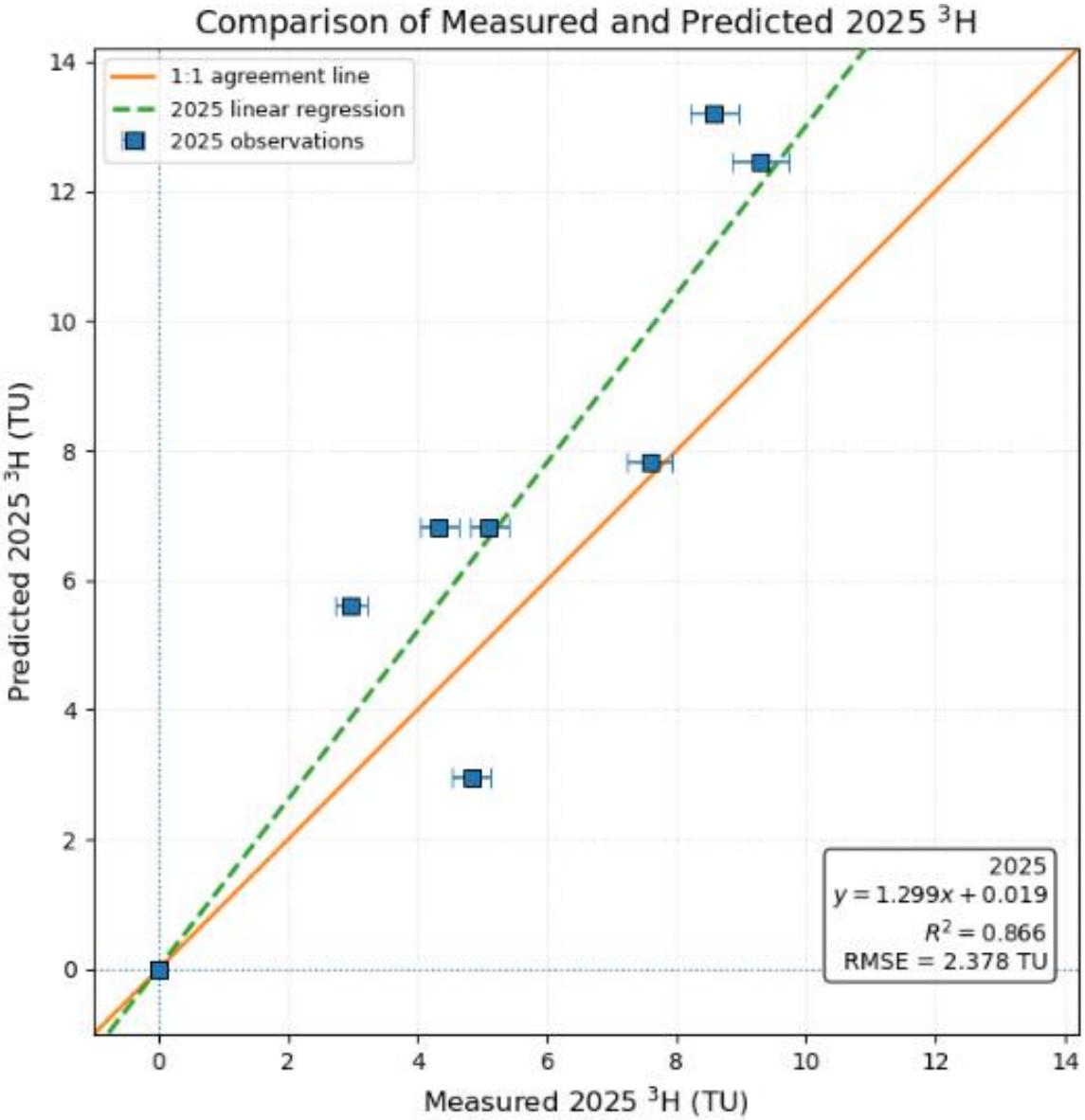


Figure 20. Comparison of measured and model-predicted ^{3}H concentrations for the 2025 model-evaluation dataset. Measured ^{3}H concentrations are plotted against MT3D-USGS-predicted concentrations for nine groundwater wells sampled during the 2025 field campaign. Horizontal error bars represent the sample-specific analytical uncertainties associated with the measured concentrations. The solid orange line indicates perfect 1:1 agreement, while the dashed green line represents the ordinary least-squares regression between measured and predicted values. The regression produced y = 1.299x + 0.019, R^2 = 0.866, and an RMSE of 2.378 TU, indicating that the model reproduced the broad spatial variability in tritium concentrations but tended to overpredict several intermediate- and high-activity samples. Measured and predicted values below 0.5 TU were assigned a value of 0 TU for plotting and statistical analysis. ME064 and ME086 therefore overlap at the origin, although both observations were retained in the regression. ME195 was excluded because of suspected localized river influence. (Data for this figure is shown in Supplementary Material 11, Table 26).

In addition, the 2025 data are presented alongside the 2010 data in Figure 21. Overall, both datasets follow the same positive measured–predicted relationship, indicating that the model captures the broad regional distribution of tritium (^3H) across the two sampling campaigns. The combined regression (R^2 = 0.796; RMSE = 2.517 TU) shows reasonable agreement, although the 2025 observations display somewhat greater scatter and a tendency toward overprediction at several intermediate- and high-concentration sites. The clustering of some predictions near 14 TU reflects the prescribed tritium concentration assigned to recharge zones and should therefore be interpreted with caution.

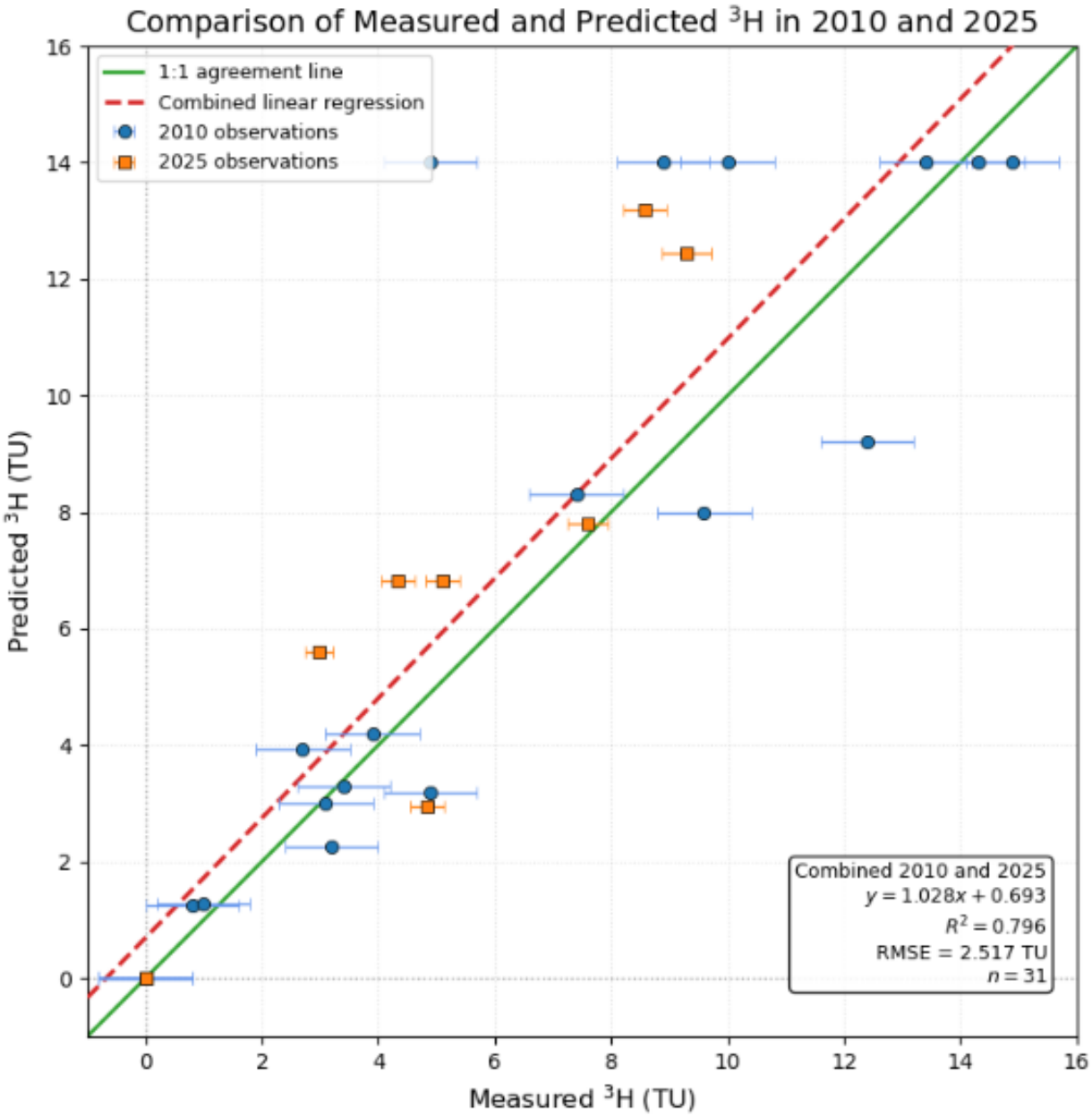


Figure 21. Combined comparison of measured and model-predicted ^3H concentrations for the 2010 and 2025 groundwater datasets. Blue circles represent the 22 groundwater observations from the 2010 calibration dataset, while orange squares represent the nine observations from the 2025 model-evaluation dataset. Horizontal error bars show analytical uncertainties of ±0.8 TU for the 2010 measurements and sample-specific uncertainties for the 2025 measurements. The solid green line represents the 1:1 relationship, and the dashed red line represents the ordinary least-squares regression fitted to all 31 observations. The combined regression produced $y = 1.028x + 0.693$, $R^2 = 0.796$, and an RMSE of 2.517 TU. Measured and predicted concentrations below 0.5 TU were assigned a value of 0 TU for plotting and statistical analysis. Overlapping observations at the origin were retained in the regression. ME195 was excluded from the 2025 dataset because of suspected localized river influence (Data in Supplementary Material 11).

Overall, the ^3H results indicate that the regional transport model reproduced the main measured concentration patterns in both the calibration and model-evaluation datasets. For the independent 2025 dataset, the regression produced $R^2 = 0.866$ and an RMSE of 2.378 TU (Figure 20), indicating a strong relationship between measured and predicted concentrations, although the regression slope of 1.299 shows that the model tended to overpredict several intermediate- and high-^3H values. When the 2010 and 2025 observations were evaluated together, the combined regression produced $R^2 = 0.796$, an RMSE of 2.517 TU, and a slope of 1.028 (Figure 21). The slope close to unity indicates that the model reproduced the overall measured–predicted relationship across both sampling campaigns, while the positive intercept and remaining scatter reflect localized differences in recharge, mixing, and flow conditions that are not fully represented by the regional model. Predictions clustering near 14 TU should also be interpreted cautiously because they are influenced by the prescribed tritium concentration assigned to model recharge zones. Broadly speaking, there is an overall good fit between the measured and model-predicted ^3H data.

4.3.2 Temporal Comparison Between 2010 and 2025 Groundwater Samples

Table 12. Temporal comparison of tritium (^{3}H) concentrations between the 2010 and 2025 groundwater sampling campaigns for resampled groundwater wells within the Montérégie Est fractured bedrock aquifer system.

Sample ID	Site ID	^{3}H 2010 (TU)	^{3}H 2025 (TU)	Δ (2025–2010)	Model prediction (TU)
ME007	INRS108	13.4	9.43 ± 0.39	↓ −3.97	14
ME050	INRS151	14.9	5.70 ± 0.31	↓ −9.20	14
ME063	INRS164	10	5.29 ± 0.28	↓ −4.71	8.77
ME122	INRS224	Below detection	<0.55	No detectable modern-recharge signal	0.48
ME175	INRS277	7.3	6.96 ± 0.34	↓−0.34	0
ME195	INRS300	2.6	5.84 ± 0.33	↑ +3.24	7.6

Overall, (^{3}H) concentrations decreased between 2010 and 2025 at four of the six resampled wells, with the largest decline observed at ME050. However, the temporal pattern was not uniform, as ME195 increased and ME122 remained below detection in both sampling campaigns.

4.4. Radiocarbon

4.4.1 Radiocarbon Model Accuracy Assessment

As with ^{3}H, the raw ^{14}C activities measured during the 2025 field campaign were compared with MT3D-USGS predictions generated using the model calibrated to the 2010 dataset (Figure 22; Supplementary Material 10, Table 27). The regression produced $R^2 = 0.984$, indicating a strong relationship between measured and predicted ^{14}C activities, while the RMSE of 3.316 pMC indicates relatively small prediction errors across the six groundwater samples. The regression equation, $y = 0.928x + 4.526$, has a slope close to one, showing that the model reproduced the overall measured concentration range, although the positive intercept and slope slightly below unity indicate modest overprediction at some lower-activity samples and underprediction at the upper end of the range. ME195 was excluded because of suspected localized river influence. Broadly speaking, there is an overall good fit between the measured and model-predicted 2025 ^{14}C data.

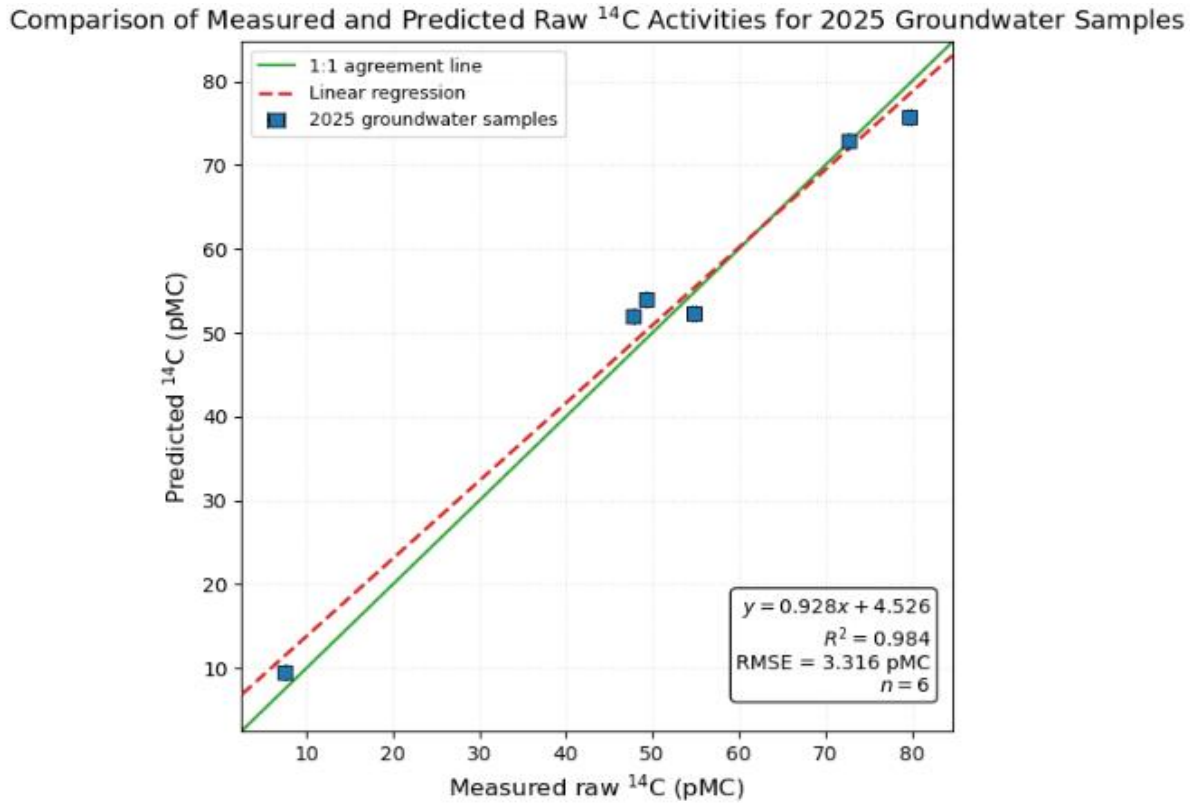


Figure 22. Comparison of measured and model-predicted raw ^{14}C activities for the 2025 groundwater dataset. Blue squares represent groundwater samples collected during the 2025 field campaign. Horizontal error bars show the analytical uncertainties associated with the measured 14C activities (too small to show on figure). The solid green line represents the 1:1 relationship, while the dashed red line represents the ordinary least-squares regression. The regression produced $y = 0.928x + 4.526$, $R^2 = 0.984$, and an RMSE of 3.316 pMC. Data for this figure is shown in Supplementary Material 10 Table 27.

In addition, the 2025 data is presented alongside the 2010 data in Figure 23:

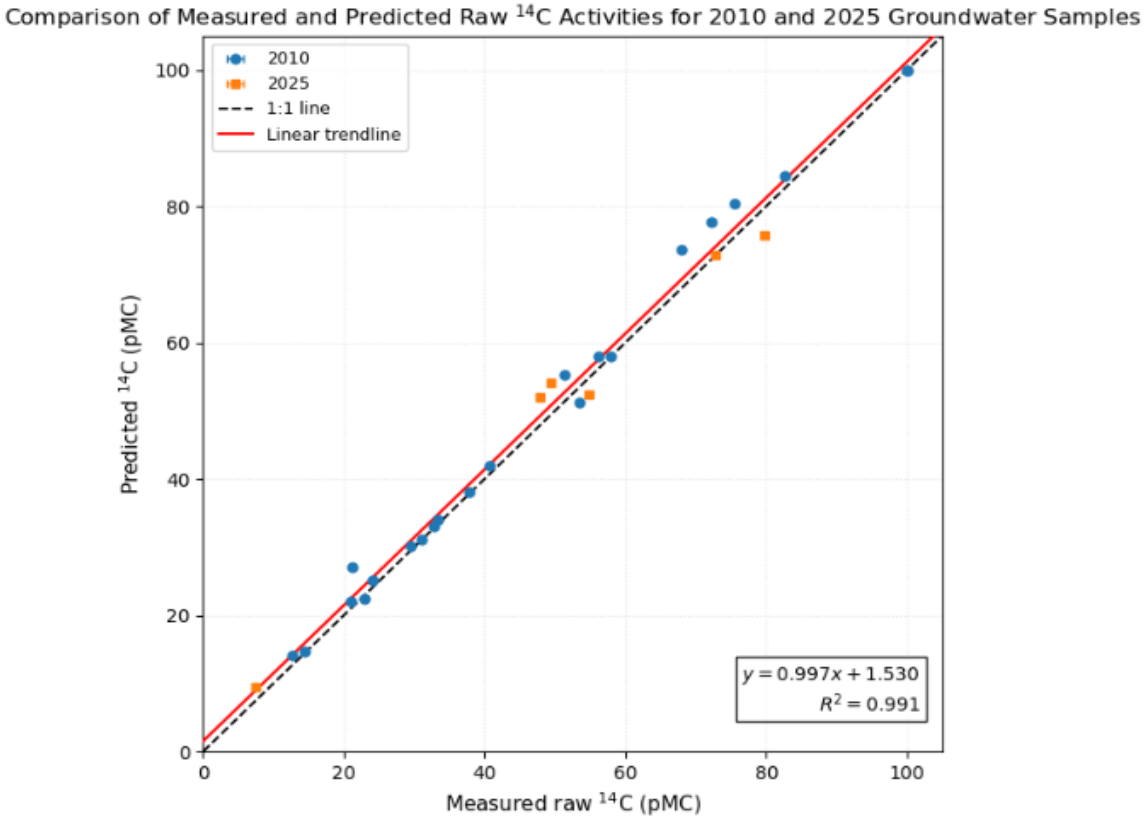


Figure 23. Combined comparison of measured and model-predicted raw 14C activities for the 2010 and 2025 groundwater datasets. Blue circles represent the 22 groundwater observations from the 2010 calibration dataset, while orange squares represent the six observations from the 2025 model-evaluation dataset. Horizontal error bars show analytical uncertainties of ±0.2 pMC for the 2010 measurements and sample-specific uncertainties for the 2025 measurements. The dashed black line represents the 1:1 relationship, while the solid red line represents the ordinary least-squares regression fitted to all 28 observations. The combined regression produced y = 0.997x + 1.530 and R^2 = 0.991 (Data for this figure are provided in Supplementary Material 11, Table 25 and 27).

When the 2010 and 2025 ^{14}C datasets were evaluated together, the combined regression produced R^2 = 0.991, indicating that the measured activities explained approximately 99% of the variation in the model-predicted values (Figure 23). The regression slope of 0.997 was almost identical to the ideal value of one, while the relatively small positive intercept of 1.530 pMC indicates only a slight overall tendency toward overprediction. The RMSE of approximately 2.801 pMC further indicates that the model predictions generally remained close to the corresponding measured activities across the full concentration range. The 2025 observations also broadly follow the relationship defined by the 2010 calibration dataset, supporting the model's ability to reproduce the regional distribution of raw ^{14}C activities

beyond the original calibration period. Broadly speaking, there is an overall good fit between the measured and model-predicted ^{14}C data.

4.4.2 Temporal Comparison Between 2010 and 2025 Groundwater Samples

The ^{14}C data for the six 2010 wells which were resampled for age tracers in 2025 are presented in Table 13.

Table 13. Temporal comparison of groundwater age-tracer results between the 2010 and 2025 field campaigns for resampled borehole wells within the Montérégie Est fractured bedrock aquifer system.

Well ID	Water group	Distance from recharge zone (m)	2010 raw (^{14}C) (pMC)	2025 raw (^{14}C) (pMC)	Change in (^{14}C) (pMC)
ME007	A1	0	106.1	66.58	−39.52
ME050	A1	0	106	59.16	−46.84
ME063	A3	0	57.9	52.06	−5.84
ME122	M1	6817.14	21.2	22.13	0.93
ME175 *	M2	256	47.6	82.53	34.93
ME195 *	A2	104	39	68.77	29.77

Note: *ME175 and ME 195 were treated as anomalous groundwater samples due to the substantial increase in measured raw ^{14}C between the 2010 and 2025 field campaigns relative to the overall decreasing trend observed in the other resampled wells. This data may reflect localized river influence and/or enhanced surface-water recharge contribution within the regional groundwater flow system (See Discussion - 5.4 River Influence).*

As shown in Table 13 the temporal changes in raw ^{14}C activity were site-specific with no overall consistent trend observed: ME007, ME050, and ME063 decreased between 2010 and 2025, whereas ME122 remained approximately stable. The increases at ME175 and ME195 differ from this general pattern and may reflect localized river or surface-water influence.

Chapter 5. Discussion

5.1 Model Results Discussion

5.1.1 ModelMuse Results

The simulated hydraulic heads reasonably reproduced the measured 2010 heads across the observed range, with a regression of $y = 1.029x - 3.341$, $R^2 = 0.981$, an RMSE of 12.57 m, and a near-zero bias of −0.58 m (Figure 12). These results indicate that the model captures the regional hydraulic-head gradient without a strong systematic tendency to overpredict or underpredict heads, although several individual wells show larger residuals.

The modeled distribution of higher hydraulic heads in the Appalachian Uplands and other topographic highs, followed by decreasing heads toward the Piedmont and St. Lawrence Lowlands, is consistent with the conceptual model of Beaudry et al. (2018). Their interpretation proposed regional groundwater movement from recharge areas in the Appalachian Uplands toward discharge and mixing zones along the western Piedmont and locally within the Lowlands near the Monteregian Hills, while groundwater flow in the low-lying, confined northern Lowlands was considered comparatively limited. The MODFLOW results generated here therefore provide quantitative hydraulic support for the regional flow pattern previously inferred from hydrogeochemical and isotopic evidence. Overall, the coupled MODFLOW–MODPATH–MT3D-USGS model successfully reproduced the principal hydraulic features of the Montérégie Est groundwater system. The close agreement between measured and simulated hydraulic heads indicates that the model captured the regional hydraulic gradients, while the simulated flow pathways were consistent with the recharge-to-discharge patterns proposed in the regional conceptual model (Figures 12–13).

The model also reproduced the spatial variation in tritium (^3H) and raw radiocarbon (^{14}C) within the 2010 calibration dataset (Figures 13–14). Crucially, the model was additionally validated by the 2025 field campaign data as highlighted in Figures 20-23. Broadly speaking, the model provides a good representation of regional groundwater flow, flow pathways, mixing, and age-tracer evolution.

This stable isotope provides an important link between the field-sampling design and the numerical modelling results, as they support the regional representativeness of the selected sampling locations, while the hydraulic-head, particle-tracking, and age-tracer comparisons provide more direct tests of the simulated groundwater-flow and transport system.

The stable isotope results also provide independent support for the MODPATH-7 guided sampling strategy used during the 2025 field campaign. Since sampling locations were

selected within approximately 250 m of major MODPATH-7-defined advective groundwater flowpathways identified through particle-tracking simulations (See Methods Section). The relatively narrow isotopic range observed among groundwater samples suggests that the sampled wells were recharged under broadly similar meteoric conditions and are connected to a common regional groundwater flow system. If the selected wells were dominated by different recharge sources or isolated local flow systems, greater variability in $\delta^{2}H$ and $\delta^{18}O$ values and the development of distinct isotopic groupings would be expected. Instead, groundwater samples form a relatively tight cluster along the BLMWL (Figure 17), suggesting that the sampled wells are representative of groundwater moving along the major regional flowpaths identified by the groundwater flow model.

This observation has important implications for the interpretation of groundwater age tracers discussed in subsequent sections in the Discussion Section. Although a large variation in measured ^{14}C activities is observed among wells with respect to measured ^{14}C activities, hydrochemical composition, and groundwater residence times, the stable isotope data suggest that these differences are unlikely to result from fundamentally different recharge sources. Rather, the similarity in groundwater isotope compositions indicates that much of the observed variation developed after recharge through processes occurring within the aquifer system, including groundwater mixing, water-rock interaction, dead carbon addition, and progressive geochemical evolution along groundwater flowpaths. In addition, temporal variations in recharge rates and recharge timing may influence the contribution of modern recharge, thereby affecting measured age tracer signatures. Overall, the stable isotope results suggest that differences in groundwater age tracer signatures are not primarily controlled by variations in recharge origin (Figure 17-18, Table 5-6). Instead, the observed variabilities in age tracers and major ion datasets are more likely related to processes occurring after recharge along flowpathways.

5.1.2 MODPATH-7 Results Discussion

The MODPATH-7 particle tracking results generally support the regional groundwater flow framework proposed by Beaudry et al. (2018), which inferred the presence of nested local, intermediate, and regional flow systems across the Montérégie Est fractured bedrock aquifer system. The simulated flowpathways reproduce the major recharge and discharge relationships identified from hydrogeochemical and isotopic evidence, including recharge within the Appalachian Uplands and groundwater migration toward discharge and mixing zones within the St. Lawrence Lowlands.

From this robust model, distinct groundwater flow patterns are evident among the major hydrogeological contexts through MODPATH-7 numerical modelling of the major advection flowpathways (Figure 13). In the Northern St. Lawrence Lowlands, simulated flowpathways are generally longer and rarely terminate in nearby surface-water bodies (Figure 13). This behaviour is consistent with the presence of thick Champlain Sea clay deposits that create confined hydraulic conditions and promote deeper regional groundwater circulation (Beaudry et al., 2018). In contrast, flow pathways within the Southern St. Lawrence Lowlands are also relatively long but commonly intersect major river systems, suggesting that rivers act as important discharge boundaries for regional groundwater flow (Figure 13). Within the Appalachian Uplands, simulated flowpathways are shorter and terminate in nearby valleys and streams, indicating the predominance of local flow systems characterized by relatively rapid recharge and discharge (Figure 13). The model generated flowpathways patterns broadly agree well with the flow system described by Beaudry et al. (2018).

Overall, two dominant regional groundwater flow directions were identified from the model. The first follows a general southeast-to-northwest trend from the Appalachian Uplands toward the St. Lawrence Lowlands, while the second converges toward major river valleys and regional discharge zones within the Lowlands (Figure 13). These simulated patterns are consistent with the conceptual interpretation of groundwater circulation proposed by Beaudry et al. (2018), who inferred relatively deep groundwater movement westwards from the Appalachian highlands toward mixing zones located near the Appalachian frontal thrust faults and around the Monteregian Hills (Details in Introduction).

5.1.3 MT3D-USGS result discussion

The MODFLOW-NWT and MT3D-USGS simulations represent steady-state groundwater-flow and tracer-transport conditions under constant boundary conditions and model parameters. Following calibration to the 2010 hydraulic-head and age-tracer observations, the model configuration remained unchanged when it was evaluated against the 2025 dataset. An additional 15-year transient simulation was not conducted because the objective was not to reproduce the year-by-year movement of the 2010 water masses, but to evaluate whether the calibrated regional system could represent the long-term hydrochemical conditions sampled independently in 2025. The transport simulations were run for sufficient time to approach a stable concentration distribution, such that additional simulation time produced negligible changes after radioactive decay, advection, dispersion, and mixing had reached dynamic equilibrium. The overall agreement between measured and simulated ^{14}C and ^{3}H activities indicates that the steady-state representation reasonably captures the dominant regional residence-time and tracer-distribution patterns. However, this agreement supports the suitability of the steady-state assumption rather than proving that all groundwater conditions remained physically unchanged between 2010 and 2025. Local differences between the two datasets may therefore represent transient processes, sampling variability, or processes that cannot be resolved by the regional steady-state model.

5.2 Identifying and characterising water-rock interactions

5.2.1 Dead Carbon Addition Along Groundwater Flowpaths

In the MT3D-USGS simulations, dead carbon addition was not explicitly represented in the model as a geochemical reaction occurring continuously along groundwater flowpathways in this regional model. Instead, to represent the dead carbon added into the groundwater system using MT3D-USGS, radiocarbon dilution associated with dead carbon inputs was incorporated at the point of recharge through adjustments to the initial ^{14}C activity assigned to recharge water (See the Numerical Model Building Section). This approach assumes that of radiocarbon dilution only significantly occurs during recharge and early groundwater evolution, when infiltrating water first interacts with carbonate-bearing minerals and soil-zone carbon sources (i.e. dead carbon addition via water-rock interaction only occurs at recharge with no additional radiocarbon exchange occurring along simulated flowpathways). To evaluate the validity of this assumption, a sensitivity analysis was conducted comparing the ratio of model-predicted to measured ^{14}C values with distance from PACES-defined major recharge zones (Figure 24).

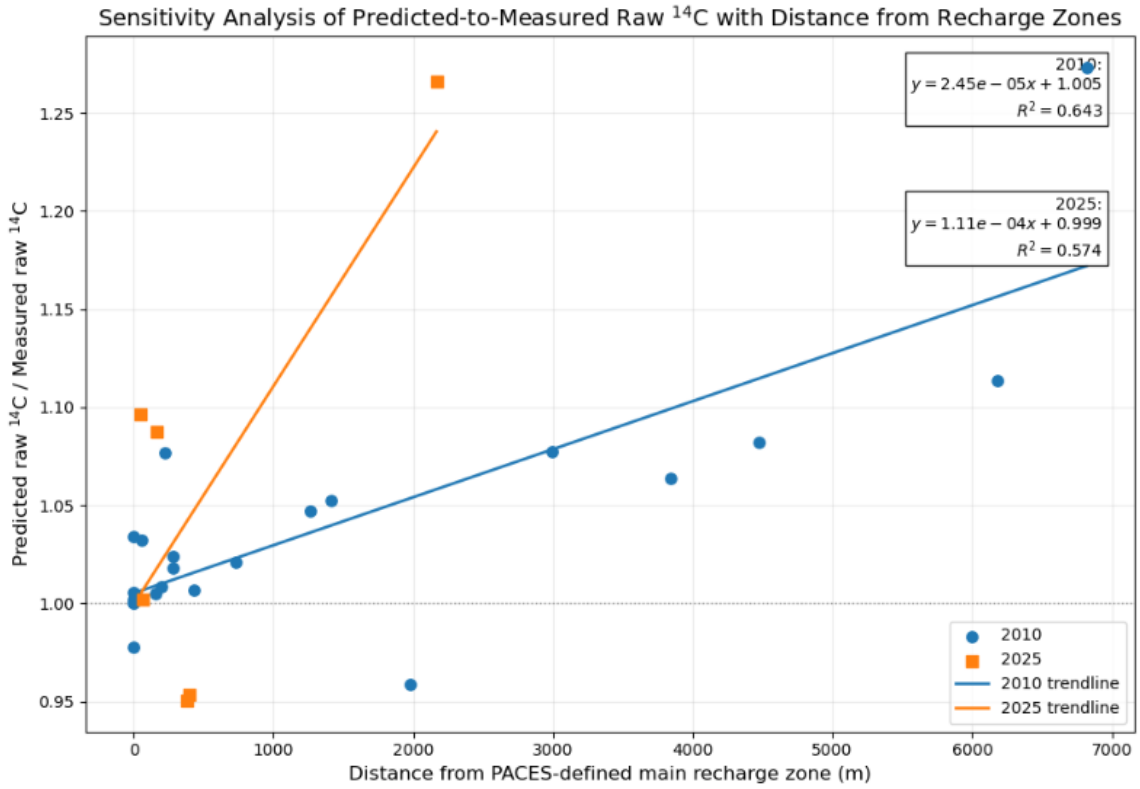


Figure 24. Sensitivity of Simulated ^{14}C Model Performance to Distance from Major Recharge Zones. Sensitivity analysis showing the relationship between the ratio of model-predicted to measured ^{14}C values and the distance from PACES-defined major recharge zones

for the 2010 (blue) and 2025 (orange) groundwater datasets. Distances represent the approximate separation between sampling wells and the nearest major recharge area used as recharge input locations for dead-carbon addition in the MT3D-USGS simulations. Trendlines illustrate changes in model performance with increasing distance from recharge zones and highlight the influence of recharge proximity and along-flow-path water–rock interactions on simulated ^{14}C distributions. Values above 1 indicate modelled ^{14}C is greater than measured (data for this figure is in Supplementary Material 11).

If significant dead carbon addition continues to occur along groundwater flow pathways through ongoing water-rock interaction, deviations between model-predicted and measured ^{14}C values would be expected to increase systematically with distance from recharge due to *in situ* dilution via radiocarbon-dead sources not accounted for in the model. Conversely, if most radiocarbon dilution occurs near recharge, there should be no discernible relationship between model performance and distance.

In this study, both the 2010 and 2025 datasets exhibit a positive trend between predicted and measured ^{14}C ratios and distance from recharge, suggesting the addition of dead carbon via water-rock interaction following the reasoning above (Figure 24). However, the 2025 dataset reveals a steeper fitted gradient ($1.11 \times 10^{-4)}$ than that for the 2010 dataset (2.45×10^{-5}). Several factors may explain this difference. First, differences in the number and spatial distribution of sampling locations between the two datasets may influence the fitted regression slopes. Although the 2010 dataset contains more observations and covers a greater distance range from the PACES-defined recharge zones, most samples are located relatively close to recharge, meaning that a small number of distal observations exert a disproportionate influence on the fitted trendline. Therefore, some of the differences observed between the 2010 and 2025 gradients may reflect sampling distribution and statistical leverage rather than solely hydrogeological processes. Second, differences in lithology may influence the rate of dead carbon addition, as groundwater samples collected from different bedrock units may experience varying degrees of water–rock interaction and carbonate dissolution along flowpaths. Finally, the observed differences may reflect temporal changes in groundwater conditions between 2010 and 2025, including variations in recharge dynamics, groundwater abstraction, residence times, or geochemical conditions that influence radiocarbon evolution. The first two factors are explored in detail below to assess its potential influence on the observed differences between the 2010 and the 2025 datasets, and potential temporal trends are evaluated in Section 5.2 and 5.3.

The first explanation for the difference in regression slopes observed between the 2010 and 2025 datasets is the influence of spatial distribution of individual observations within each

dataset. Although the 2010 dataset contains a larger number of samples and extends farther from the PACES-defined major recharge zones than the 2025 dataset, much of this extended distance range is represented by a limited number of distal observations. In particular, the 2010 regression is strongly influenced by a single sample located approximately 6817 m from the PACES-defined recharge zone. Because regression slopes are sensitive to both the distribution and range of observations along the independent variable, the presence of a small number of high-leverage distal points may substantially influence the fitted relationship between predicted-to-measured ^{14}C ratios and distance from recharge. In the present study, the majority of 2025 observations are located within approximately 1000 m of the PACES-defined recharge zones, while only a small number of samples occur at substantially greater distances. As a result, the overall regression slope is heavily influenced by a limited number of distal observations, particularly the sample located at approximately 2166 m from recharge (See Supplementary Material 10). If these distal observations are affected by site-specific factors such as lithology, carbonate abundance, groundwater mixing, or localized water-rock interactions, the resulting regression slope may reflect those local controls rather than a purely distance-dependent process. Therefore, interpretation of the 2025 regression trend requires caution, as a small number of lithologically influenced high-leverage observations may disproportionately affect the apparent relationship between recharge distance and model performance.

In addition to these statistical effects, differences in sampling strategy between the two field campaigns further influence the regression-derived trends. The 2025 sampling campaign primarily targeted locations that are 250 m close to MODFLOW-NWT and MODPATH-7 derived major advection flowlines, resulting in a clustering of sampling points along hydraulically meaningful pathways. As a result, many 2025 samples tend to be concentrated in recharge-proximal regions and are more likely to represent groundwater with shorter residence times and reduced cumulative water–rock interaction. This targeted approach introduces a non-random spatial distribution of observations, which biases the dataset toward early-stage geochemical conditions and advective transport regimes.

Therefore, by focusing on major advective pathways identified through MODFLOW and MODPATH simulations, the 2025 dataset captures geochemical changes that are directly associated with groundwater transport along dominant flowlines, which are critical for understanding regional-scale flow systems. As such, while the dataset may not fully represent

the entire range of aquifer heterogeneity, it offers a process-oriented perspective on groundwater evolution along preferential pathways.

The second factor that may contribute to the differences observed between the 2010 and 2025 datasets is lithological variability among the sampled wells. Dead carbon addition is strongly influenced by groundwater interaction with carbonate-bearing minerals, as dissolution of radiocarbon-free carbonate rocks can dilute DIC ^{14}C activities and produce apparently older groundwater ages (Clark & Fritz, 1997). Also, variations in bedrock lithology and carbonate mineral abundance may influence the rate and magnitude of dead carbon addition along groundwater flow pathways.

Of the sampling locations considered, five wells containing age tracer data (^{14}C and ^{3}H) were sampled during both the 2010 and 2025 field campaigns (Table 4), whereas the remaining wells were not consistently resampled. As a result, the two datasets do not represent identical lithological conditions. Differences in bedrock composition among sampling locations may therefore contribute to the observed differences in regression slopes between the 2010 (2.45×10^{-5}) and 2025 (1.11×10^{-4}) datasets.

As shown in Table 21 in the Supplementary Material 6, the resampled wells span a range of lithological settings, including siliciclastic, metamorphic, and carbonate-bearing units. However, a key distinction between the 2010 and 2025 datasets lies in the lithological composition of wells that were not consistently resampled. In the 2010 dataset, several non-resampled wells intersect a broader range of lithologies, including ultramafic (e.g., peridotite, gabbro), metamorphic (e.g., schist), and mixed sedimentary units (Supplementary Material 6 Table 21), whereas the 2025 dataset includes a greater proportion of wells associated with mudrock, shale, and carbonate-bearing formations (Supplementary Material 6 Table 21). This difference in lithological representation introduces spatial variability in geochemical conditions that may directly influence the evolution of DIC and, therefore, measured ^{14}C values.

Carbonate-bearing lithologies (e.g., limestone, dolostone, calcareous mudstone) contribute radiocarbon-dead carbon (dead carbon) through dissolution processes (details in Introduction), leading to dilution of ^{14}C activity in groundwater (Clark & Fritz, 1997; Appelo & Postma, 2005).On the other hand, silicate - dominated lithologies such as sandstone, schist, and crystalline rocks typically contain lower amount of carbonate minerals than limestone - and dolostone - bearing units (Fryar, 2021). Therefore, groundwater interacting with these lithologies is expected to receive a smaller contribution of dead carbon through mineral dissolution, reducing the potential for ^{14}C dilution relative to carbonate - rich aquifer materials

(Clark & Fritz, 1997; Appelo & Postma, 2005). As groundwater flows through carbonate-rich or lithological units mixed with carbonate-rich units, progressive water–rock interaction after point of recharge can increase the proportion of dead carbon in solution, resulting in lower measured ^{14}C values relative to recharge conditions, even in the absence of significant increases in residence time.

In this study, differences in the lithological composition of wells included in the 2010 and 2025 datasets may influence the apparent relationship between distance from recharge and predicted-to-measured ^{14}C ratios. Wells intersecting carbonate-bearing or mixed sedimentary lithologies may experience greater incorporation of radiocarbon-dead carbon through continued water-rock interaction, resulting in lower measured ^{14}C activities relative to model predictions. This would manifest the steeper regression slope (1.11×10^{-4}) in the 2025 dataset compared to the 2010 dataset (2.45×10^{-5}), not necessarily due to increased groundwater age or flowpath length, but as a result of lithologically controlled geochemical evolution. Notably, the well located at the greatest distance from the recharge zone (ME122; ~6800 m) occurs within the 2010 dataset and is characterized by shale and mudstone units interbedded with sandstone, siltstone, and limestone, indicating the presence of carbonate-bearing material along the flowpath (Supplementary Material 6 Table 21). This well represents the most distal observation included in the regression analysis and exhibits one of the largest models overpredictions of ^{14}C activity (predicted/measured ratio = 1.27 in 2010). Because dead carbon contributions are applied only at recharge in the current model setup, additional incorporation of radiocarbon-dead carbon through continued water-rock interaction along the flowpath is not represented. Therefore, ME122 provides a plausible example of how lithologically controlled geochemical evolution may contribute to increasing divergence between model-predicted and measured ^{14}C values at distal locations. Additionally, ME122 plots within the sodium–bicarbonate field and shows elevated bicarbonate concentrations, high alkalinity values, and persistently low measured ^{14}C activities (Figure 19 & Table 8 & Table 11). This suggests that the water sampled at this location has undergone significant interactions with carbonate-bearing lithology units.

Additional evidence supporting the influence of carbonate-bearing lithologies on the observed regression relationship is further provided by the Piper diagram (Figure 19). Most groundwater samples plot within the calcium–magnesium–bicarbonate hydrochemical facies, indicating that groundwater chemistry throughout much of the study area is strongly influenced by carbonate dissolution and carbonate buffering reactions. However, several groundwater

samples, including ME122, ME175, ME011, and ME050, exhibit more evolved hydrochemical compositions characterized by increasing sodium relative to calcium and magnesium. Such hydrochemical signatures are commonly associated with prolonged groundwater residence times, continued water–rock interaction, and cation-exchange processes occurring along regional groundwater flowpaths (Appelo & Postma, 2005). The sodium enrichment observed in ME122 and ME175 may also reflect the influence of the brackish water group identified by Beaudry et al. (2018) within the northern St. Lawrence Lowlands. Groundwater associated with this water group has been interpreted as reflecting residual marine influences linked to Champlain Sea sediments and brackish groundwater evolution. Therefore, the elevated sodium concentrations observed in these samples may result not only from progressive water–rock interaction, but also from hydrochemical processes associated with saline or formerly marine-influenced groundwater systems.

The distribution of groundwater samples on the Piper diagram as well as Table 11 which compares the major ion data measured in 2010 and 2025 suggest that there is a variability in the extent to which groundwater has interacted with carbonate-bearing lithologies following recharge (Figure 19 & Table 8 & Table 12). As a result, more localised variability in water rock-interaction may contribute to the lower measured ^{14}C activities observed at several locations independently of groundwater residence time. Indeed, because the 2025 field campaign includes a greater proportion of groundwater samples potentially influenced by carbonate-bearing and mixed sedimentary lithologies, part of the steeper gradient in the predicted-to-measured ^{14}C gradient for the 2025 data may reflect enhanced rates of dead carbon incorporation associated with specific water–rock interactions rather than solely increases in groundwater age or flowpathway length.

Although HCO_3^-, CO_3^-, and alkalinity values are lower in 2025 compared to 2010 (Table 8& Table 11), the overall geochemical data from both sampling periods continue to indicate a groundwater system dominated by carbonate buffering along the flow pathways. This interpretation is consistent with the lithological framework of the study area, where the 2025 sampling campaign includes a greater proportion of wells intersecting carbonate-bearing or mixed sedimentary units (e.g. mudrock, shale, and dolostone; Table 20 in the Supplementary Material 6). Despite this increased representation of carbonate lithologies, bicarbonate and alkalinity values at key resampled wells such as ME122 and ME163 decrease between 2010 and 2025 (Table 11), indicating that carbonate presence alone does not directly control the observed concentration changes.

To summarise, although the linear regression–derived trendline for the combined dataset can be used as a first-order approximation to evaluate potential increases in dead carbon addition along major flowpaths due to water–rock interactions, there is likely a strong dependence on local conditions, as demonstrated by the two distinctive regression lines presented here. Therefore, when evaluating regional processes, the use of the combined dataset is expected to provide a more robust approach for capturing the overall broader gradient of geochemical evolution along flowpaths, while minimizing biases associated with dataset-specific sampling distributions.

5.3 Evaluating potential temporal trends in the data

The groundwater flow and transport model developed in this study was calibrated using the 2010 age-tracer dataset. Therefore, data generated by the 2025 field campaign can be used to evaluate broad trends and also identify potential temporal shifts in the hydrogeologic processes occurring in the region over the 15-year period.

Starting with the stable isotope data, comparison of stable isotope compositions between the 2010 field campaign and the 2025 field campaign indicates that groundwater isotope signatures remained broadly consistent over the 15-year period (Table 6; Figure 18). All five resampled wells exhibit negligible changes in both $\delta^{18}O$ and $\delta^{2}H$ values, suggesting that the sources and mechanisms of groundwater recharge remained generally stable between sampling periods. This observed consistency within the 15 years' timeframe indicates that no major shift in recharge origin occurred during the study period. However, stable isotope data alone do not provide direct information on changes in recharge rates, groundwater residence times, or the proportion of modern recharge entering the aquifer system. Therefore, temporal variations on these factors should be further evaluated using age tracers and hydrochemical datasets.

Comparison of measured and model-predicted radiocarbon values indicates that the model reproduced the 2010 age-tracer observations with high accuracy ($R^2 = 0.993$) between measured and predicted raw ^{14}C values. When evaluated against the independent 2025 field campaign dataset, the model continued to reproduce groundwater age-tracer distributions with similarly high accuracy despite no additional calibration being performed, yielding an R^2 value of 0.984 between measured and model-predicted raw ^{14}C values. Furthermore, the combined 2010 and 2025 dataset produced an R^2 value of 0.991, with regression relationships remaining close to the 1:1 line (Figure 23). The persistence of this strong agreement suggests that the regional groundwater flow framework represented by the model remained broadly valid between the two sampling campaigns, suggesting no significant temporal changes in groundwater conditions between 2010 and 2025.

Additional evidence for temporal stability is provided by the age-tracer results from the resampled wells (Table 12 & Table 13). Excluding wells influenced by recharge variability or river-water mixing, the remaining resampled groundwater wells exhibited relatively minor changes in measured radiocarbon activities over the fifteen-year monitoring period. Raw ^{14}C values at ME063 decreased from 57.9 pMC in 2010 to 52.06 pMC in 2025, while ME122 remained effectively unchanged, increasing only slightly from 21.2 pMC to 22.13 pMC. These

relatively small differences in the radiocarbon values over the 15-year sampling period suggest that regional groundwater residence times and large-scale groundwater flow patterns remained broadly stable between the two sampling campaigns. Likewise, with respect to tritium, while there is an observed variability between the 2010 and 2025 datasets no consistent overall trend is observed, with some wells indicating a decrease while others unchanging or increasing (Table 12). This variability may be, in part, due to an increased sensitivity of inputs relative to radiocarbon. This is because unlike radiocarbon, which reflects groundwater evolution over decadal- to millennial-scale timescales, tritium is highly sensitive to the proportion of recently recharged groundwater within a mixed groundwater system. For example, the slight decrease in measured ^{14}C activity at ME063 from 57.9 to 52.06 pMC, together with modest increases in calcium, magnesium, sodium, and chloride concentrations between 2010 and 2025 is matched by a decrease of 4.71 TU (Table 11 & Table 12). suggest that the 2025 sample may potentially contain a slightly greater proportion of older and more geochemically evolved groundwater (≥ 60 years) which can affect tritium values to a much greater extent than radiocarbon. Therefore, the observed tritium variability may reflect more older groundwater mixing in ME063, and a greater sensitivity overall to moderate changes in relative subsurface contributions to groundwater rather than a fundamental modification of regional groundwater flow pathways, however this would require further investigation to confirm this.

These observations suggest that the 2025 samples may contain a slightly greater contribution from older or more geochemically evolved groundwater, particularly at ME063, where modest increases in Ca, Mg, Na, and Cl coincide with a slight decrease in measured ^{14}C activity. Furthermore, the persistence of elevated sodium and chloride concentrations at ME122, together with its location within the brackish water group identified by Beaudry et al. (2018), suggests that mixing with geochemically evolved groundwater remains an important control on groundwater chemistry within portions of the study area. The observed increases in sodium and chloride concentrations at some locations may indicate a slightly greater contribution from groundwater associated with the regional brackish water group, although the available data do not demonstrate a substantial expansion of the brackish groundwater system. Nevertheless, these observations suggest that evolved groundwater sources continue to influence groundwater chemistry and may contribute to the increasing discrepancy between measured and model-predicted age-tracer values along longer regional flowpaths. From a groundwater resource management perspective, continued mixing between fresh groundwater and more evolved brackish groundwater may have implications for long-term groundwater

quality, particularly in areas located near the transition zone between fresh and brackish groundwater systems.

This interpretation is consistent with the sensitivity analysis results. The relationship between the predicted-to-measured ^{14}C ratio and distance from the PACES-defined recharge zones exhibits a slightly steeper slope in the 2025 dataset (approximately 2.45×10^{-5}) than in the 2010 dataset (approximately 1.11×10^{-5}) (Figure 24). The increase in slope suggests that discrepancies between measured and model-predicted radiocarbon values become slightly more pronounced with increasing distance from recharge areas in the 2025 dataset. As the model was not recalibrated using the 2025 age-tracer data and continues to reproduce measured ^{14}C values with a high degree of accuracy, the observed increase in slope is more likely related to modest changes occurring within the groundwater system than to deterioration in model performance. When considered together with the hydrochemical evidence presented above, the steeper 2025 sensitivity relationship suggests that groundwater sampled during the 2025 field campaign may contain a slightly greater contribution from geochemically evolved groundwater sources along longer regional flowpaths and potentially variability in water rock interactions. Therefore, the increased slope likely reflects minor changes in groundwater mixing proportions and groundwater evolution rather than a fundamental modification of regional groundwater flow dynamics.

The age-tracer and stable-isotope datasets provide additional support for this interpretation. Both ME007 and ME050 are characterized by relatively young groundwater and are located immediately adjacent to PACES-defined recharge zones. Therefore, these wells are expected to respond rapidly to changes in local groundwater withdrawals and associated changes in the relative contributions of shallow and deeper groundwater. One possible explanation for the lower proportion of young groundwater observed in 2025 is localized over-abstraction near these wells. Increased groundwater withdrawal could lower local hydraulic heads and allow for a greater contribution of deeper, older groundwater to the open boreholes, thereby changing the mixture sampled at the wells. The substantial differences observed in measured ^{14}C and tritium concentrations between the 2010 and 2025 sampling campaigns are therefore consistent with a reduction in the contribution of recently recharged groundwater and an increased contribution of older groundwater, potentially caused by localized pumping.

The major-ion results provide supporting, although not conclusive, evidence for this interpretation. At ME007, HCO_3^- concentrations increased from 85.0 mg/L in 2010 to 187.2 mg/L in 2025, while alkalinity increased from 76.8 to 153.3 mg/L as $CaCO_3$. These increases

indicate that the groundwater sampled in 2025 was more mineralized and may have undergone more extensive water–rock interaction than the groundwater sampled in 2010, which is consistent with a greater contribution of deeper or longer-residence-time groundwater. Similarly, ME050 exhibits measurable changes in pH, dissolved inorganic carbon, and carbonate-system parameters between the two sampling campaigns (Tables 11 and 12), suggesting a change in groundwater source or mixing proportions. However, these hydrochemical changes are not unique indicators of pumping-induced upcoming because they may also reflect carbonate dissolution, local recharge conditions, well operation, or natural variability.

Meteorological records from the Granby and Saint-Germain-de-Grantham stations indicate lower cumulative June–September precipitation totals in 2025 than in 2010. At Granby, the station selected to represent conditions near ME007, cumulative June–September precipitation decreased from approximately 555.8 mm in 2010 to 295.0 mm in 2025 (Environment and Climate Change Canada [ECCC], 2025). Similarly, at Saint-Germain-de-Grantham, the station selected to represent conditions near ME050, precipitation decreased from approximately 394.8 mm in 2010 to 284.5 mm in 2025 (ECCC, 2025). Although reduced precipitation may have limited the availability of recent recharge, the available data do not establish it as the primary cause of the observed tracer changes. Instead, reduced recharge combined with localized groundwater abstraction could have increased the relative contribution of deeper groundwater to these wells.

Overall, the combined age-tracer, stable-isotope, and major-ion results indicate a potentially substantive change in the groundwater mixtures sampled at ME007 and ME050 between 2010 and 2025. However, the changes observed among the resampled wells were localized and site-specific, with no consistent evidence of a region-wide shift in groundwater age-tracer conditions. Additional information on pumping rates, well-use histories, hydraulic-head changes, well construction, and repeated seasonal sampling would be required to determine whether localized over-abstraction caused the increased contribution of older groundwater.

5.4 River Influence

ME175, ME195, and ME031 were evaluated separately from the broader dataset because their proximity to major surface-water features may result in localized groundwater–river interactions that are not fully represented by the regional model. ME175 and ME195 are located approximately 256 m and 104 m from a river, respectively. ME031 is also situated near a river and close to the brackish groundwater zone delineated by Beaudry et al. (2018), although it was not classified as belonging to the CS hydrochemical group. These wells were therefore excluded from the principal model-evaluation regressions and treated as local hydrogeological exceptions (Figure 16; Table 4).

The age-tracer results provide the clearest evidence of localised modern-water contributions. Between 2010 and 2025, raw ^{14}C activity increased from 47.6 to 82.53 pMC at ME175 and from 39.0 to 68.77 pMC at ME195, whereas most other resampled wells showed decreases (Table 13). Tritium at ME175 remained relatively stable, decreasing only from 7.3 to 6.96 ± 0.34 TU, despite a model prediction of 0 TU. At ME195, ^{3}H increased from 2.6 to 5.84 ± 0.33 TU. These observations indicate greater contributions of modern (ground)water than represented by the regional simulation (Table 12).

Hydrochemical changes also suggest site-specific mixing. At ME195, Ca^{2+}, Mg^{2+}, and HCO_3^- increased, while Na^+ and Cl^- decreased, producing a shift toward the fresher Ca–Mg–HCO_3 facies represented by the river samples (Figure 19; Tables 7–8). ME175 remained Na-rich and became depleted in Ca^{2+} and Mg, while Cl^- and SO_4^{2-} increased, indicating a more complex influence involving modern-water input, ion exchange, and its brackish-influenced M2 setting. At ME031, decreases in Cl^-, HCO_3^-, and alkalinity, together with an increase in pH, indicate localized dilution or mixing, although evidence for any direct river infiltration cannot be presently confirmed (Tables 8 and 10).

However, despite these observed trends, the stable isotope data indicates that river water was not the dominant component at ME175 or ME195 during the 2025 campaign. Both wells remained within the main groundwater cluster near the Basses-Laurentides Meteoric Water Line, whereas the river samples were considerably more isotopically enriched and had lower d-excess values (Figure 17; Table 5). Nevertheless, smaller river-water contributions may vary seasonally or between years in response to river stage, precipitation, recharge, and hydraulic gradients. The observed differences are therefore most consistent with variable localized mixing, bank infiltration, or enhanced modern recharge near river corridors. These

temporally variable, sub-grid-scale processes are not explicitly resolved by the regional 250 m model, justifying the separate treatment of these wells.

5.5 Overall underestimation of the CS group

The selected wells show substantial underestimation of raw measured ^{14}C activities, particularly for the CS hydrochemical water group (Supplementary Material 9, Table 22). The CS group is strongly associated with brackish groundwater influenced by Champlain Sea marine water and is commonly overlain by thick Champlain Sea clay deposits. These conditions likely produce a distinct baseline hydrochemical and isotopic signal that is not fully represented in the present MT3D-USGS transport model. As a result, the model predicts very low ^{14}C activities for several CS wells, while the measured values remain higher (Supplementary Material 9, Table 22). This mismatch may also reflect limitations in the recharge-boundary representation. The PACES-defined main recharge zones were mapped at a regional scale and include limited recharge zones within the CS area; therefore, small-scale local recharge or river influence may not be captured. Because recharge zones were generalized over relatively large areas, localized inputs of younger water near rivers or small recharge windows through the Champlain Sea clay may be missed by the model. The underestimation of ^{14}C in ME081, ME200, ME205, and ME175 therefore likely reflects a combination of unresolved brackish Champlain Sea groundwater effects, limited representation of local recharge, and possible small-scale surface-water influence not captured by the regional model framework (Supplementary Material 9, Table 22).

5.6 Model Limitations and Simplifications

The numerical modelling framework developed in this study was intended to reproduce first-order regional scale groundwater-flow and age-tracer patterns across the approximately 9,218 km² Montérégie Est study area. It was not designed to reproduce fracture-scale groundwater flow or site-specific conditions at individual wells. Therefore, the model necessarily simplifies the spatial variability of hydraulic properties, aquifer geometry, recharge, groundwater–surface-water exchanges, and solute-transport processes. Regional groundwater models are inherently affected by such simplifications because hydrogeological observations are generally much less spatially detailed than the numerical grid used to represent the aquifer system (Gagné et al., 2018). The simplifications and limitations described below should therefore be considered when interpreting simulated hydraulic heads, flowpaths, and ^{3}H and ^{14}C distributions.

Flow Model Simplifications:

5.6.1 Fractured Bedrock Layer Geometry

The depth of the hydraulically active fractured bedrock zone is not well constrained throughout the Montérégie Est region. In the absence of a continuous regional dataset defining the base of active groundwater circulation, the bottom of the upper fractured bedrock layer was generally assigned as 100 m. This assumed 100 m thickness was based on the general interpretation that most active groundwater circulation in regional fractured bedrock aquifers occurs within the shallow fractured zone (Laurencelle,2018). However, the true thickness of hydraulically active bedrock likely varies across the study area according to lithology, fracture density, structural setting, topography, and weathering history.

In locations where the initial hydraulic-head surface fell below the elevation calculated as Bedrock_Surface − 100 m, the upper-aquifer bottom was instead assigned as Initial_Head − 10 m. This adjustment prevented the layer bottom from occurring above the initial saturated groundwater level and reduced numerical drying and convergence problems. Nevertheless, this represents a numerical correction rather than an independently measured geological boundary. Simulated transmissivity, vertical gradients, groundwater storage volume, and residence time may therefore be sensitive to the assumed layer thickness.

The use of one upper fractured bedrock layer also prevents the model from resolving separate shallow and deeper flow systems within that interval. Groundwater circulation occurring in shallow weathered fractures, deeper bedding-plane fractures, and localized

structural features is represented by a single vertically averaged hydraulic response.

5.6.2 Hydraulic Conductivity Assumptions

Hydraulic conductivity within the fractured bedrock aquifer was assigned using the ranges reported by the PACES project for the different hydrogeological contexts of the Montérégie Est region. A single representative average hydraulic conductivity was assigned within each hydrogeological context. This regional parameterization assumes that the average hydraulic properties of each context provide an appropriate first-order representation of groundwater flow at the model scale, although substantial local variability may occur within individual geological units and fracture networks.

Horizontal hydraulic conductivity was assumed to be isotropic based on Equation 21:

$$K_x = K_y \quad (21)$$

Vertical hydraulic conductivity was assigned as Equation 11.

This vertical anisotropy was used to represent lower vertical fracture connectivity relative to horizontal groundwater flow. However, use of a single anisotropy ratio throughout the model inevitably cannot reproduce local and site-specific variations in fracture orientation, aperture, connectivity, as well as broader lithologic or structural heterogeneities such as bedding-planes, fractures, or faults which may have a preferred plane, all of which may result in observable anisotropy in conductivity which was not be factored in by this model. Vertical and horizontal groundwater velocities may therefore differ locally from those predicted by the regional model.

Hydraulic conductivity in the fractured bedrock aquifer was also assumed to decrease exponentially with depth because of the regional reduction in the density and aperture of hydraulically active fractures. Because the fractured bedrock aquifer was represented as a single numerical layer, this vertical decrease could not be represented as a continuous gradient. Instead, the PACES-derived surface hydraulic-conductivity values were multiplied by a depth-decay factor in Equation 22:

$$K_x = K_y = 0.135335283236613 * K_{average} \quad (22)$$

This depth corresponds approximately to the midpoint of an aquifer layer extending 100 m below the bedrock surface.

This treatment provides an effective layer-scale hydraulic conductivity that accounts for the general decrease in fracture permeability with depth. However, it averages the more permeable shallow fractures and less permeable deeper bedrock into one representative value. The model therefore cannot reproduce continuous vertical changes in hydraulic conductivity (or smaller scale variability of this within a region) or preferential groundwater flow through individual fractures and structural features. The treatment of using average K for each hydrogeological zones therefore can also result in local flow dynamics being overlooked.

5.6.3 Recharge Simplifications:

Groundwater recharge was represented using the spatially distributed SWAT-derived recharge dataset developed for the Montérégie Est region through the PACES project. This dataset estimates the net recharge reaching the fractured bedrock aquifer after accounting for regional surface-water-balance processes. It was therefore applied directly to the upper fractured bedrock layer as bedrock recharge rather than being treated as precipitation or infiltration entering at the ground surface.

Although the SWAT-derived layer provides a spatially distributed and regionally consistent estimate of bedrock recharge, it remains subject to uncertainty associated with the input climate data, soil and land-use classifications, surface-runoff calculations, evapotranspiration estimates, model calibration, and spatial discretization used in the original SWAT analysis. Local recharge processes occurring at scales smaller than the SWAT grid may consequently be smoothed or omitted. These processes may include focused recharge through bedrock outcrops, permeable sediment windows, fractures, depressions, and discontinuities within otherwise low-permeability surficial deposits.

The recharge dataset represents long-term average conditions and was applied under a steady-state groundwater-flow formulation. The model therefore does not reproduce seasonal snowmelt recharge, individual precipitation events, drought periods, interannual climate variability, or potential changes in recharge between the 2010 and 2025 sampling campaigns. These temporal processes are important in southern Québec, where recharge is strongly seasonal, commonly peaks during spring snowmelt, and varies between years in response to precipitation and temperature conditions (Dubois et al., 2021, 2022). Simulated recharge should consequently be interpreted as an effective regional average rather than the recharge rate occurring at a particular location and time.

Application of the unmodified SWAT recharge layer produced abrupt changes in simulated hydraulic heads that were inconsistent with the regional piezometric pattern. The recharge values were therefore multiplied by the same depth-scaling factor used to represent the effective decrease in hydraulic conductivity within the fractured bedrock layer. This adjustment improved agreement between simulated and regional hydraulic heads. However, hydraulic conductivity and recharge are separate physical parameters, and scaling both using the same factor is an empirical regional simplification rather than a direct representation of recharge processes. This treatment may introduce parameter compensation or model non-uniqueness; whereby different combinations of hydraulic conductivity and recharge could reproduce similar regional head distributions.

Uncertainty in the magnitude and spatial distribution of bedrock recharge propagates into simulated hydraulic gradients, groundwater velocities, flowpath lengths, and residence-time distributions. The SWAT recharge layer should therefore be regarded as the best available regional estimate of bedrock recharge, while recognizing that local recharge rates and pathways may differ from the values represented at the model-grid scale.

5.6.4 Drain Package and Groundwater-Discharge Representation

Regional groundwater-discharge areas were identified primarily from the PACES hydrogeological framework. As spatially distributed measurements of groundwater discharge, streambed properties, and groundwater–surface-water exchange was not available across the model domain, groundwater discharge was represented using the MODFLOW Drain (DRN) Package. Here drain elevations were assigned assuming groundwater discharge occurs where simulated hydraulic heads rise above the local land-surface elevation which allows the model to represent seepage and discharge toward topographically low areas, streams, wetlands, and other potential groundwater-discharge locations. However, it is acknowledged that this may be an oversimplification and actual stream stages, wetland elevations, channel incision, and local discharge elevations may differ from the model-top surface.

The use of Model_Top as the drain elevation may also produce uncertainty where the true discharge feature is incised below the land surface. In these locations, the model may require hydraulic heads to rise higher than the actual river or wetland stage before discharge occurs. Combined with the 250 m grid resolution, this simplification may moderately affect simulated groundwater heads, discharge rates, and flowpath termination near small streams, wetlands, and localized springs.

5.6.5 Hydraulic-Head Constraint and Model Non-Uniqueness

Simulated hydraulic heads were compared with hydraulic-head values extracted at 25 observation locations from the PACES regional piezometric surface. These points provide a constraint on the first-order regional hydraulic gradient, but their density is limited relative to the approximately 9,218 km² model domain. In addition, values extracted from an interpolated piezometric surface are not equivalent to a dense set of independent, contemporaneous groundwater-level measurements.

The hydraulic-head comparison therefore provides stronger support for the regional pattern of flow than for local hydraulic conditions. Local residuals may reflect interpolation uncertainty in the PACES piezometric surface, differences in the timing of groundwater-level measurements, unresolved pumping effects, or fracture-scale heterogeneity. The limited number of head-comparison points also increases the possibility of variability between the model and in situ conditions as multiple combinations of hydraulic conductivity, recharge, anisotropy, and drain conductance may reproduce a similar regional head distribution used to generate the model as highlighted by previous studies (Gagné et al., 2018).

For this reason, hydraulic heads were not used as the only measure of model performance. Simulated results were also evaluated using MODPATH flowpaths, ^{3}H and ^{14}C distributions, major-ion chemistry, stable isotopes, and the conceptual groundwater-flow framework developed by Beaudry et al. (2018).

5.7 Transport Model Simplifications and Limitations

5.7.1 Uniform Dispersivity

The MT3D-USGS transport models used a spatially uniform longitudinal dispersivity and fixed transverse horizontal and vertical dispersivity ratios throughout the model domain. The adopted longitudinal dispersivity represents an effective regional scale macrodispersivity intended to account for unresolved spreading caused by heterogeneity below the 250 m grid scale.

In reality, dispersivity is not spatially uniform and is dependent on transport distance, lithology, fracture aperture, fracture orientation, hydraulic gradient, groundwater velocity, and the degree of fracture connectivity. The use of a single dispersivity value may therefore overestimate mixing in some parts of the aquifer and underestimate it in others. A large effective dispersivity may smooth sharp tracer gradients and produce excessive numerical spreading, whereas a value that is too low may fail to represent mixing between adjacent groundwater flowpaths. The modelled ^{3}H and ^{14}C distributions should consequently be interpreted as regional average tracer patterns rather than predictions of specific fracture-scale concentration variability.

5.7.2 Vertical Mixing and Groundwater Sampling Depth Limitations

MT3D-USGS tracer values were extracted from the fractured bedrock model layer at the grid cells corresponding to sampled wells. Each predicted value therefore represents the simulated concentration within the numerical layer rather than a concentration calculated for an exact well-screen or fracture depth.

In the physical aquifer, groundwater chemistry and age-tracer concentrations may vary considerably with depth. Shallow fractures may contain recently recharged groundwater with relatively high ^{3}H and ^{14}C activities, whereas deeper or poorly connected fractures may contain older groundwater with lower tracer activities. A single numerical layer cannot resolve this vertical variability within the upper fractured bedrock aquifer.

The 2010 and 2025 groundwater samples were collected at the wellhead rather than from isolated depth intervals. During pumping, water may enter a well from several water-producing fractures located at different depths. The measured sample therefore represents a volume-weighted mixture of groundwater from the net contributing connected fractures intercepted by the well, rather than groundwater from one precisely defined depth. The relative contribution from each fracture depends on fracture transmissivity, the open interval of the

well, pumping rate, pumping duration, and vertical hydraulic gradients. As a result, the measured wellhead concentration is not directly equivalent to either a concentration at one model elevation or a simple arithmetic average of the entire fractured bedrock layer being sampled by the well. Discrepancies at individual wells may result from unresolved vertical mixing and borehole hydraulics rather than solely from errors in simulated regional groundwater transport. This observation is especially important where both young and old groundwater components occur in the same well. Gagné et al. (2018), Meyzonnat et al. (2023) and others have shown that isotope-derived groundwater ages in regional fractured bedrock systems may represent mixtures of recent recharge and older groundwater rather than one discrete groundwater travel time. The authors therefore recommended cautious, primarily conceptual interpretation of comparisons between simulated travel times and isotope-derived mean residence times. As a result, agreement between simulated and measured concentrations, such as those presented here, should therefore be interpreted at the regional scale to accommodate this local variability in fracture input at the well scale.

5.7.3 Lack of Dual-Domain Mass Transfer

The fractured-bedrock aquifer was represented as a single mobile continuum. Although molecular diffusion was included through the MT3D-USGS dispersion formulation, this process operated only within the simulated mobile domain. The model did not explicitly distinguish rapidly flowing fracture water from relatively immobile pore water within the surrounding rock matrix and therefore did not include a dual-domain mass-transfer formulation for exchange between these domains. In natural fractured-bedrock aquifers, concentration gradients may drive solutes and groundwater-age tracers from flowing fractures into the adjacent rock matrix. These tracers may later diffuse back into the fractures as fracture-water concentrations change. Such fracture–matrix exchange can temporarily store tracer mass, broaden groundwater travel-time distributions, and produce prolonged concentration tails. Mixing between older matrix water and younger fracture water may also generate tracer concentrations that cannot be reproduced solely through advection, dispersion, and molecular diffusion within a single mobile continuum (Meyzonnat et al., 2023).

The absence of explicit fracture–matrix mass transfer may therefore cause the model to underestimate tracer retention, delayed release, and mixing between mobile and relatively immobile groundwater domains. Consequently, simulated tracer concentrations may respond too directly to the advective groundwater-flow field and may exhibit narrower residence-time

distributions than those occurring in the natural aquifer. This limitation may be particularly important along long regional flowpaths and within confined areas, where longer residence times provide greater opportunity for diffusion and exchange between fractures and the surrounding rock matrix.

5.7.4 Simplified Representation of Tracer Recharge Zones

For the model developed here the recharge rates used by MODFLOW and the tracer-source areas used by MT3D-USGS represent two separate model inputs. Bedrock recharge rates were obtained from the spatially distributed SWAT-derived recharge layer, whereas ^{3}H and ^{14}C concentrations were introduced through the MT3D-USGS Source-Sink Mixing Package within the major fractured bedrock recharge zones identified by the PACES project. The PACES-defined major recharge zones are regional features, covering areas greater than approximately 1 km² (Carrier et al., 2013). They were therefore suitable for representing the principal locations at which tracer-bearing recharge enters the fractured bedrock aquifer at the regional scale. However, their spatial extent and resolution may not capture variability such as smaller recharge areas, localized bedrock outcrops, individual fracture-controlled recharge pathways, permeable sediment windows, or focused recharge associated with streams and topographic depressions.

Additionally, in this study, tracer concentrations were assigned uniformly within each defined recharge object according to the applicable model scenario. For example, a uniform concentration of 14 TU was assigned within the principal recharge zones for the ^{3}H model, whereas effective ^{14}C activities were assigned according to confinement conditions, hydrochemical water groups, and sensitivity-test results. This approach does not represent any temporal or spatial variability in recharge chemistry or tracer concentration. It also creates relatively distinct boundaries between cells receiving an assigned tracer concentration and adjacent cells receiving no tracer source or a different concentration. Therefore, the transport model may omit small or spatially diffuse sources of modern tracer-bearing recharge and may overestimate tracer inputs within the mapped major recharge zones. Simulated ^{3}H and ^{14}C distributions should therefore be interpreted as responses to the dominant regional recharge framework rather than as complete representations of every local recharge pathway. Discrepancies at individual wells, particularly near small streams, sediment windows, or localized fractured outcrops, may reflect recharge features that are not resolved by the PACES recharge-zone polygons or the 250 m model grid.

5.7.5 Simplified Radiocarbon Geochemistry

Here, radiocarbon was simulated as a dissolved tracer undergoing advection, dispersion, and first-order radioactive decay. Geochemical reactions affecting dissolved inorganic carbon were not explicitly simulated along groundwater flowpaths. However, per the introduction, processes such as carbonate dissolution and precipitation, oxidation of organic matter, methanogenesis, sulfate reduction, isotopic exchange, and mixing with brackish or radiocarbon-dead groundwater may modify ^{14}C activities independently of radioactive decay. The final ^{14}C model represented these processes indirectly by assigning effective recharge concentrations of 0, 35, or 100 pMC to selected recharge cells according to confinement conditions, hydrochemical water groups, and sensitivity-test results on the assumption that the majority of dead carbon addition occurred near to, or at, the recharge zone. However, this simplification cannot account for continued carbon reactions along the subsequent groundwater flowpath. Simulated ^{14}C activities in this model therefore only approximate the combined effects of the assigned initial activity, groundwater transport, mixing represented by the dispersion formulation, and radioactive decay, rather than a complete reactive-transport simulation of the carbon system.

5.7.6 Constant Tracer Inputs and Steady-State Conditions

The ^{3}H model used a constant recharge concentration of 14 TU, derived from groundwater sampled near major recharge areas during the 2010 PACES campaign. The model does not reproduce the historical atmospheric tritium input curve, seasonal precipitation variability, or changes in recharge tritium between 2010 and 2025. Similarly, the ^{14}C model applies time-independent recharge-zone activities.

The agreement of the 14 TU simulation with both the 2010 and 2025 observations suggests that the regional distribution is strongly controlled by groundwater flow pathways, mixing, and radioactive decay. Nevertheless, the constant input prevents the model in its current iteration from distinguishing among waters recharged during different atmospheric-input periods. Predicted tritium concentrations should therefore be interpreted as effective indicators of regional groundwater renewal and relative residence time rather than exact reconstructions incorporating variability in the input.

More broadly, the steady-state groundwater-flow formulation assumes that hydraulic gradients and regional flow directions remain constant through time. It does not reproduce historical changes associated with deglaciation, the Champlain Sea invasion and retreat,

climatic variability, groundwater abstraction, or changes in land use. Old groundwater retained beneath confined areas may therefore contain inherited paleo-recharge and geochemical signals that cannot be fully reproduced by a steady-state regional transport model. Gagné et al. (2018) similarly noted that representing mixtures of recent recharge and old groundwater within a steady-state regional model is difficult and that isotope-derived ages should be used cautiously as conceptual validation targets rather than exact equivalents of simulated travel time.

Chapter 6. Conclusions

6.1 Summary of Major Findings

This study developed a coupled regional groundwater-flow and age-tracer modelling framework for the ~9,218 km² Montérégie Est fractured-bedrock aquifer system. MODFLOW-NWT was used to simulate hydraulic heads, MODPATH 7 was used to investigate groundwater flowpaths, and MT3D-USGS was used to simulate the transport, mixing, and radioactive decay of tritium (^{3}H) and radiocarbon (^{14}C). The modelling framework integrated data from the 2010 PACES campaign with stable-isotope, hydrochemical, and age-tracer data collected during the 2025 field campaign. This allowed a quantitative, ground-truthed hydrogeologic model to be proposed for the region where only a conceptual model had been previously proposed.

The simulated hydraulic-head distribution accurately reproduced the first-order regional hydraulic gradients, with $R^2 = 0.981$, an RMSE of 12.57 m, and a near-zero mean bias. Higher heads were simulated in the Appalachian Uplands and other topographic highs, followed by decreasing heads toward the Appalachian Piedmont and St. Lawrence Lowlands. The MODPATH results identified shorter local flow systems in the Appalachian Uplands and longer regional flowpaths extending toward the Lowlands, major rivers, and regional discharge areas. These patterns broadly agreed with the regional groundwater-flow conceptual model proposed by Beaudry et al. (2018).

The age-tracer simulations provided an independent evaluation of the groundwater-flow framework. The model reproduced the main spatial variations in ^{3}H and raw ^{14}C within the 2010 calibration dataset. Predictions produced using the 2010-calibrated model were subsequently compared with newly collected 2025 observations. For the independent 2025 model-evaluation dataset, the ^{3}H comparison produced $R^2 = 0.866$ and an RMSE of 2.378 TU, while the raw ^{14}C comparison produced $R^2 = 0.984$ and an RMSE of 3.316 pMC. When the 2010 and 2025 datasets were combined, the regression slopes for both tracers were close to one. These results indicate that the model also accurately reproduced the broad regional distribution of modern and older groundwater beyond the original calibration dataset, although localized deviations remained.

Stable-isotope and major-ion results provided additional support for the interpretation of recharge, mixing, and groundwater evolution. Most groundwater samples plotted near the Basses-Laurentides Meteoric Water Line, indicating predominantly meteoric recharge under broadly similar climatic conditions. Hydrochemical compositions ranged from relatively fresh Ca–Mg–HCO_3 groundwater to chemically evolved Na-rich groundwater, consistent with

carbonate dissolution, ion exchange, mixing, and increasing water–rock interaction along groundwater flowpaths.

Temporal comparisons between the 2010 and 2025 campaigns showed that groundwater conditions did not change uniformly throughout the study area. Tritium decreased at four of the six resampled wells. Raw ^{14}C decreased substantially at ME007, ME050, and ME063, while ME122 remained approximately stable. In contrast, ME175 and ME195 showed increases in raw ^{14}C, together with evidence of changing modern-water contributions. These site-specific changes likely reflect variations in recharge, groundwater–river interaction, bank infiltration, and groundwater mixing rather than a uniform regional shift.

6.2 Limitations and Future Work

The key limitations and simplifications of specific aspects of the modelling approach are outlined in detail in Section 5.6 and 5.7. From here, the overall limitations are identified with potential avenues to address these are as follows.

Firstly, is the potential for partial overfitting to the prescribed recharge-boundary conditions. Several 2010 calibration wells are located within or immediately adjacent to PACES-defined main recharge zones, where relatively high ^{3}H and ^{14}C concentrations were assigned directly as model inputs. Consequently, close agreement at some recharge-proximal wells partly reflects the imposed boundary concentrations rather than an entirely independent simulation of tracer evolution along groundwater flowpaths. This is particularly relevant for wells predicted at or near the assigned recharge concentrations, including the clustering of some ^{3}H predictions near 14 TU and ^{14}C predictions near 100 pMC. The high regression coefficients should therefore be interpreted together with RMSE, residual patterns, recharge-zone distance, and performance at wells located farther downgradient. The comparison with the independently collected 2025 data provides a stronger test of model transferability, although some 2025 wells are also located close to mapped recharge areas and may remain sensitive to the same boundary assumptions.

Additionally, the spatial resolution and generalization of the recharge representation constitute an additional significant limitation. The tracer-boundary conditions were based on relatively large PACES-defined main recharge zones, several of which cover areas greater than 1 km^2. These polygons provide a reasonable regional approximation but cannot represent smaller recharge features, spatial variability within individual recharge areas, or recharge occurring outside the mapped zones. Assigning one tracer concentration across a large polygon may create abrupt boundaries and may not reproduce gradual spatial variations in recharge age, infiltration rate, soil-zone carbon inputs, or atmospheric tracer concentrations. Future work should therefore develop a continuous, higher-resolution recharge map incorporating surficial geology, soil permeability, land cover, topography, precipitation, evapotranspiration, snowmelt, and streamflow data. Seasonal or monthly recharge estimates would also support a transient model and improve the representation of temporally variable tracer inputs.

Another highlighted limitation was that the regional model also does not fully represent localized hydrogeological variability. The 250 m grid and equivalent-porous-medium approach are appropriate for examining first-order regional groundwater flow but cannot explicitly resolve individual fractures, small faults, narrow sediment-filled valleys, localized recharge

pathways, or groundwater–river connections occurring at scales smaller than a model cell. Therefore, the simulated flowlines represent generalized advective pathways through the regional equivalent porous medium rather than the exact trajectories followed by groundwater through individual fractures. The model is most reliable for interpreting intermediate and regional flow systems, whereas short local flowlines may be simplified, merged with longer pathways, or omitted because their controlling features occur below the model resolution. The classification of individual flowlines as local, intermediate, or regional should therefore be interpreted according to their relative travel distances, depths, and durations within the regional model rather than as precise delineations of natural flow systems. Such sub-grid variability may explain anomalous results at individual wells and the observed differences between the 2010 and 2025 campaigns. The model should consequently be interpreted as a regional representation rather than a precise predictor of tracer concentrations, hydraulic conditions, or exact groundwater-flow pathways at individual wells.

A more detailed three-dimensional representation of surficial sediments would improve the model's ability to reproduce this local variability. The current framework does not fully resolve the vertical and lateral distributions of till, marine clay, silt, sand, gravel, and buried-valley deposits. These units may strongly control recharge, aquifer confinement, vertical leakage, shallow flow, and groundwater discharge to rivers. Future models could incorporate borehole logs, geological cross-sections, geophysical surveys, and piezocone data to distinguish permeable granular units from low-permeability clay and till layers. Representing these deposits as separate model layers would improve simulations of localized recharge and hydraulic connections between surface water, shallow sediments, and the fractured-bedrock aquifer.

Another model simplification was that hydraulic conductivity was represented using regional datasets and simplified assumptions regarding depth decay and anisotropy. In reality, K within fractured bedrock may vary by several orders of magnitude over short distances because of variations in fracture density, aperture, connectivity, lithology, weathering, and structural features. Spatially averaged values may reproduce the regional hydraulic-head distribution while failing to represent localized velocities and preferential flowpaths. Additional pumping tests, slug tests, borehole-flow measurements, packer tests, fracture logs, and structural mapping would allow spatial variations in K, vertical anisotropy, faults, and preferential fracture zones to be represented more realistically. Locally refined or nested models around river corridors, recharge zones, and anomalous wells could improve the

simulation of localized flow without requiring uniformly fine resolution across the complete regional model domain.

Another model limitation is the dependence on a relatively limited dataset to identify temporal trends. To address this, a future field campaign should attempt to resample as many of the original 2010 age-tracer wells as possible. The relatively small number of paired wells limits the ability to separate regional temporal trends from well-specific changes. A larger paired dataset would provide a stronger evaluation of whether tracer concentrations have changed consistently across hydrochemical groups, recharge settings, and flowpath positions. Repeated sampling during different seasons would also help determine whether observed differences reflect long-term changes or seasonal variations in river stage, recharge, pumping, and groundwater-mixing proportions. Depth-discrete or packer-isolated sampling would further reduce uncertainty associated with open wells that may combine groundwater from fractures having different depths, transmissivities, and residence times.

Further work could include transient groundwater-flow and transport simulations, time-varying atmospheric ^{3}H and ^{14}C inputs, improved river stages and streambed conductance, and explicit simulation of pumping. Reactive transport modelling of carbonate dissolution, DIC evolution, and dead-carbon addition would provide a more physically based representation of ^{14}C than assigning reduced concentrations only at recharge boundaries. Additional measurements of $\delta^{13}C$-DIC, DIC, CFCs, SF_6, ^{85}Kr, dissolved gases, and noble-gas recharge temperatures could further constrain groundwater mixing and residence-time distributions.

Finally, formal parameter-estimation and uncertainty analyses should be undertaken. PEST, Monte Carlo simulations, sensitivity analysis, and comparison of alternative conceptual models could quantify parameter non-uniqueness and evaluate whether similarly good fits can be produced using different combinations of recharge, hydraulic conductivity, porosity, dispersivity, river conductance, and tracer-boundary concentrations. Cross-validation, in which selected wells are withheld from calibration and used only for evaluation, would provide a particularly useful test of potential overfitting. These analyses would help distinguish model agreement caused by imposed calibration conditions from agreement arising from an accurate representation of regional groundwater flow and transport.

6.3 Implications for Groundwater Resource Management

The model identifies important differences in groundwater renewal and flow across Montérégie Est. Recharge area. Firstly, the Appalachian Uplands, northern Piedmont, and portions of the Southern St. Lawrence Lowlands supply relatively young groundwater and should therefore be prioritized for land-use planning and protection from surface-derived contamination. Meanwhile, groundwater along longer regional flowpaths and beneath confined portions of the Lowlands generally has longer residence times and is renewed more slowly, making these resources potentially more sensitive to sustained pumping and long-term changes in recharge.

The results also show that groundwater quality may be influenced by mixing between fresh groundwater, evolved Na-rich groundwater, and remaining brackish groundwater, particularly near the transition into the Northern St. Lawrence Lowlands. Continued monitoring of major ions, stable isotope, and age tracers would further identify changes in these mixing zones. Additionally, as highlighted in this study, groundwater–river interaction near selected wells further indicates that surface-water and groundwater resources should be managed as connected systems. Overall, the model provides a regional screening tool for identifying recharge areas, regional flowpaths, slowly renewed groundwater, and locations requiring additional monitoring, but site-specific management decisions should be supported by higher-resolution local investigations.

6.4 Potential Contributions of Regional Age Tracer Groundwater Model

In closing, the potential contributions of a regional groundwater age-tracer model, such as the model developed in this study, are as follows:

- The results demonstrate that a regional equivalent porous medium (EPM) model can reproduce the principal spatial patterns of raw groundwater age-tracer activities in a fractured-bedrock aquifer. Although individual fractures are not represented explicitly, the model captures the broad regional flow system and provides a practical framework for interpreting the distribution of recently recharged and older groundwater.
- The simulated flow paths and age-tracer distributions identify areas of relatively active groundwater circulation. Because groundwater is an important drinking-water resource in Montérégie Est, these results may support regional land-use and industrial planning by helping identify areas where contaminants could migrate more rapidly along active flow paths. However, site-specific investigations would still be required to assess contamination risks at the local scale.
- Previous investigations in Montérégie Est used hydrochemistry and groundwater-age tracers—including ^{3}H, ^{14}C, $^{3}H/^{3}He$, and helium isotopes—to distinguish recently recharged groundwater from older groundwater under confined conditions and to develop conceptual interpretations of regional groundwater flow (Carrier et al., 2013; Beaudry et al., 2018; Pinti et al., 2022). Laurencelle (2018) also investigated the hydraulic properties and palaeohydrogeological evolution of the regional fractured-bedrock aquifer. The present study builds upon this work by integrating hydrochemistry, ^{3}H, and ^{14}C observations into a regional numerical flow-and-transport model for Montérégie Est, thereby providing a quantitative framework for characterizing groundwater-flow regimes, tracer distributions, and flow rates.
- Previous regional studies compared multilayer groundwater-flow models with tracer-derived residence times or MODPATH particle-tracking travel times (Reilly et al., 1994; Sanford et al., 2004; Gagné et al., 2018). In southern Québec, Gagné et al. (2018) found that MODPATH reproduced younger $^{3}H/^{3}He$ residence times more successfully than older ^{14}C residence times, partly because of groundwater mixing and limitations in representing long regional flow paths. The present study extends these approaches by using MT3D-USGS to simulate ^{14}C radioactive decay together with advective–dispersive transport and mixing in the fractured-bedrock aquifer. The

satisfactory agreement between simulated and measured tracer activities demonstrates the value of directly simulating age-tracer transport rather than relying solely on advective particle-tracking times (Zhu, 2000; Gusyev et al., 2013, 2014).

References

ABB Measurement & Analytics. (2017). *Triple isotopic water analyzer: Instruction manual*. ABB/Los Gatos Research.

Agilent Technologies. (2016). *Agilent 5100 and 5110 ICP-OES user's guide* (Publication No. G8010-90002). Agilent Technologies.

Agrawal, R. K., Mohanty, R. K., Rathi, A., Mehta, S., Yadava, M. G., Kumar, S., & Laskar, A. H. (2024). Estimation of groundwater residence time using radiocarbon and stable isotope ratio in dissolved inorganic carbon and soil CO_2. *Radiocarbon, 66*(2), 249–266. https://doi.org/10.1017/RDC.2024.43

Alecsa, C. D., Boros, I., Frank, F., Knabner, P., Nechita, M., Prechtel, A., Rupp, A., & Suciu, N. (2020). Numerical benchmark study for flow in highly heterogeneous aquifers. *Advances in Water Resources, 138*, 103558. https://doi.org/10.1016/j.advwatres.2020.103558

Appelo, C. A. J., & Postma, D. (2005). *Geochemistry, groundwater and pollution* (2nd ed.). CRC Press/Balkema. https://doi.org/10.1201/9781439833544

Beaudry, C. (2013). *Hydrogéochimie de l'aquifère rocheux régional en Montérégie Est, Québec* [Master's thesis, Université du Québec, Institut national de la recherche scientifique]. EspaceINRS. https://espace.inrs.ca/id/eprint/1363/#

Beaudry, C., Lefebvre, R., Rivard, C., & Cloutier, V. (2018). Conceptual model of regional groundwater flow based on hydrogeochemistry (Montérégie Est, Québec, Canada). *Canadian Water Resources Journal / Revue canadienne des ressources hydriques, 43*(2), 152–172. https://doi.org/10.1080/07011784.2018.1461579

Bedekar, V., Morway, E. D., Langevin, C. D., & Tonkin, M. J. (2016). *MT3D-USGS version 1: A U.S. Geological Survey release of MT3DMS updated with new and expanded transport capabilities for use with MODFLOW* (Techniques and Methods 6-A53). U.S. Geological Survey. https://doi.org/10.3133/tm6A53

Berghuijs, W. R., Collenteur, R. A., Jasechko, S., Jaramillo, F., Luijendijk, E., Moeck, C., van der Velde, Y., & Allen, S. T. (2024). Groundwater recharge is sensitive to changing long-term aridity. *Nature Climate Change, 14*, 357–363. https://doi.org/10.1038/s41558-024-01953-z

Berkowitz, B. (2002). Characterizing flow and transport in fractured geological media: A review. *Advances in Water Resources, 25*(8–12), 861–884. https://doi.org/10.1016/S0309-1708(02)00042-8

Bethke, C. M., & Johnson, T. M. (2008). Groundwater age and groundwater age dating. *Annual Review of Earth and Planetary Sciences, 36*, 121-152. https://doi.org/10.1146/annurev.earth.36.031207.124210

Briggs, M. A., Day-Lewis, F. D., Ong, J. B., Harvey, J. W., & Lane, J. W. (2014). Dual-domain mass-transfer parameters from electrical hysteresis: Theory and analytical approach applied to laboratory, synthetic streambed, and groundwater experiments. *Water Resources Research, 50*(10), 8281-8299. https://doi.org/10.1002/2014WR015880

Capuano, R. M., & Jones, C. R. (2020). Cation exchange in groundwater–chemical evolution and prediction of paleo-groundwater flow: A natural-system study. *Water Resources Research, 56*(8), e2019WR026318. https://doi.org/10.1029/2019WR026318

Carol, E.S., Kruse, E.E., Laurencena, P.C. *et al.* Ionic exchange in groundwater hydrochemical evolution. Study case: the drainage basin of El Pescado creek (Buenos Aires province, Argentina). *Environ Earth Sci* **65**, 421–428 (2012). https://doi.org/10.1007/s12665-011-1318-z

Carrier, M.-A., Lefebvre, R., Rivard, C., Parent, M., Ballard, J.-M., Benoît, N., Vigneault, H., Beaudry, C., Malet, X., Laurencelle, M., Gosselin, J.-S., Ladevèze, P., Thériault, R., Beaudin, I., Michaud, A., Pugin, A. J.-M., Morin, R., Crow, H., Gloaguen, E., . . . Lavoie, D. (2013a). *Atlas hydrogéologique de la Montérégie Est, Québec, Canada* (Rapport de recherche R-1432). Institut national de la recherche scientifique, Centre Eau Terre Environnement. https://espace.inrs.ca/id/eprint/1640/

Carrier, M.-A., Lefebvre, R., Rivard, C., Parent, M., Ballard, J.-M., Benoît, N., Vigneault, H., Beaudry, C., Malet, X., Laurencelle, M., Gosselin, J.-S., Ladevèze, P., Thériault, R., Beaudin, I., Michaud, A., Pugin, A. J.-M., Morin, R., Crow, H., Gloaguen, E., . . . Lavoie, D. (2013). *Portrait des ressources en eau souterraine en Montérégie Est, Québec, Canada* (Rapport de recherche R-1433). Institut national de la recherche scientifique, Centre Eau Terre Environnement. https://www.environnement.gouv.qc.ca/_PACES/rapports-projets/MonteregieEst/MON-scientif-INRS-201306.pdf

Cartwright, I., Currell, M. J., Cendón, D. I., & Meredith, K. T. (2020). A review of the use of radiocarbon to estimate groundwater residence times in semi-arid and arid areas. *Journal of Hydrology, 580*, 124247. https://doi.org/10.1016/j.jhydrol.2019.124247

Chandra, S., Auken, E., Maurya, P. K., Ahmed, S., & Verma, S. K. (2019). Large-scale mapping of fractures and groundwater pathways in crystalline hardrock by AEM. *Scientific Reports, 9*, 398. https://doi.org/10.1038/s41598-018-36153-1

Chromatographic Specialties Inc. (n.d.). *Septa, 22 mm, PTFE/grey butyl, for 24-400 screw cap, 1000/pk* (Part No. 222201) [Product information]. Retrieved July 4, 2026, from https://chromspec.com/

Cickaric, D., Dersek-Timotić, I., Onjia, A., & Rajaković, L. (2005). Development of ion chromatography methods for the determination of trace anions in ultra pure water from power plants. *Journal of the Serbian Chemical Society, 70*(7), 995–1003. https://doi.org/10.2298/JSC0507995C

Clark, I. D. (2015). *Groundwater geochemistry and isotopes*. CRC Press. https://doi.org/10.1201/b18347

Clark, I. D., & Fritz, P. (1997). *Environmental isotopes in hydrogeology*. Lewis Publishers. https://doi.org/10.1201/9781482242911

Cloutier, V. (2004). *Origine et évolution géochimique des eaux souterraines du système aquifère des Basses-Laurentides dans les roches sédimentaires paléozoïques des basses-terres du Saint-Laurent, Québec, Canada* [Doctoral dissertation, Université du Québec, Institut national de la recherche scientifique]. EspaceINRS. https://espace.inrs.ca/id/eprint/1445/

Cloutier, V., Lefebvre, R., Savard, M. M., Bourque, É., & Therrien, R. (2006). Hydrogeochemistry and groundwater origin of the Basses-Laurentides sedimentary rock aquifer system, St. Lawrence Lowlands, Québec, Canada. *Hydrogeology Journal, 14*(4), 573–590. https://doi.org/10.1007/s10040-005-0002-3

Cook, P. G. (2003). *A guide to regional groundwater flow in fractured rock aquifers*. CSIRO Land and Water. https://gw-project.org/books/a-guide-to-regional-groundwater-flow-in-fractured-rock-aquifers/

Cook, P. G., & Herczeg, A. L. (Eds.). (2000). *Environmental tracers in subsurface hydrology*. Kluwer Academic Publishers. https://doi.org/10.1007/978-1-4615-4557-6

Craig, H. (1961). Isotopic variations in meteoric waters. *Science, 133*(3465), 1702–1703. https://doi.org/10.1126/science.133.3465.1702

Dansgaard, W. (1964). Stable isotopes in precipitation. *Tellus, 16*(4), 436–468. https://doi.org/10.1111/j.2153-3490.1964.tb00181.x

DHI. (2025). *Péclet number*. In *FEFLOW 8.1 documentation*. https://download.feflow.com/html/help81/feflow/09_Parameters/Auxiliary_Data/peclet_number.html

Dubois, E., Larocque, M., Gagné, S., & Braun, M. (2022). Climate change impacts on groundwater recharge in cold and humid climates: Controlling processes and thresholds. *Climate, 10*(1), Article 6. https://doi.org/10.3390/cli10010006

Dubois, E., Larocque, M., Gagné, S., & Meyzonnat, G. (2021). Simulation of long-term spatiotemporal variations in regional-scale groundwater recharge: Contributions of a water budget approach in cold and humid climates. *Hydrology and Earth System Sciences, 25*(12), 6567–6589. https://doi.org/10.5194/hess-25-6567-2021

DWK Life Sciences. (n.d.-a). *WHEATON black phenolic closures* [Product page]. Retrieved July 4, 2026, from https://www.dwk.com/na/wheaton-black-phenolic-closures

DWK Life Sciences. (n.d.-b). *WHEATON glass and plastic containers* [Product catalog]. Retrieved July 4, 2026, from https://www.dwk.com/pub/media/mageplaza/resource/pdf/WHEATON-Container-Guide.pdf

Eastoe, C. J., Watts, C. J., Ploughe, M., & Wright, W. E. (2012). Future use of tritium in mapping pre-bomb groundwater volumes. *Ground Water, 50*(1), 87–93. https://doi.org/10.1111/j.1745-6584.2011.00806.x

Environment and Climate Change Canada. (n.d.-a). *Historical climate data: Granby, Quebec* [Data set]. Government of Canada. Retrieved July 4, 2026, from the Historical Climate Data database.

Environment and Climate Change Canada. (n.d.-b). *Historical climate data: Saint-Germain-de-Grantham, Quebec* [Data set]. Government of Canada. Retrieved July 4, 2026, from the Historical Climate Data database.

Epting, J., Michel, A., Affolter, A., & Huggenberger, P. (2021). Climate change effects on groundwater recharge and temperatures in Swiss alluvial aquifers. *Journal of Hydrology X, 11*, 100071. https://doi.org/10.1016/j.hydroa.2020.100071

Fetter, C. W. (1999). *Contaminant hydrogeology* (2nd ed.). Prentice Hall.

Fetter, C. W. (2018). *Applied hydrogeology* (4th ed.). Waveland Press.

Fleckenstein, J. H., Krause, S., Hannah, D. M., & Boano, F. (2010). Groundwater–surface water interactions: New methods and models to improve understanding of processes and dynamics. *Advances in Water Resources, 33*(11), 1291–1295. https://doi.org/10.1016/j.advwatres.2010.09.011

Fontes, J.-C., & Garnier, J.-M. (1979). Determination of the initial ^{14}C activity of the total dissolved carbon: A review of the existing models and a new approach. *Water Resources Research, 15*(2), 399–413. https://doi.org/10.1029/WR015i002p00399

Freeze, R. A., & Cherry, J. A. (1979). *Groundwater*. Prentice-Hall.

Gagné, S., Larocque, M., Pinti, D. L., Saby, M., Meyzonnat, G., & Méjean, P. (2018). Benefits and limitations of using isotope-derived groundwater travel times and major ion chemistry to validate a regional groundwater flow model: Example from the Centre-du-Québec region, Canada. *Canadian Water Resources Journal / Revue canadienne des ressources hydriques, 43*(2), 195-213. https://doi.org/10.1080/07011784.2017.1394801

Gat, J. R. (1996). Oxygen and hydrogen isotopes in the hydrologic cycle. *Annual Review of Earth and Planetary Sciences, 24*, 225–262. https://doi.org/10.1146/annurev.earth.24.1.225

Gelhar, L. W., Welty, C., & Rehfeldt, K. R. (1992). A critical review of data on field-scale dispersion in aquifers. *Water Resources Research, 28*(7), 1955-1974. https://doi.org/10.1029/92WR00607

Giordano, M. (2009). Global groundwater? Issues and solutions. *Annual Review of Environment and Resources, 34*, 153–178. https://doi.org/10.1146/annurev.environ.030308.100251

Gleeson, T., Befus, K. M., Jasechko, S., Luijendijk, E., & Cardenas, M. B. (2016). The global volume and distribution of modern groundwater. *Nature Geoscience, 9*, 161–167. https://doi.org/10.1038/ngeo2590

Gleeson, T., Novakowski, K., & Kyser, T. K. (2009). Extremely rapid and localized recharge to a fractured rock aquifer. Journal of Hydrology, 376(3–4), 496–509. https://doi.org/10.1016/j.jhydrol.2009.07.056

Goode, D. J. (1996). Direct simulation of groundwater age. *Water Resources Research, 32*(2), 289–296. https://doi.org/10.1029/95WR03401

Gusyev, M. A., Toews, M., Morgenstern, U., Stewart, M., White, P., Daughney, C., & Hadfield, J. (2013). Calibration of a transient transport model to tritium data in streams and simulation of groundwater ages in the western Lake Taupo catchment, New Zealand. *Hydrology and Earth System Sciences, 17*(3), 1217–1227. https://doi.org/10.5194/hess-17-1217-2013

Gusyev, M. A., Abrams, D., Toews, M. W., Morgenstern, U., & Stewart, M. K. (2014). A comparison of particle-tracking and solute transport methods for simulation of tritium concentrations and groundwater transit times in river water. *Hydrology and Earth System Sciences, 18*(8), 3109–3119. https://doi.org/10.5194/hess-18-3109-2014

Han, L.-F., & Plummer, L. N. (2013). Revision of Fontes and Garnier's model for the initial ^{14}C content of dissolved inorganic carbon used in groundwater dating. *Chemical Geology, 351*, 105–114. https://doi.org/10.1016/j.chemgeo.2013.05.011

Han, L.-F., & Plummer, L. N. (2016). A review of single-sample-based models and other approaches for radiocarbon dating of dissolved inorganic carbon in groundwater. *Earth-Science Reviews, 152*, 119–142. https://doi.org/10.1016/j.earscirev.2015.11.004

Hanna Instruments. (n.d.). *HI98194 multiparameter pH/EC/TDS/salinity/DO/pressure/temperature waterproof meter* [Product page]. Retrieved

July 4, 2026, from https://hannainst.com/multiparameter-ph-orp-ec-tds-salinity-do-pressure-temperature-waterproof-meter

Harbaugh, A. W. (2005). *MODFLOW-2005, the U.S. Geological Survey modular ground-water model-The Ground-Water Flow Process* (Techniques and Methods 6-A16). U.S. Geological Survey. https://doi.org/10.3133/tm6A16

Hem, J. D. (1985). *Study and interpretation of the chemical characteristics of natural water* (3rd ed.; Water-Supply Paper 2254). U.S. Geological Survey. https://doi.org/10.3133/wsp2254

Hill, M. C., & Tiedeman, C. R. (2007). *Effective groundwater model calibration: With analysis of data, sensitivities, predictions, and uncertainty*. John Wiley & Sons. https://doi.org/10.1002/0470041080

Hossain, M. A., & Yonge, D. R. (1999a). Accuracy of the Taylor-Galerkin model for contaminant transport in groundwater. *Applied Mathematics and Computation, 102*, 109-119. https://doi.org/10.1016/S0096-3003(98)10038-3

Hossain, M. A., & Yonge, D. R. (1999b). On Galerkin models for transport in groundwater. *Applied Mathematics and Computation, 100*, 249-263. https://doi.org/10.1016/S0096-3003(98)00025-3

Huysmans, M., & Dassargues, A. (2005). Review of the use of Péclet numbers to determine the relative importance of advection and diffusion in low permeability environments. *Hydrogeology Journal, 13*, 895-904. https://doi.org/10.1007/s10040-004-0387-4

International Atomic Energy Agency. *Global Network of Isotopes in Precipitation (GNIP)*. Retrieved July 3, 2026, from https://www.iaea.org/services/networks/gnip

Janos, D., Molson, J. W., & Lefebvre, R. (2018). Regional groundwater flow dynamics and residence times in Chaudière-Appalaches, Québec, Canada: Insights from numerical simulations. *Canadian Water Resources Journal / Revue canadienne des ressources hydriques, 43*(2), 214-239. https://doi.org/10.1080/07011784.2018.1437370

Karandish, F., Liu, S., & de Graaf, I. (2025). Global groundwater sustainability: A critical review of strategies and future pathways. *Journal of Hydrology, 657*, 133060. https://doi.org/10.1016/j.jhydrol.2025.133060

Kazemi, G. A., Lehr, J. H., & Perrochet, P. (2006). *Groundwater age*. John Wiley & Sons. https://doi.org/10.1002/0471929514

Kitterød, N.-O., Kværner, J., Aagaard, P., Arustienė, J., Bikše, J., Dagestad, A., Gundersen, P., Hansen, B., Hjartarson, Á., Karro, E., Klavins, M., Marandi, A., Radienė, R., Retike, I., Rossi, P. M., & Thorling, L. (2022). Hydrogeology and groundwater quality in the Nordic and Baltic countries. *Hydrology Research, 53*(7), 958–982. https://doi.org/10.2166/nh.2022.018

Klaus, M. (2023). Decadal increase in groundwater inorganic carbon concentrations across Sweden. *Communications Earth & Environment, 4*, 221. https://doi.org/10.1038/s43247-023-00885-4

Konikow, L. F., & Kendy, E. (2005). Groundwater depletion: A global problem. *Hydrogeology Journal, 13*, 317–320. https://doi.org/10.1007/s10040-004-0411-8

Kuang, X., Liu, J., Scanlon, B. R., Jiao, J. J., Jasechko, S., Lancia, M., Biskaborn, B. K., Wada, Y., Li, H., Zeng, Z., Guo, Z., Yao, Y., Gleeson, T., Nicot, J.-P., Luo, X., Zou, Y., &

Zheng, C. (2024). The changing nature of groundwater in the global water cycle. *Science, 383*(6686), eadf0630. https://doi.org/10.1126/science.adf0630

Larocque, M., Cloutier, V., Levison, J., & Rosa, E. (2018). Results from the Quebec Groundwater Knowledge Acquisition Program. *Canadian Water Resources Journal / Revue canadienne des ressources hydriques, 43*(2), 69–74. https://doi.org/10.1080/07011784.2018.1472040

Laurencelle, M. (2018). *Propriétés hydrauliques et processus d'invasion par la mer de Champlain du système aquifère rocheux fracturé régional de la Montérégie Est, Québec, Canada* [Doctoral dissertation, Université du Québec, Institut national de la recherche scientifique]. EspaceINRS. https://espace.inrs.ca/id/eprint/7618/

Laurencelle, M., Lefebvre, R., Ladevèze, P., Carrier, M.-A., Rivard, C., Parent, M., & Benoît, N. (2013, September 29–October 3). *Modeling the evolution of the regional fractured-rock aquifer system in the Northern Lake Champlain watershed following the last deglaciation* [Conference presentation]. GéoMontréal 2013, Montréal, Québec, Canada.

Laurencelle, M., Lefebvre, R., Molson, J. W., & Parent, M. (2016, September 25–29). *Modeling of the palaeo-hydrogeological evolution of a fractured-rock aquifer following the Champlain Sea Transgression in the St. Lawrence Valley (Quebec)* [Conference poster]. 43rd IAH International Congress, Montpellier, France. https://doi.org/10.13140/RG.2.2.28675.30249

Laurencelle, M., Lefebvre, R., Parent, M., & Molson, J. W. (2018, April 8–13). *Paleo-hydrogeological evolution of a fractured-rock aquifer since the Champlain Sea incursion in the St. Lawrence Valley (Quebec, Canada)* [Conference poster]. EGU General Assembly 2018, Vienna, Austria. https://doi.org/10.13140/RG.2.2.19742.64328

Leketa, K., & Abiye, T. (2021). Using environmental tracers to characterize groundwater flow mechanisms in the fractured crystalline and karst aquifers in Upper Crocodile River Basin, Johannesburg, South Africa. *Hydrology, 8*(1), 50. https://doi.org/10.3390/hydrology8010050

Libby, W. F. (1960, December 12). *Radiocarbon dating* [Nobel lecture]. Nobel Prize Outreach. https://www.nobelprize.org/prizes/chemistry/1960/libby/lecture/

Lindsey, B. D., Jurgens, B. C., & Belitz, K. (2019). *Tritium as an indicator of modern, mixed, and premodern groundwater age* (Scientific Investigations Report 2019–5090). U.S. Geological Survey. https://doi.org/10.3133/sir20195090

Lohman, S. W. (1972). *Definitions of selected ground-water terms-Revisions and conceptual refinements* (Water-Supply Paper 1988). U.S. Geological Survey. https://doi.org/10.3133/wsp1988

Lucas, L. L., & Unterweger, M. P. (2000). Comprehensive review and critical evaluation of the half-life of tritium. *Journal of Research of the National Institute of Standards and Technology, 105*(4), 541–549. https://doi.org/10.6028/jres.105.043

Meyzonnat, G., Larocque, M., Barbecot, F., Pinti, D. L., & Gagné, S. (2016). The potential of major ion chemistry to assess groundwater vulnerability of a regional aquifer in southern Quebec, Canada. *Environmental Earth Sciences, 75*, 68. https://doi.org/10.1007/s12665-015-4793-9

Meyzonnat, G., Musy, S., Corcho-Alvarado, J. A., Barbecot, F., Pinti, D. L., Purtschert, R., Lauzon, J.-M., & McCormack, R. (2023). Age distribution of groundwater in fractured aquifers of the St. Lawrence Lowlands (Canada) determined by environmental tracers ($^{3}H/^{3}He$, ^{85}Kr, SF_6, CFC-12, ^{14}C). *Hydrogeology Journal, 31*, 2139–2157. https://doi.org/10.1007/s10040-023-02671-0

MilliporeSigma. (n.d.). *WHEATON HDPE bottle, 1 L* (Product No. Z569712; synonym W082130) [Product page]. Retrieved July 4, 2026, from https://www.sigmaaldrich.com/US/en/product/aldrich/z569712

Minea, I., Boicu, D., Negm, A., Zelenakova, M., & Demirci, M. (2025). Editorial: Impact of climate changes on groundwater resources. *Frontiers in Environmental Science, 13*, 1557374. https://doi.org/10.3389/fenvs.2025.1557374

Ministère de l'Environnement, de la Lutte contre les changements climatiques, de la Faune et des Parcs. (n.d.). *Projets d'acquisition de connaissances sur les eaux souterraines (PACES)* [Data set]. Données Québec. https://www.donneesquebec.ca/recherche/fr/dataset/projets-d-acquisition-de-connaissances-sur-les-eaux-souterraines-paces

Molson, J. W., & Frind, E. O. (2012). On the use of mean groundwater age, life expectancy and capture probability for defining aquifer vulnerability and time-of-travel zones for source water protection. *Journal of Contaminant Hydrology, 127*, 76-87. https://doi.org/10.1016/j.jconhyd.2011.06.001

Molson, J.W., & Frind, E.O. 2017. HEATFLOW-SMOKER: Density-dependent flow and advective-dispersive transport of thermal energy, mass or residence time. University of Laval and University of Waterloo.

Murseli, S., Middlestead, P., St-Jean, G., Zhao, X., Jean, C., Crann, C. A., Kieser, W. E., & Clark, I. D. (2019). The preparation of water (DIC, DOC) and gas (CO_2, CH_4) samples for radiocarbon analysis at AEL-AMS, Ottawa, Canada. *Radiocarbon, 61*(5), 1563–1571. https://doi.org/10.1017/RDC.2019.14

Nastev, M., Rivera, A., Lefebvre, R., Martel, R., & Savard, M. M. (2005). Numerical simulation of groundwater flow in regional rock aquifers, southwestern Quebec, Canada. *Hydrogeology Journal, 13*, 835–848. https://doi.org/10.1007/s10040-005-0445-6

Neumann, L. E., Šimůnek, J., & Cook, F. J. (2011). Implementation of quadratic upstream interpolation schemes for solute transport into HYDRUS-1D. *Environmental Modelling & Software, 26*(11), 1298–1308. https://doi.org/10.1016/j.envsoft.2011.05.010

Neuman, S. P. (1990). Universal scaling of hydraulic conductivities and dispersivities in geologic media. *Water Resources Research, 26*(8), 1749-1758. https://doi.org/10.1029/WR026i008p01749

Niswonger, R. G., Panday, S., & Ibaraki, M. (2011). *MODFLOW-NWT, a Newton formulation for MODFLOW-2005* (Techniques and Methods 6-A37). U.S. Geological Survey. https://doi.org/10.3133/tm6A37

Nowak, M. E., Schwab, V. F., Lazar, C. S., Behrendt, T., Kohlhepp, B., Totsche, K. U., Küsel, K., & Trumbore, S. E. (2017). Carbon isotopes of dissolved inorganic carbon reflect utilization of different carbon sources by microbial communities in two limestone

aquifer assemblages. *Hydrology and Earth System Sciences, 21*, 4283–4300. https://doi.org/10.5194/hess-21-4283-2017

Ofterdinger, U., MacDonald, A. M., Comte, J.-C., & Young, M. E. (2019). Groundwater in fractured bedrock environments: Managing catchment and subsurface resources—An introduction. *Geological Society, London, Special Publications, 479*, 1–9. https://doi.org/10.1144/SP479-2018-170

Ohenhen, L. O., Mayle, M., Kolawole, F., Ismail, A., & Atekwana, E. A. (2023). Exploring for groundwater in sub-Saharan Africa: Insights from integrated geophysical characterization of a weathered basement aquifer system, central Malawi. *Journal of Hydrology: Regional Studies, 49*, 101433. https://doi.org/10.1016/j.ejrh.2023.101433

OI Analytical (2005). Aurora 1030 Wet Oxidation TOC analyzer Operator's Manual. College Station, Texas.

Okada, S., & Momoshima, N. (1993). Overview of tritium: Characteristics, sources, and problems. *Health Physics, 65*(6), 595–609. https://doi.org/10.1097/00004032-199312000-00001

Olsson, I. U. (Ed.). (1970). *Radiocarbon variations and absolute chronology: Proceedings of the Twelfth Nobel Symposium*. Almqvist & Wiksell.

Parent, M., Rivard, C., Lefebvre, R., Carrier, M.-A., & Séjourné, S. (2014). *Hydrogeological systems of the Montérégie Est region, southern Quebec: Fieldtrip guidebook, GeoMontréal 2013 Conference* (Geological Survey of Canada Open File 7605). Geological Survey of Canada. https://doi.org/10.4095/294604

Pearson, F. J., Jr. (1965). Use of C-13/C-12 ratios to correct radiocarbon ages of materials initially diluted by limestone. In *Proceedings of the Sixth International Conference on Radiocarbon and Tritium Dating* (USAEC CONF-650652, pp. 357–366). U.S. Atomic Energy Commission.

Pearson, F. J., Jr., & Hanshaw, B. B. (1970). Sources of dissolved carbonate species in groundwater and their effects on carbon-14 dating. In *Isotope hydrology 1970: Proceedings of a symposium on use of isotopes in hydrology held by the International Atomic Energy Agency in cooperation with UNESCO in Vienna, 9–13 March 1970* (pp. 271–285). International Atomic Energy Agency.

Pollock, D. W. (2012). *User guide for MODPATH version 6-A particle-tracking model for MODFLOW* (Techniques and Methods 6-A41). U.S. Geological Survey. https://doi.org/10.3133/tm6A41

Pollock, D. W. (2016). *User guide for MODPATH version 7-A particle-tracking model for MODFLOW* (Open-File Report 2016-1086). U.S. Geological Survey. https://doi.org/10.3133/ofr20161086

Reilly, T. E., Plummer, L. N., Phillips, P. J., & Busenberg, E. (1994). The use of simulation and multiple environmental tracers to quantify groundwater flow in a shallow aquifer. *Water Resources Research, 30*(2), 421–433. https://doi.org/10.1029/93WR02655

Reilly, T. E., & Harbaugh, A. W. (2004). *Guidelines for evaluating ground-water flow models* (Scientific Investigations Report 2004-5038). U.S. Geological Survey. https://doi.org/10.3133/sir20045038

Reimer, P. J., Brown, T. A., & Reimer, R. W. (2004). Discussion: Reporting and calibration of post-bomb ^{14}C data. *Radiocarbon, 46*(3), 1299–1304. https://doi.org/10.1017/S0033822200033154

Rivera, A. (Ed.). (2014). *Canada's groundwater resources*. Fitzhenry & Whiteside. https://publications.gc.ca/site/eng/9.854795/publication.html

Rohde, M. M., Albano, C. M., Huggins, X., Klausmeyer, K. R., Morton, C., Sharman, A., Zaveri, E., Saito, L., Freed, Z., Howard, J. K., Job, N., Richter, H., Toderich, K., Rodella, A. S., Gleeson, T., Huntington, J., Chandanpurkar, H. A., Purdy, A. J., Famiglietti, J. S., . . . Stella, J. C. (2024). Groundwater-dependent ecosystem map exposes global dryland protection needs. *Nature, 632*, 101–107. https://doi.org/10.1038/s41586-024-07702-8

Rozanski, K., Araguás-Araguás, L., & Gonfiantini, R. (1993). Isotopic patterns in modern global precipitation. In P. K. Swart, K. C. Lohmann, J. McKenzie, & S. Savin (Eds.), *Climate change in continental isotopic records* (Geophysical Monograph Series, Vol. 78, pp. 1–36). American Geophysical Union. https://doi.org/10.1029/GM078p0001

Sanford, W. E., Plummer, L. N., McAda, D. P., Bexfield, L. M., & Anderholm, S. K. (2004). Hydrochemical tracers in the Middle Rio Grande Basin, USA: 2. Calibration of a groundwater-flow model. *Hydrogeology Journal, 12*(4), 389–407. https://doi.org/10.1007/s10040-004-0326-4

Sauty, J.-P. (1980). An analysis of hydrodispersive transfer in aquifers. *Water Resources Research, 16*(1), 145-158. https://doi.org/10.1029/WR016i001p00145

Scanlon, B. R., Keese, K. E., Flint, A. L., Flint, L. E., Gaye, C. B., Edmunds, W. M., & Simmers, I. (2006). Global synthesis of groundwater recharge in semiarid and arid regions. *Hydrological Processes, 20*, 3335–3370. https://doi.org/10.1002/hyp.6335

Schlegel, M., Souza, J., Warix, S. R., Murray, E. M., Godsey, S. E., Seyfried, M. S., Cram, Z., & Lohse, K. A. (2024). Carbon evolution and mixing effects on groundwater age calculations in fractured basalt, southwestern Idaho, U.S.A. *Frontiers in Water, 6*, 1388465. https://doi.org/10.3389/frwa.2024.1388465

Seltzer, A. M., Bekaert, D. V., Barry, P. H., Durkin, K., Mace, E., Aalseth, C. E., Zappala, J., Mueller, P., Jurgens, B. C., & Kulongoski, J. T. (2021). Groundwater residence time estimates obscured by anthropogenic carbonate. *Science Advances, 7*(17), eabf3503. https://doi.org/10.1126/sciadv.abf3503

Sherwood Lollar, B., Warr, O., & Higgins, P. M. (2024). The hidden hydrogeosphere: The contribution of deep groundwater to the planetary water cycle. *Annual Review of Earth and Planetary Sciences, 52*, 443–466. https://doi.org/10.1146/annurev-earth-040722-102252

Singhal, B. B. S., & Gupta, R. P. (2010). *Applied hydrogeology of fractured rocks* (2nd ed.). Springer. https://doi.org/10.1007/978-90-481-8799-7

Sophocleous, M. (2002). Interactions between groundwater and surface water: The state of the science. *Hydrogeology Journal, 10*, 52–67. https://doi.org/10.1007/s10040-001-0170-8

Stosch, H.-G. (2022). *Excel template to plot hydrochemical data into a Piper diagram* (Version 1.1) [Computer software]. Zenodo. https://doi.org/10.5281/zenodo.6581209

Stuiver, M., & Polach, H. A. (1977). Discussion: Reporting of ^{14}C data. *Radiocarbon, 19*(3), 355–363. https://doi.org/10.1017/S0033822200003672

Taylor, R., Scanlon, B., Döll, P. *et al.* Ground water and climate change. *Nature Clim Change* **3**, 322–329 (2013). https://doi.org/10.1038/nclimate1744

Thermo Fisher Scientific. (n.d.-a). *Choice nylon syringe filters, 0.45 µm, 25 mm* (Catalog No. CH4525-NN) [Product page]. Retrieved July 4, 2026, from https://www.thermofisher.com/order/catalog/product/CH4525-NN

Thermo Fisher Scientific. (n.d.-b). *EnviroWare assembled borosilicate glass EPA vials* (Catalog No. 0333914E) [Product page]. Retrieved July 4, 2026, from https://www.thermofisher.com/order/catalog/product/0333914A

Thermo Fisher Scientific. (n.d.-c). *Nalgene wide-mouth lab quality HDPE bottles, 60 mL* (Catalog No. 2104-0002) [Product page]. Retrieved July 4, 2026, from https://www.thermofisher.com/order/catalog/product/2104-0002

Thompson, M., & Walsh, J. N. (1989). *Handbook of inductively coupled plasma spectrometry* (2nd ed.). Blackie.

Tóth, J. (1963). A theoretical analysis of groundwater flow in small drainage basins. *Journal of Geophysical Research, 68*(16), 4795–4812. https://doi.org/10.1029/JZ068i016p04795

UNESCO World Water Assessment Programme. (2022). *The United Nations World Water Development Report 2022: Groundwater: Making the invisible visible*. UNESCO. https://doi.org/10.54679/CAOS3862

University of Ottawa. (n.d.-a). *Geochemistry laboratory*. Retrieved July 4, 2026, from https://www.uottawa.ca/faculty-science/research/centres-institutes-core-facilities-laboratories/geochemistry

University of Ottawa. (n.d.-b). *Radiocarbon laboratory*. Retrieved July 4, 2026, from https://www.uottawa.ca/research-innovation/national-ael-ams-facility/radiocarbon-laboratory

University of Ottawa. (n.d.-c). *Services: Ján Veizer Stable Isotope Laboratory*. Retrieved July 4, 2026, from https://www.uottawa.ca/research-innovation/isotope/services

University of Ottawa. (n.d.-d). *Tritium laboratory*. Retrieved July 4, 2026, from https://www.uottawa.ca/research-innovation/national-ael-ams-facility/tritium-laboratory

U.S. Geological Survey. (2019). *How much water is there on Earth?* Water Science School. https://www.usgs.gov/water-science-school/science/how-much-water-there-earth

U.S. Geological Survey. (2025, June 24). *ModelMuse: A graphical user interface for groundwater models*. https://www.usgs.gov/software/modelmuse-a-graphical-user-interface-groundwater-models

Vogel, J. C., Thilo, L., & van Dijken, M. (1974). Determination of groundwater recharge with tritium. *Journal of Hydrology, 23*(1–2), 131–140. https://doi.org/10.1016/0022-1694(74)90027-4

Winston, R. B. (2009). *ModelMuse-A graphical user interface for MODFLOW-2005 and PHAST* (Techniques and Methods 6-A29). U.S. Geological Survey. https://doi.org/10.3133/tm6A29

Winston, R. B. (2024). *Revision of ModelMuse to support the use of PEST software with MODFLOW and SUTRA models* (Techniques and Methods 6-A64). U.S. Geological Survey. https://doi.org/10.3133/tm6A64

Winter, T. C., Harvey, J. W., Franke, O. L., & Alley, W. M. (1998). *Ground water and surface water: A single resource* (U.S. Geological Survey Circular 1139). U.S. Geological Survey. https://doi.org/10.3133/cir1139

Woessner, W. W. (2000). Stream and fluvial plain ground water interactions: Rescaling hydrogeologic thought. *Ground Water, 38*(3), 423–429. https://doi.org/10.1111/j.1745-6584.2000.tb00228.x

Xu, M., & Eckstein, Y. (1995). Use of weighted least-squares method in evaluation of the relationship between dispersivity and field scale. *Ground Water, 33*(6), 905-908. https://doi.org/10.1111/j.1745-6584.1995.tb00035.x

Yager, R. M., & Ratcliffe, N. M. (2011). *Hydrogeology and simulation of groundwater flow in fractured rock in the Newark basin, Rockland County, New York* (Scientific Investigations Report No. 2010-5250). U.S. Geological Survey. https://doi.org/10.3133/sir20105250

Zheng, C., & Wang, P. P. (1999). *MT3DMS: A modular three-dimensional multispecies transport model for simulation of advection, dispersion and chemical reactions of contaminants in groundwater systems-Documentation and user's guide* (Contract Report SERDP-99-1). U.S. Army Engineer Research and Development Center. https://apps.dtic.mil/sti/pdfs/ADA373474.pdf

Zhu, C. (2000). Estimate of recharge from radiocarbon dating of groundwater and numerical flow and transport modelling. *Water Resources Research, 36*(9), 2607–2620. https://doi.org/10.1029/2000WR900172

Zipper, S. C., Brookfield, A. E., Ajami, H., Ayers, J. R., Beightel, C., Fienen, M. N., Gleeson, T., Hammond, J. C., Hill, M. C., Kendall, A. D., Kerr, B., Lapides, D. A., Porter, M., Parimalarenganayaki, S., Rohde, M. M., & Wardropper, C. (2024). Streamflow depletion caused by groundwater pumping: Fundamental research priorities for management-relevant science. *Water Resources Research, 60*(5), e2023WR035727. https://doi.org/10.1029/2023WR035727

Supplementary Material:

1. MODFLOW-NWT Solver Configuration and Convergence Sensitivity Testing

MODFLOW-NWT was implemented through ModelMuse to solve the steady-state groundwater-flow equation for the Montérégie Est regional model. ModelMuse provides a graphical interface for defining the model grid, hydrogeological properties, boundary conditions, and numerical solver settings, while MODFLOW-NWT performs the finite-difference groundwater-flow calculations (Winston, 2009; Niswonger et al., 2011).

The Newton formulation was selected because the upper fractured-bedrock layer was represented as convertible and could therefore behave as confined, semi-confined, or unconfined depending on the simulated hydraulic head. Under these conditions, transmissivity varies with saturated thickness, producing a nonlinear groundwater-flow problem. MODFLOW-NWT applies Newton–Raphson linearization and upstream weighting to improve convergence where cells approach dry conditions or transition between saturated and partially saturated states (Niswonger et al., 2011). This formulation was therefore considered appropriate for the heterogeneous regional fractured-bedrock system represented in this study.

Numerical behaviour in MODFLOW-NWT is controlled by parameters defining the hydraulic-head and flux convergence criteria, the permitted number of nonlinear iterations, smoothing near dry-cell conditions, and the linear method used to solve the resulting asymmetric matrix. Suggested starting values and allowable or practical ranges reported for the principal MODFLOW-NWT controls are summarized in Table 14 in Supplementary Material. Parameters for which no fixed range is provided are problem dependent and should be selected through evaluation of convergence behaviour, model water balance, and the physical plausibility of the simulated hydraulic-head and groundwater-flow distributions (Niswonger et al., 2011).

Table 14. Suggested starting input values for the MODFLOW-NWT input file (after Niwonfer et al., 2011, U.S. Geological Survey).

Input variable name	Default values	Range
Iteration Control		
HEADTOL	1×10^{-4} (L)	—

FLUXTOL	500 (L^3/T)	—
MAXITEROUT	100	10–2,000
Dry Cell Tolerance		
THICKFACT	0.00001	1×10^{-6} – 1
NWT Options		
LINMETH	1	1 or 2
IPRNWT	0	0 or 2
IBOTAV	0**	0 or 1
Under-relaxation Input		
(Model Complexity: Simple / Moderate / Complex)		
DBDTHETA	0.97 / 0.7 / 0.4	0–1
DBDKAPPA	0.0001 / 0.0001 / 0.00001	0–1
DBDGAMMA	0.0 / 0.0 / 0.0	0–1
MOMFACT	0.0 / 0.1 / 0.1	0–1
Residual Control		
(Model Complexity: Simple / Moderate / Complex)		

BACKFLAG	0*** / 0 / 0	0 or 1
MAXBACKITER	—	1–100
BACKTOL	—	1–2
BACKREDUCE	—	0.05–0.99
Linear Solution Control and Options for GMRES		
(Model Complexity: Simple / Moderate / Complex)		
MAXITINNER	50 / 50 / 50	25–1,000
ILUMETHOD	2/2/2002	1 or 2
LEVFILL	1/1/2001	5–10 (ILUMETHOD=1), 0–2 (ILUMETHOD=2)
STOPTOL	1×10^{-10} / 1×10^{-10} / 1×10^{-10}	1×10^{-8} – 1×10^{-12}
MSDR	5/10/2015	5–20

Note: (L) and (T) represent the model length and time units, respectively. In the present model, (L) is metres and (T) is years. The GMRES-specific controls are included for completeness but were not active in the final simulation because LINMETH was set to 2.

1.1 Final solver configuration

The final MODFLOW-NWT solver configuration is summarized in Table 15. The head-convergence tolerance was set to 0.0001 m, meaning that the maximum change in hydraulic head between successive outer iterations was required to fall below this value before the head criterion was satisfied. FLUXTOL was set to 500 m^3/yr, consistent with the length

and time units used throughout the model. FLUXTOL represents the root-mean-squared change in calculated fluxes between successive nonlinear iterations and is a numerical convergence criterion rather than the total volumetric water-budget discrepancy.

MAXITEROUT was increased to 500 to provide sufficient nonlinear iterations for convergence across the large, heterogeneous model domain. Increasing the maximum permitted number of iterations does not itself alter the governing groundwater-flow equations; rather, it prevents the simulation from terminating before the convergence criteria have been satisfied.

THICKFACT was assigned a value of 0.0001. This dimensionless parameter controls the smoothing of conductance and saturated-thickness terms as cells approach dry conditions. The selected value is one order of magnitude higher than the default value of 0.00001 reported by Niswonger et al. (2011) but remains within the recommended parameter range and was selected to provide stable numerical behaviour during transitions between saturated and nearly dry conditions in the upper convertible layer. Because THICKFACT can influence localized conductance and flow calculations in cells approaching dryness, the value of 0.0001 was applied consistently in all final groundwater-flow simulations.

The χMD linear solution method was selected by setting LINMETH to 2. This method is designed to solve the asymmetric matrix generated by the Newton formulation. Solver-convergence output was enabled to permit examination of nonlinear iteration behaviour in the MODFLOW listing file. IBOTAV was disabled, and the ModelMuse complexity setting was defined as Moderate. The CONTINUE option was also disabled so that the model terminated when convergence was not achieved, preventing unconverged simulations from being used as inputs to MODPATH 7 or MT3D-USGS.

Table 15. Final MODFLOW-NWT solver settings used for the Montérégie Est regional groundwater-flow model.

Parameter	Final setting	Units or option	Role in the simulation
HEADTOL	0.0001	m	Hydraulic-head convergence tolerance

FLUXTOL	500	$m^3\ yr^{-1}$	Flux convergence tolerance
MAXITEROUT	500	Iterations	Maximum number of nonlinear outer iterations
THICKFACT	0.00001	Dimensionless	Smoothing factor applied as saturated thickness approaches zero
LINMETH	2	χMD	Linear method used to solve the asymmetric Newton matrix
IPRNWT	Enabled	Positive output-control setting	Prints solver-convergence information to the listing file
IBOTAV	0	Disabled	Does not apply the optional bottom-cell head correction
Model complexity	Moderate	ModelMuse option	Applies internal solver controls appropriate for

			moderate nonlinearity
CONTINUE	Disabled	ModelMuse option	Stops the simulation when convergence is not achieved

1.1.2 Convergence sensitivity assessment

Initial model testing used HEADTOL and FLUXTOL values of 1 m and 10 m³/yr, respectively. The final simulation used HEADTOL = 0.0001 m and FLUXTOL = 500 m³/yr, consistent with the recommended MODFLOW-NWT starting criteria expressed in the units of the present model. Although the revised settings apply a substantially stricter hydraulic-head criterion and a different flux criterion, comparison of the resulting simulations showed no discernible change in the regional hydraulic-head pattern and negligible differences in simulated heads at the observation locations (Table 16).

This comparison indicates that the original simulation had already approached the same numerical groundwater-flow solution and that the revised parameters primarily affected the formal convergence requirements rather than the regional hydrogeological interpretation. The final settings were nevertheless retained because they provided stable solver behaviour, satisfied the selected convergence criteria, and were more readily comparable with the MODFLOW-NWT guidance provided by Niswonger et al. (2011).

All MODPATH 7 particle-tracking and MT3D-USGS transport simulations reported in this study were generated using the final converged MODFLOW-NWT solution. This ensured that calculated pathlines and age-tracer predictions were based on a consistent hydraulic-head and cell-by-cell groundwater-flow field. The similarity of the hydraulic solutions obtained using the alternative convergence settings indicates that the principal model predictions were not materially controlled by the selection of HEADTOL and FLUXTOL at the regional scale examined here. However, THICKFACT and other parameters influencing cells near dry

conditions were maintained consistently because they may affect localized cell-to-cell flows even when regional hydraulic-head distributions appear similar.

The final model hydraulic head Table is shown in Table 17.

Table 16. Comparison of measured and simulated 2010 hydraulic heads under two MODFLOW-NWT solver configurations.

Well ID	Measured head (2010) m	Scenario 1 predicted head m	Scenario 2 predicted head m	Change: Scenario 2 − Scenario 1 m
ME 007	107.82	98.5	97.72	−0.78
ME 050	123.32	127.48	127.52	0.04
ME 066	376.5	374.76	375.6	0.84
ME 068	232.03	271.61	276.53	4.92
ME 203	95.12	92.41	89.22	−3.19
ME 214	80.154	107.07	112.86	5.79
ME 219	235.35	231.01	235.46	4.45
ME 008	127.41	122.33	118.42	−3.91
ME 061	190.86	200.94	202.06	1.12
ME 063	210.18	206.55	206.56	0.01
ME 111	109.93	115.75	118.08	2.33

ME 200	23.03	27.99	27.91	−0.08
ME 205	8.31	27.82	27.79	−0.03
ME 081	22.46	13.46	13.63	0.17
ME 129	48.39	46.27	46.58	0.31
ME 149	52.67	39.39	39.45	0.06
ME 125	38.18	40.05	40.08	0.03
ME 178	51.26	47.35	47.41	0.06
ME 109	65.92	53.01	51.46	−1.55
ME 154	33.34	28.73	27.82	−0.91
ME 175	51.62	44.47	44.48	0.01
ME 176	30.52	23.52	21.97	−1.55
ME 092	37.85	37.19	37.1	−0.09
ME 223	29.9	16.14	16.12	−0.02
ME 122	8.64	8.83	8.76	−0.07
ME 218	120.66	99	94.55	−4.45

ME 195	64.39	58.46	56.83	−1.63

Comparison of measured hydraulic heads from the 2010 field campaign with predicted heads obtained using two MODFLOW-NWT solver configurations. Scenario 1 represents the initial simulation, which did not satisfy the selected numerical convergence criteria. Scenario 2 used HEADTOL = 1×10^{-5} m, FLUXTOL = 100 $m^3\ yr^{-1}$, MAXITEROUT = 100, and THICKFACT = 1×10^{-7}, and completed with convergence warnings. The final column shows the change in predicted hydraulic head between Scenario 2 and Scenario 1. Positive values indicate that Scenario 2 produced a higher predicted head, whereas negative values indicate a lower predicted head.

Table 17. Predicted head vs the measured head by the final model.

Well ID	Predicted head (2010)	Measured head (2010)
ME 007	98.5	107.82
ME 050	127.48	123.32
ME 066	374.76	376.5
ME 068	271.61	232.03
ME 203	92.41	95.12
ME 214	107.07	80.154
ME 219	231.01	235.35
ME 008	122.33	127.41
ME 061	200.94	190.86
ME 063	206.55	210.18

ME 111	115.75	109.93
ME 200	27.99	23.03
ME 205	27.82	8.31
ME 081	13.46	22.46
ME 129	46.27	48.39
ME 149	39.39	52.67
ME 125	40.05	38.18
ME 178	47.35	51.26
ME 109	53.01	65.92
ME 154	28.73	33.34
ME 175	44.47	51.62
ME 176	23.52	30.52
ME 092	37.19	37.85
ME 223	16.14	29.9
ME 122	8.83	8.64

2. Conditional Definition of the Upper Aquifer Bottom Elevation

The bottom elevation of the Upper Aquifer was calculated in ModelMuse using the following Boolean ternary expression:

If (piezo > (Model_Top - 100.0), Model_Top - 100.0,piezo - 10.0)

Where the piezometric surface is less than 100 m below the bedrock surface, the Upper Aquifer is assigned a thickness of 100 m. Where the piezometric surface is more than 100 m below the bedrock surface, the bottom of the Upper Aquifer is placed 10 m below the piezometric surface.

This conditional formulation prevents the initial hydraulic head from occurring at or below the bottom of the upper model layer. It therefore preserves the assumed 100 m fractured-bedrock thickness across most of the model domain while locally increasing the layer thickness in areas with deeper hydraulic heads. This adjustment reduced the occurrence of dry or nearly dry cells and improved model stability.

3. Sensitivity analysis of the lower model boundary of the fractured bedrock layer

The elevation of the lower model boundary of the upper fractured bedrock layer was varied between 250, 500, and 1000 m below mean sea level while all other model parameters and boundary conditions were held constant (Table 18). Simulated hydraulic heads changed only slightly at most observation wells, generally by less than 2 m, indicating that the regional head distribution was not strongly controlled by the assumed model depth. Greater sensitivity occurred at only a few locations, particularly ME218, where the 1000 m-deep scenario produced a substantially larger change. The lower boundary was therefore retained at 500 m below mean sea level because it provided an intermediate and sufficiently deep representation of the regional bedrock flow system, minimized the potential influence of an artificially shallow no-flow boundary, and avoided extending the model to 1000 m where additional depth did not consistently improve agreement with observed heads and introduced greater localized sensitivity.

Table 18. Sensitivity of simulated 2010 hydraulic heads to the assumed lower model boundary elevation (−250, −500, and −1000 m above mean sea level).

Well ID	Measured head (2010) m	Predicted head (2010), m Upper Aquifer Bottom set as: -500m	Predicted head (2010) m Upper Aquifer Bottom set as: -1000m	Predicted head (2010) m Upper Aquifer Bottom set as: -250m
ME 007	107.82	98.5	98.43	98.6
ME 050	123.32	127.48	127.52	127.52
ME 066	376.5	374.76	374.13	374.88

ME 068	232.03	271.61	271.05	272.2
ME 203	95.12	92.41	92.13	93.35
ME 214	80.154	107.07	106.79	109.89
ME 219	235.35	231.01	230.45	232.37
ME 008	127.41	122.33	118.38	120.32
ME 061	190.86	200.94	202.07	202.1
ME 063	210.18	206.55	206.57	206.49
ME 111	109.93	115.75	115.06	115.92
ME 200	23.03	27.91	27.93	27.91
ME 205	8.31	27.79	27.79	27.79

ME 081	22.46	13.63	13.63	13.63
ME 129	48.39	46.57	46.57	46.58
ME 149	52.67	39.39	39.24	39.55
ME 125	38.18	40.05	40.07	40.04
ME 178	51.26	47.41	47.41	47.41
ME 109	65.92	53.01	52.93	52.95
ME 154	33.34	28.73	27.82	27.83
ME 175	51.62	44.47	44.49	44.49
ME 176	30.52	23.52	21.97	23.49
ME 092	37.85	37.19	37.1	37.77

ME 223	29.9	16.14	16.11	16.11
ME 122	8.64	8.83	8.77	8.76
ME 218	120.66	99	82.95	94.56
ME 195	64.39	58.46	56.83	58.2

4. Sensitivity of the Coupled Hydraulic Scaling Factor

Two coupled scaling factors were evaluated:

(1) 0.135335, representing the exponential reduction in hydraulic conductivity at a conceptual depth of 50 m; and

(2) 0.278, representing an alternative, less strongly reduced hydraulic parameterization.

For each simulation, the same factor was applied globally to the upper-layer hydraulic conductivity, recharge, and DRN conductance inputs. All remaining MODFLOW-NWT and MT3D-USGS parameters, including model geometry, porosity, dispersivity, tracer boundary concentrations, and radioactive-decay constants, were held constant. Predicted raw ^{14}C activities were then compared with the measured 2010 values used during model calibration.

Table 19. Comparison of measured and model-predicted raw ^{14}C activities under alternative coupled hydraulic scaling factors. Residuals were calculated as predicted minus measured activity.

Water group	Sample ID	Measured (14C) (pMC)	Predicted, factor 0.135335 (pMC)	Residual (pMC)	Predicted, factor 0.278 (pMC)	Residual (pMC)2
A1	ME007	100	100	0	100	0
A1	ME050	100	100	0	100	0
A1	ME066	72.2	77.76	5.56	76.12	3.92
A2	ME068	23	22.49	−0.51	29.68	6.68
A2	ME203	31	31.16	0.16	33.46	2.46
A2	ME214	20.9	22	1.1	27.34	6.44

A2	ME218	32.8	33.07	0.27	34.44	1.64
A2	ME219	14.5	14.6	0.1	27.35	12.85
A3	ME008	33.4	34	0.6	35	1.6
A3	ME061	24	25.13	1.13	38.4	14.4
A3	ME063	57.9	58	0.1	58	0.1
A3	ME111	56.1	58	1.9	58	1.9
M1	ME122	21.2	26.99	5.79	32.66	11.46
M1	ME125	37.8	38	0.2	38	0.2
M1	ME178	40.7	42	1.3	50.29	9.59
M1	ME109	29.4	30.1	0.7	36.12	6.72
M2	ME154	51.3	55.28	3.98	68.45	17.15
M2	ME176	75.5	80.33	4.83	81.58	6.08
M2	ME092	68	73.58	5.58	83.33	15.33

M3	ME223	12.7	14.14	1.44	16.75	4.05

5. Hydraulic-Head Sensitivity to Vertical Hydraulic Conductivity and Application of the 0.135335 Scaling Factor

This supplementary section compares simulated hydraulic heads from three model configurations used to evaluate the sensitivity of the regional groundwater-flow model to vertical hydraulic conductivity and the application of the 0.135335 scaling factor. The final model was selected based on its improved agreement with measured 2010 hydraulic heads and its consistency with the conceptual recharge–discharge framework of the Montérégie Est fractured-bedrock aquifer (Table 20).

The final model applies the recharge, discharge, and horizontal hydraulic conductivity scaling approach, including the 0.135335 factor applied to K_x and K_y. In this configuration, vertical hydraulic conductivity was assigned as:

$K_z=K_x/20$

This configuration was compared against two sensitivity scenarios. In the first sensitivity scenario, vertical hydraulic conductivity was reduced by assigning:

$K_z=K_x/100\ K_z$

This scenario tests the effect of stronger vertical anisotropy and reduced vertical hydraulic connection between model layers. In the second sensitivity scenario, the 0.135335 factor was not applied to the recharge, discharge, K_x, and K_y parameterization. This scenario was used to evaluate the influence of the scaling factor on simulated hydraulic-head distributions.

The reduced-K_z scenario generally produced lower simulated hydraulic heads than the final model. This indicates that assigning $K_z=K_x/100K_z$ reduced vertical hydraulic connectivity too strongly, limiting vertical leakage and lowering simulated heads at many wells.

These sensitivity results support the selection of the final model configuration using $K_z=K_x/20K_z$ and the 0.135335 scaling factor. This configuration provides the best match to measured hydraulic heads while maintaining a physically reasonable representation of vertical hydraulic exchange and regional flow patterns within the fractured-bedrock aquifer.

Therefore, the final model was used for subsequent MODPATH particle tracking and MT3D-USGS age-tracer simulations.

Table 20. Comparison of simulated hydraulic heads under final-model, reduced K_z, and no-scaling-factor sensitivity scenarios.

Well ID	Final-model predicted hydraulic head (m)	Predicted Kz = Kx/100 (m)	Predicted, no 0.135335 factor (m)
ME007	98.5	94.5	90.88
ME050	127.48	114.67	116.97
ME066	374.76	348.91	369.18
ME068	271.61	231.3	259.75
ME203	92.41	81.99	83.44
ME214	107.07	81.8	103.12
ME218	99	36.47	36.49
ME219	231.01	192.72	217.55
ME008	122.33	112.21	108.73

ME061	200.94	189	192.19
ME063	206.55	199.67	198.45
ME111	115.75	115.75	105.88
ME081	13.63	6.83	12.51
ME129	46.57	44.12	44.85
ME149	39.39	39.08	38.65
ME109	53.01	45.78	48.52
ME122	8.83	5.94	16.84
ME125	40.05	24.18	38.13
ME178	47.41	45.47	46.23
ME092	37.19	30.17	28.13
ME154	28.73	26.85	24.37
ME176	23.52	21.42	20.63

ME200	27.91	24.67	24.33
ME205	27.79	24.98	23
ME175	44.47	39.18	40.37
ME223	16.14	13.22	15.89
ME195	58.46	56.36	57.98

6. The lithology of sampled wells

Table 21. Comparison of measured and model-predicted raw ^{14}C values, recharge-zone distance, and interpreted lithologies for sampled groundwater wells within the Montérégie Est fractured bedrock aquifer system from the 2010 field campaign.

2010 Field Campaign:

Well ID	Measured Raw ^{14}C (pMC)	Predicted ^{14}C (pMC)	Distance from Recharge Zone (m)	Age-Tracer Well	Interpreted Bedrock Lithology (Carrier et. al, 2013)
ME007	100	100	0	Yes	Slate, arkose, slaty schist, limestone, and conglomerate
ME050	100	100	0	Yes	Feldspathic sandstone with slate interbeds
ME066	72.2	77.76	222.26	No	Schist
ME068	23	22.49	0	No	Schist and chlorite phyllite (metabasalt)
ME203	31	31.16	157	No	Feldspathic sandstone with slate interbeds
ME214	20.9	22	1414.71	No	Slate and phyllite, limestone, sandstone, siltstone and calcareous conglomerate
ME219	14.5	14.6	428.44	No	Phyllite, schist and wacke

ME008	33.4	34	285.23	No	Feldspathic sandstone with slate interbeds
ME061	24	25.13	1265.69	No	Phyllite, schist, slate, sandstone, quartzite, dolostone and conglomerate
ME063	57.9	58	0	Yes	Phyllite, schist, slate, sandstone, quartzite, dolostone and conglomerate
ME111	56.1	58	No	No	Slate, arkose, slaty schist, limestone and conglomerate
ME122	21.2	26.99	6817.14	Yes	Shale and mudstone with interbeds of sandstone, siltstone and limestone
ME125	37.8	38	0	No	Mudrock, slate, dolostone and sandstone
ME178	40.7	42	56.59	No	Mudrock, slate, dolostone and sandstone
ME154	51.3	55.28	2994.29	No	Calcareous mudstone with interbeds of argillaceous limestone
ME176	75.5	80.33	3839.98	No	Mudrock, slate, dolostone and sandstone

ME092	68	73.58	4471.37	No	Shale and mudstone with interbeds of sandstone, siltstone and limestone
ME223	12.7	14.14	6178.02	No	Shale and mudstone with interbeds of sandstone, siltstone and limestone
ME129	82.7	84.41	734.48	No	Mudrock, slate, dolostone and sandstone
ME149	53.5	51.28	1980.18	No	Dolostone, sandstone, limestone and shale
ME175	**47.6**	**—**	**—**	**Yes**	**Mudrock, slate, dolostone and sandstone**

2025 Field Campaign:

Well ID	Measured Raw ^{14}C (pMC)	Predicted ^{14}C (pMC)	Distance from Recharge Zone (m)	Age-Tracer Well	Interpreted Bedrock Lithology
ME241	54.85	52.29	395.35	No	Mudrock, slate, dolostone and sandstone
ME143-1	72.72	72.87	68.06	No	Mudrock, slate, dolostone and sandstone
ME122	22.13	26.99	6719.48	Yes	Shale and mudstone with interbeds of sandstone, siltstone and limestone

ME063	52.06	51.77	0	Yes	Phyllite, schist, slate, sandstone, quartzite, dolostone and conglomerate
ME003	79.73	75.785	383.55	No	Slate with sandstone and limestone interbeds
ME064	47.83	52	164.12	No	Phyllite, schist, slate, sandstone, quartzite, dolostone and conglomerate
ME195	68.77	70.94	655.74	No	Slate, arkose, slaty schist, limestone and conglomerate
ME011	7.52	9.52	2166.07	No	Feldspathic sandstone with slate interbeds
ME039	49.32	54.06	48.35	No	Phyllite, schist, slate, sandstone, quartzite, dolostone and conglomerate
ME007	66.58	100	0	Yes	Slate, arkose, slaty schist, limestone and conglomerate
ME050	59.16	100	0	Yes	Feldspathic sandstone with slate interbeds
ME175*	**82.53**	—	—	**Yes**	**Mudrock, slate, dolostone and sandstone**

7. Porosity graph of different porosity MT3D-USGS radiocarbon results

Similar effective porosity values have also been applied in fractured-rock groundwater models outside Québec; for example, the USGS Newark Basin fractured-rock model used an effective porosity of 0.02, estimated by comparing simulated groundwater ages with groundwater ages derived from tritium/helium dating (Yager & Ratcliffe, 2011). This supports the use of an effective porosity value of 0.02 in the present model as a reasonable regional-scale approximation for fractured bedrock. In the flow model, porosity does not substantially affect the simulated hydraulic-head distribution under steady-state conditions, but it directly influences advective groundwater velocity, particle-tracking travel times, and age-tracer transport. For a given Darcy flux, groundwater velocity is inversely proportional to effective porosity; therefore, a lower porosity would produce faster simulated groundwater velocities, shorter travel times, and higher predicted ^{3}H and ^{14}C activities due to less radioactive decay. In contrast, a higher porosity would slow simulated groundwater velocities, increase residence times, and produce lower predicted ^{3}H and ^{14}C activities due to greater radioactive decay along flowpaths. The selected value of 0.02 therefore provides a reasonable baseline, while sensitivity testing with higher and lower porosity values can be used to evaluate uncertainty in simulated groundwater residence times and tracer concentrations.

8. Cell Péclet Number Calculation for Transport Stability

Another type of P_e is the mesh or cell Péclet number (P_{ec}). This is a dimensionless parameter in numerical simulations comparing rates of advection to diffusion flow in a single computational cell (Hossain & Yonge, 1998), it is defined as Equation 23:

$$P_{ec} = \frac{v\Delta x}{D} \quad (23)$$

Where v is the velocity of the groundwater flow, Δx is the grid cell distance (L), and D is the dispersion coefficient (L^2/T) (Hossain & Yonge, 1998). When $P_{ec} \leq 2$ is required for numerical models to provide oscillation-free and accurate results.

Using the same numerical simplifications as equation 22, equation 22 is simplified into equation 24:

$$P_{ec} \simeq \frac{ve\Delta x}{\alpha Lve} = \frac{\Delta x}{\alpha L} \quad (24)$$

$\therefore\ P_{ec} \simeq \frac{250m}{376.09m} = 0.66 \leq 2$, indicating numerical stability across the model.

9. Underprediction table of the wells in CS group

Table 22. Comparison of measured and MT3D-USGS-predicted raw ^{14}C activities for selected 2010 groundwater samples from the CS and M2 hydrochemical water groups.

Well ID	Water group	INRS/PACES ID	Measured raw ^{14}C, 2010 (pMC)	Predicted ^{14}C (pMC)
ME081	CS	INRS182	76.6	0.34
ME200	CS	P03	16.7	9.26
ME205	CS	P08 / DUP18	18	0.004
ME175	M2	INRS277	47.6	23.11

10. Radiocarbon recharge boundary scenario sensitivity analysis

Table 23. Spatial, hydrochemical, and radiocarbon characteristics of the selected 2010 groundwater samples, together with MT3D-USGS predicted 14C activities under three recharge-boundary scenarios. Scenario 1 assigns 100 pMC to all PACES-defined main recharge zones. Scenario 2 assigns 35 pMC to all PACES-defined main recharge zones. Scenario 3 assigns 100 pMC to unconfined zones, while 14C concentrations in semi-confined and confined zones are allowed to evolve through the transport simulation.

ME ID	Water group	PACES/INRS ID	Measured raw 14C (pMC)	Scenario 1 predicted 14C Main recharge zones = 100 pMC	Scenario 2 predicted 14C Main recharge zones = 35 pMC	Scenario 3 predicted 14C Unconfined zones = 100 pMC
ME 007	A1	INRS108	106.1	100	99.99	100
ME 050	A1	INRS151	106.	100	35	78.61
ME 066	A1	INRS167	72.2	100	35	100
ME 068	A2	INRS169	23.	100	35	81.49
ME 203	A2	P06	31.	97.17	34.16	16.16
ME 214	A2	P16	20.9	100	35	63.37
ME 218	A2	P19	32.8	93.28	35.95	75.99
ME 219	A2	P20	14.5	93.2	35.95	79.99
ME 008	A3	INRS109	33.4	100	35	94.22
ME 061	A3	INRS162	24.	84.84	29.53	37.14

ME 063	A3	INRS1 64	57.9	100	35	97.47
ME 111	A3	INRS2 13	56.1	99.99	35	97.25
ME 109	M1	INRS2 11	29.4	93.86	75.51	90.38
ME 122	M1	INRS2 24	21.2	66.97	23.2	28.07
ME 125	M1	INRS2 27	37.8	100	35	91.74
ME 178	M1	INRS2 80	40.7	100	35	49.9
ME 092	M2	INRS1 93	68.	82.36	32	75.57
ME 154	M2	INRS2 56	51.3	54.44	24.85	40.35
ME 176	M2	INRS2 78	75.5	83.43	25.02	70.76
ME 223	M3	P23	12.7	23.82	10.24	12.055
ME 129	LL	INRS2 31	82.7	86.55	34.25	84.35
ME 149	LL	INRS2 51	53.5	40	26.58	40.
ME 081	CS	INRS1 82	76.6	36.93	15.5	27.9
ME 200	CS	P03	16.7	0.31	0.18	0.15
ME 205	CS	P08	18.	34.4	12.7	0.001

11. Measured and Model Predicted Age Tracer Data for 2010 and 2025

Table 24. 2010 measured and predicted tritium data by hydrochemical water group.

No.	Water group	ME ID	INRS/PACES sample ID	Measured (^{3}H) (TU)	Predicted ($_3$H) (TU)	Distance from PACES-defined main recharge zone (m)
1	A1	ME007	INRS108	13.4	14	0
2	A1	ME050	INRS151	14.9	14	0
3	A1	ME066	INRS167	14.3	14	222.26
4	A2	ME068	INRS169	4.9	3.19	0
5	A2	ME203	P06	3.4	3.28	157
6	A2	ME214	P16	0	0.24	1,414.71
7	A2	ME218	P19	2.7	3.94	198.11
8	A2	ME219	P20	0.8	1.25	428.44
9	A3	ME008	INRS109	7.4	8.3	285.23
10	A3	ME061	INRS162	3.1	3	1,265.69
11	A3	ME063	INRS164	10	14	0
12	A3	ME111	INRS213	8.9	14	0
13	M1	ME122	INRS224	<DL*	0.27	6,817.14
14	M1	ME125	INRS227	4.9	14	0
15	M1	ME178	INRS280	3.2	2.27	56.59

16	M1	ME109	INRS211	3.9	4.19	281.83
17	M2	ME154	INRS256	1	1.29	2,994.29
18	M2	ME176	INRS278	<DL*	0.3	3,839.98
19	M2	ME092	INRS193	9.6	7.99	4,471.37
20	M3	ME223	P23 (DUP17)	<DL*	0	6,178.02
21	LL	ME129	INRS231	12.4	9.2	734.48
22	LL	ME149	INRS251	<DL*	0.01	1,980.18

***Note:** Values recorded as -0.5 TU in the source dataset (Beaudry et al., 2018) indicate measurements below the reporting or detection limit. These values were assigned 0 TU for both prediction and measured raw ^{3}H plotting and regression analysis and should not be interpreted as true negative tritium concentrations.*

Table 25. 2010 Measured and predicted radiocarbon data by hydrochemical water groups.

No.	Water group	ME ID	INRS/PACES ID	Measured raw (^{14}C) (pMC)	Predicted (^{14}C) (pMC)	Distance from PACES-defined main recharge zone (m)
1	A1	ME007	INRS108	100	100	0
2	A1	ME050	INRS151	100	100	0
3	A1	ME066	INRS167	72.2	77.76	222.26
4	A2	ME068	INRS169	23	22.49	0
5	A2	ME203	P06	31	31.16	157
6	A2	ME214	P16	20.9	22	1,414.71
7	A2	ME218	P19	32.8	33.07	198.11
8	A2	ME219	P20	14.5	14.6	428.44

9	A3	ME008	INRS109	33.4	34	285.23
10	A3	ME061	INRS162	24	25.13	1,265.69
11	A3	ME063	INRS164	57.9	58	0
12	A3	ME111	INRS213	56.1	58	0
13	M1	ME122	INRS224	21.2	26.99	6,817.14
14	M1	ME125	INRS227	37.8	38	0
15	M1	ME178	INRS280	40.7	42	56.59
16	M1	ME109	INRS211	29.4	30.1	281.83
17	M2	ME154	INRS256	51.3	55.28	2,994.29
18	M2	ME176	INRS278	75.5	80.33	3,839.98
19	M2	ME092	INRS193	68	73.58	4,471.37
20	M3	ME223	P23 (DUP17)	12.7	14.14	6,178.02
21	LL	ME129	INRS231	82.7	84.41	734.48
22	LL	ME149	INRS251	53.5	51.28	1,980.18

Table 26. Measured and model-predicted tritium concentrations for the 2025 model-evaluation dataset. Measured and MT3D-USGS-predicted (^{3}H) concentrations are reported in tritium units (TU), with sample-specific analytical uncertainties reported for the measured values. For plotting and statistical analysis, measured or predicted concentrations below 0.5 TU, including measurements below the detection limit, were assigned a value of 0 TU. The dataset contains nine groundwater wells.

Well ID	Measured (3H) (TU)	Predicted (3H) (TU)	Measured uncertainty (TU)
ME241	7.59	7.81	±0.35

ME143	9.29	12.45	±0.43
ME003	4.34	6.82	±0.29
ME064	0	0	0
ME011	5.11	6.82	±0.29
ME039	8.58	13.2	±0.37
ME124	4.83	2.95	±0.29
ME086	0	0	0
ME151	2.97	5.6	±0.24

Note: After applying the 0.5 TU threshold, ME064 and ME086 both plot at (0) TU measured and (0) TU predicted. The graph therefore contains nine observations, although these two points overlap at the origin. Resampled wells for age tracers are not included in the fitted graph of 2025.

Table 27. Measured and model-predicted raw 14C activities for groundwater samples collected during the 2025 field campaign. Measured and MT3D-USGS-predicted 14C activities are reported in percent modern carbon (pMC). Analytical uncertainties reported as F14C were converted to pMC by multiplying by 100.

Sample ID	Measured raw (14C) (pMC)	Predicted (14C) (pMC)	Measured uncertainty (pMC)	Distance from PACES-defined main recharge zone (m)
ME241	54.85	52.29	±0.14	395.35
ME143	72.72	72.87	±0.19	68.06
ME003	79.73	75.79	±0.17	383.55
ME064	47.83	52	±0.13	164.12
ME011	7.52	9.52	±0.06	2,166.07
ME039	49.32	54.06	±0.13	48.35

Note: Resampled wells for age tracers are not included in the fitted graph of 2025.

12. Calculation of bicarbonate and carbonate

Bicarbonate (HCO_3^-), carbonate (CO_3^{2-}), and alkalinity values for the 2010 dataset were taken from the Beaudry et al. (2018) hydrochemical dataset and are reported in Table 9. The Beaudry supplementary material also reports HCO_3^- and CO_3^{2-} as major/minor carbonate-system parameters across the hydrochemical water groups, showing that bicarbonate is generally the dominant carbonate species in the Montérégie Est groundwater system. For the 2025 samples, HCO_3^- and CO_3^{2-} were calculated rather than directly measured. These calculations used measured pH, temperature, and dissolved inorganic carbon (DIC) concentrations to distribute total DIC among aqueous carbonate species according to carbonate equilibrium relationships. In this approach, DIC was first converted to total dissolved carbon concentration, and the relative proportions of dissolved CO_2/H_2CO_3, HCO_3^-, and CO_3^{2-} were calculated from pH-dependent carbonate dissociation equilibria. The calculated HCO_3^- and CO_3^{2-} concentrations were then converted to mg/L using their molar masses.

For the 2025 groundwater samples, bicarbonate (HCO_3^-), carbonate (CO_3^{2-}), and alkalinity were calculated from measured dissolved inorganic carbon (DIC), pH, and temperature. DIC was first converted from ppm C, equivalent to mg C/L, into mol C/L. The measured pH was then used with temperature-corrected carbonate equilibrium constants to distribute total DIC among dissolved CO_2/H_2CO_3, HCO_3^-, and CO_3^{2-}. The calculated molar concentrations of HCO_3^- and CO_3^{2-} were then converted to mg/L using their molar masses. Alkalinity was calculated from the carbonate species, mainly HCO_3^- and CO_3^{2-}, and reported as mg/L as $CaCO_3$. This approach allowed the 2025 calculated carbonate-system values to be compared with the 2010 Beaudry et al. hydrochemical dataset, which reports HCO_3^- and CO_3^{2-} as carbonate-system parameters across the Montérégie Est water groups.

Sample calculation:

For sample ME122, the measured 2025 values were:

DIC = 55.8 ppm C

pH = 8.9

First, DIC was converted from ppm C to mol C/L. Because ppm C is equivalent to mg C/L:

55.8 ppm C = 55.8 mg C/L

$DIC = (55.8 \times 10^{-3}) / 12.011$

$DIC = 4.65 \times 10^{-3}$ mol C/L

At pH 8.9, most dissolved inorganic carbon occurs as bicarbonate (HCO_3^-), with a smaller fraction present as carbonate (CO_3^{2-}). Based on the carbonate equilibrium calculation, the approximate molar concentrations are:

$[HCO_3^-] = 4.50 \times 10^{-3}$ mol/L

$[CO_3^{2-}] = 1.45 \times 10^{-4}$ mol/L

These molar concentrations were then converted to mg/L using their molar masses:

$HCO_3^- = 4.50 \times 10^{-3}$ mol/L × 61,016.8 mg/mol

$HCO_3^- = 274.87$ mg/L

$CO_3^{2-} = 1.45 \times 10^{-4}$ mol/L × 60,008.9 mg/mol

$CO_3^{2-} = 8.71$ mg/L

Alkalinity was then calculated from the bicarbonate and carbonate concentrations and reported as mg/L as $CaCO_3$:

Alkalinity = $([HCO_3^-] + 2[CO_3^{2-}]) \times 50{,}043$

Alkalinity = $(0.00450 + 2 \times 0.000145) \times 50{,}043$

Alkalinity ≈ 239.09 mg/L as $CaCO_3$

Therefore, for ME122, the calculated 2025 carbonate-system values are:

$HCO_3^- = 274.87$ mg/L

$CO_3^{2-} = 8.71$ mg/L

Alkalinity = 239.09 mg/L as $CaCO_3$